Strojniški vestnik
Journal of Mechanical Engineering

no. 6

year 2016

volume 62

Strojniški vestnik – Journal of Mechanical Engineering (SV-JME)

Aim and Scope

The international journal publishes original and (mini)review articles covering the concepts of materials science, mechanics, kinematics, thermodynamics, energy and environment, mechatronics and robotics, fluid mechanics, tribology, cybernetics, industrial engineering and structural analysis.

The journal follows new trends and progress proven practice in the mechanical engineering and also in the closely related sciences as are electrical, civil and process engineering, medicine, microbiology, ecology, agriculture, transport systems, aviation, and others, thus creating a unique forum for interdisciplinary or multidisciplinary dialogue.

The international conferences selected papers are welcome for publishing as a special issue of SV-JME with invited co-editor(s).

Editorial Office
University of Ljubljana, Faculty of Mechanical Engineering
SV-JME, Aškerčeva 6, SI-1000 Ljubljana, Slovenia
Phone: 386 (0)1 4771 137
Fax: 386 (0)1 2518 567
info@sv-jme.eu, http://www.sv-jme.eu

Print: Grafex, d.o.o., printed in 310 copies

Founders and Publishers
University of Ljubljana, Faculty of Mechanical Engineering, Slovenia
University of Maribor, Faculty of Mechanical Engineering, Slovenia
Association of Mechanical Engineers of Slovenia
Chamber of Commerce and Industry of Slovenia, Metal Processing Industry Association

Cover: The cover shows the application of cooling of Inconel 718 workpiece with liquefied nitrogen jet during orthogonal radial turning. With performed experimental measurements of temperature distributions, the surface heat transfer coefficient has been defined (back calculation method). Based on the results, the correlation with nitrogen phase and surface overheat temperature has been defined. Results prove that nitrogen phase plays an important role for achieving efficiency of the cryogenic machining process.

Image Courtesy: Laboratory for Machining, University of Ljubljana, Faculty of Mechanical Engineering, Slovenia

ISSN 0039-2480

General information

Strojniški vestnik – Journal of Mechanical Engineering is published in 11 issues per year (July and August is a double issue).

Institutional prices include print & online access: institutional subscription price and foreign subscription €100,00 (the price of a single issue is €10,00); general public subscription and student subscription €50,00 (the price of a single issue is €5,00). Prices are exclusive of tax. Delivery is included in the price. The recipient is responsible for paying any import duties or taxes. Legal title passes to the customer on dispatch by our distributor.

Single issues from current and recent volumes are available at the current single-issue price. To order the journal, please complete the form on our website. For submissions, subscriptions and all other information please visit: *http://en.sv-jme.eu/*.

You can advertise on the inner and outer side of the back cover of the journal. The authors of the published papers are invited to send photos or pictures with short explanation for cover content.

We would like to thank the reviewers who have taken part in the peer-review process.

The journal is subsidized by Slovenian Research Agency.

Strojniški vestnik - Journal of Mechanical Engineering is available on http://www.sv-jme.eu, where you access also to papers' supplements, such as simulations, etc.

Contents

Strojniški vestnik - Journal of Mechanical Engineering
volume 62, (2016), number 6
Ljubljana, June 2016
ISSN 0039-2480

Published monthly

Papers

Strojniški vestnik - Journal of Mechanical Engineering 62(2016)6, 331-339

DOI:10.5545/sv-jme.2016.3572
Original Scientific Paper
Received for review: 2015-12-08
Received revised form: 2016-03-14
Accepted for publication: 2016-04-14

The Procedure of Solving the Inverse Problem for Determining Surface Heat Transfer Coefficient between Liquefied Nitrogen and Inconel 718 Workpiece in Cryogenic Machining

Matija Hriberšek[1,*] – Viktor Šajn[1] – Franci Pušavec[1] – Joel Rech[2] – Janez Kopač[1]
[1] University of Ljubljana, Faculty of Mechanical Engineering, Slovenia
[2] University of Lyon, Ecole Nationale d'Ingenieurs de Saint-Etienne, France

The determination of the cooling effect is important since the phase (liquid and gaseous) has a significant influence on the cooling effect, which indirectly influences the integrity of the machined surface after machining process. Therefore, this paper presents how the phase of liquefied nitrogen influences the surface heat transfer coefficient. The determination of the phase has been defined by resolving the inverse problem with conducted experiments and verified by the design of a numerical simulation. The experimental part includes the temperature measurement in the material (a plate of Inconel 718) at the time when the nozzle has moved across the plate, and the design of the numerical simulation. The results have shown that the surface heat transfer coefficient reaches the maximum value of 75000 W/(m²K) at the temperature difference (between liquefied nitrogen-Inconel 718 plate) of 196 K (liquid phase of the nitrogen). Steep value decrease for heat transfer coefficent (15000 W/(m²K)) at temperature difference 160 K (pure gaseous phase of the nitrogen) has been detected.
Keywords: liquefied nitrogen, cryogenic machining, numerical simulation, surface heat transfer coefficient

Highlights
- *Performation of experimental temperature measurements with thermocouples in Inconel 718 plate.*
- *Design of numerical simulation and experimental validation of results.*
- *Determination of the surface heat transfer coefficient for nitrogen comparing liquid and gaseous phase.*
- *Specification of the differences between the liquid and gaseous phase of nitrogen.*

0 INTRODUCTION AND STATE OF THE ART

When planning production processes, the most important task is to obtain the best machine part quality with minimum manufacturing costs. The environmental aspects have also become significantly important [1], which is connected with striving to achieve a higher level of productivity and environmental awareness.

This idea has been recognized in terms of sustainable manufacturing. This includes minimizing the use of cooling lubrication fluids based on artificial ingredients and increasing cutting speeds. The way of supplying and the quantity cooling lubrication liquids delivered to the cutting zone largely influence machinability of constructional materials [2]. The use of ecologically impeccable cooling lubrication fluids that do not harm people's health and are environment-friendly has been promoted. Such cooling lubrication fluids are for instance liquefied nitrogen and vegetable-based oils. In connection with such fluids, more and more sustainable alternative technologies have been developing. One of them is cryogenic machining, where liquefied nitrogen can be used as a cooling lubrication fluid [3]. These facts encouraged the present research on how liquefied nitrogen functions as a cooling lubrication fluid, in order to enable its use in industry in future to encourage green production.

Materials such as high temperature alloys (nickel, titanium, etc.) are usually employed in manufacturing processes of high added valued products, especially in space, aircraft and military industry [4]. Such materials have excellent mechanical and thermal properties which are maintained even when the materials are exposed to high temperatures. Additionally, such materials have low thermal conductivity and get plastically hardened at high temperatures, hence their extremely poor machinability [5]. At the formation of a chip, high temperatures and deformations occur in contact zones, which causes fast tool wear or even cutting edge fractures [6]. According to these facts, it can be concluded that such materials should be machined by the use of a cooling fluid, such as liquefied nitrogen. For conducting this research, Inconel 718 was chosen. Inconel 718 is a nickel-chromium alloy and is one of high-temperature alloys.

The main property of cryogenic machining is the use of a cryogenic fluid (liquefied nitrogen) as the cooling fluid during cutting processes at very low temperatures. The dividing line between cryogenic and conventional temperatures is in evaporation point that should be below –150 °C [7]. The idea is based on the delivering of a cryogenic fluid (liquefied

*Corr. Author's Address: University of Ljubljana, Faculty of Mechanical Engineering, Aškerčeva 6, 1000 Ljubljana, Slovenia, matija.hribersek@fs.uni-lj.si

nitrogen) to the local zone on the cutting edge where the temperature during cutting is the highest [8].

Based on the researches of the temperature in the cutting zone, Ding and Hong [9] has explained that the use of liquefied nitrogen increases tool life and achieves better material machinability (shorter chips), compared to conventional processes. Dhokia et al. [10] has proven that the surface quality after cryogenic machining is better (lower roughness), compared to the cutting processes at which conventional cooling lubrication fluids are used.

Pu et al. [11] has conducted experiments to prove that compressive residual stresses in a material after cryogenic machining are favorable since they prevent cracks on the surface.

Reviewing the state of the art in the field of observation phase of nitrogen, the majority of previous studies have been conducted with the purpose to research the macrocharacteristics of heat transfer when boiling [12]. Tsukamoto and Uyemara [13] have presented an optical way of observing bubble formation at the surface of a thin wire, heated by a stepwise transient in liquid nitrogen. Kida et al. [12] has conducted researches in the field of the microcharacteristics of boiling, analyzing the size and the frequency of nitrogen bubble formation.

The aim of the paper is to contribute to better understanding of the influence of liquefied nitrogen in terms of defining the surface heat transfer coefficient in correlation to its phase, by resolving the inverse problem. Studies in terms of defining surface heat transfer coefficient between liquefied nitrogen and surface workpiece have been encouraged by not knowing exactly values for this coefficient published in the past publications.

Most papers dealing with this topic use the surface heat transfer coefficient values referenced from the following papers: Hong and Ding [14] (h_{LN}=23270 W/(m^{2}K) to 46750 W/(m^{2}K) and Hong and Ding [15] (h_{LN}=48270 W/(m^{2}K) to 74950 W/(m^{2}K).

The paper presents the analysis of the difference between the influence of the liquid and gaseous phase of nitrogen on in-depth temperature and depth of the cooling layer in Inconel 718 workpiece. This simulates the temperature distribution in the cutting zone during machining, what indirectly influences the friction coefficient, the surface integrity of the workpiece, and the functionality of a final component/product [16].

0.1 Theoretical Background

0.1.1 The Difference between Liquid and Gaseous Phase

The paper presents the difference between the influence of the liquid and gaseous phase of nitrogen in terms of determining the surface heat transfer coefficient depending on the temperature of the fluid/workpiece. An important characteristic of nitrogen is its phase. Due to its extremely low evaporation temperature (T) (–196 °C at air pressure (p) of 10^5 Pa), liquefied nitrogen has a high tendency to evaporate and consequently, the phase (liquid and gaseous) can change when liquefied nitrogen exits the nozzle. Physical properties of this fluid for both phases, such as density (ρ), specific heat (C_p), viscosity (v), and thermal conductivity (λ) are listed in Table 1 [17].

Table 1. *Differences in physical properties between liquid and gaseous phase at T = –196 °C (both phases) and p = 10^5 Pa (both phases)*

	Phase of the media	
Physical properties of nitrogen	N_1 (liquid)	N_2 (gaseous)
ρ [kg/m^3]	803.6	4.979
C_p [J/(kgK)]	2046	1351
v [Pa·s]	1.463·10^4	0.05331·10^{-4}
λ [W/(mK)]	1.320·10^{-1}	0.07658·10^{-1}

Fig. 1 presents the phases of nitrogen.

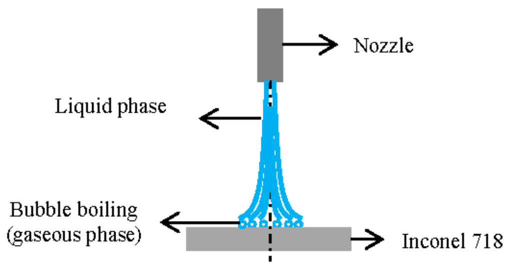

Fig. 1. *Phases of nitrogen (liquid and gaseous)*

0.1.2 Thermal Conditons at Cooling with Liquefied Nitrogen

The function of the application of liquefied nitrogen to the local area of a tool or to a workpiece (tool-workpiece contact) is the cooling of the machining process. It is a process of convection (cooling), where a cold flow of the fluid comes to the surface of a warmer body and creates a boundary layer that fits the surface of the body. That is assumed to be the gaseous layer of nitrogen which has lower thermal conductivity than pure liquid phase (Fig. 1). In this way the nitrogen film modeling has been designed in the numerical simulation [18].

For performing experiments in this work, the plate has been cooled by the moving nozzle, where convective (forming thin film on the workpiece surface) and diffused (heat transfer through the solid body) heat transfer occurs. Convective heat transfer occurs when a thin film is formed on the workpiece surface and when boiling bubbles start moving upwards in the atmosphere because of the pushing force. Advection needs to be taken into account, too, and it is a phenomenon when energy (including thermal energy) is moved by the physical transfer of a hot or cold object from one place to another. This can be described by the Eq. (1) [19]:

$$Q = v_f \rho C_p \Delta T, \tag{1}$$

where Q [W] is heat flux, ΔT [K] temperature difference and v_f [m/s] velocity of the flux.

From the physical point of view, the process can be described by Fouriers law, which is defined as: the heat flux density q [W/m^2], resulting from thermal conduction, is proportional to the magnitude of the temperature gradient and opposite to it in sign. The law can be defined in the Cartesian coordinate system and is defined by Eq. (2):

$$\vec{q} = -\lambda \cdot \left(\frac{\partial T}{\partial x}, \frac{\partial T}{\partial y}, \frac{\partial T}{\partial z} \right). \tag{2}$$

This means that if temperature decreases with distance, the heat flux density q is positive and in the direction of distance vector. If temperature T increases with the distance vector $\vec{r}$, the heat flux density q is negative and in the opposite direction of the distance vector $\vec{r}$ [18]. Heat flux density, accepted by the body, is defined by Eq. (3):

$$q = h\left(T_{body} - T_{fluid}\right), \quad q = \frac{\partial T}{\partial z},$$
$$T_{body} = 25 \text{ °C}, \quad T_{fluid} = -196 \text{ °C}, \tag{3}$$

where T_{fluid} [°C] is fluid temperature and T_{body} [°C] body temperature.

The surface heat transfer coefficient h [W/(m^{2}K)] is in thermodynamics and mechanics a proportional coefficient to the heat flux density, which flows through the surface layer, and the temperature difference [20] and [21].

Additionally, the convective heat transfer, that is present when the difference between the temperature of the workpiece surface and the fluid exists has to be taken into account, too. This phenomenon refers to the thermal boundary layer which causes the surface heat transfer. Additionally, there is also a velocity boundary layer due to the friction between the surface and the fluid which is the result of the fluid viscosity [22] and has to be taken into account.

1 METHODS

At first, a numerical simulation (finite element method) has been designed to describe experimental condition and to resolve the inverse problem for determining the surface heat transfer coefficient between liquefied nitrogen and Inconel 718 workpiece plate.

Eulerian formulation, which is fixed in space and can be used to simulate the flow through the material mesh, has been used [23].

When at least one parameter of the process is not known, different methods can be used to resolve inverse problem [24]. In the experimental part of measuring temperature, the surface heat transfer coefficent was not known. The focus of the numerical simulation was to determine the surface heat transfer coefficent, based on fitting the experimental T_{exp} (t) and the simulation $T_{sim}(t)$ curve.

Fig. 2 displays the sequence of the operations that have been conducted to determine the surface heat transfer coefficient between liquefied nitrogen and Inconel 718. At the beginning, the values for the heat transfer coefficient from literature have been selected [14] and [15].

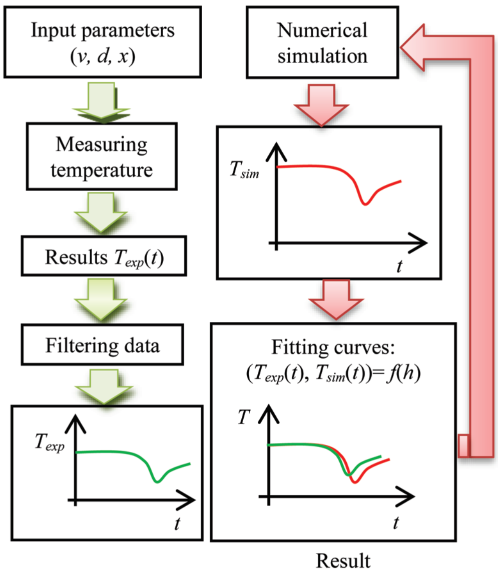

Fig. 2. *Procedure for defining the surface heat transfer coefficient between liquefied nitrogen and the workpiece surface (Inconel 718)*

To reach the fitting of the experimental curve $T_{exp}(t)$ and the simulation curve $T_{sim}(t)$, the exact values for the surface heat transfer coefficient, depending on the difference of the temperature between the coolant and the workpiece, have been determined.

Additionally, the values for the surface heat transfer coefficient have been checked to coincide with the value interval from the literature.

2 THE EXPERIMENTAL PART

The workpiece was an Inconel 718 plate (150 mm × 246 mm × 2.5 mm) which was hot-rolled, aged and polished at R_a < 0.3 µm on the upper side. On the lower side of the plate, 3 sets of 5 holes within the distance of 5 mm were made. Each set of the holes was at the following depths: 0.1 mm, 0.5 mm and 1 mm from the polishing side of the plate. Three sets of holes were machined because of the future researches of the temperature field along the depth of the Inconel 718 plate.

The nozzle was moved across the middle of the plate, right above the middle hole on the grinded surface of the plate. In the experiments, five thermocouples NiCr-Ni (K-type, diameter 0.3 mm) were used. The thermocouples were fixed to the holes with a power tape. To assure the contact of the thermocouple with the workpiece, the thermopaste based on silicon oil with metal oxides was used. The nozzle diameter was 1 mm and moved 15 mm above the plate. Liquefied nitrogen was piped through the nozzle under pressure of p = 1.8·10^5 Pa. For data acquisition, a NI acquisition card was used, while for the nozzle movement, the nozzle was attached to the machine spindle and moved along the plate. Firstly, the input parameters were determined and with it the design of experiments. The parameters were: the measuring temperature in correlation to the nozzle moving speed v [m/min], depth d [mm] and the distance from the neutral line x [mm] (in the middle of the plate). The temperature in the material (T) was measured, depending on the changing of the input parameters (v, d and x). The value range for the moving nozzle speed was defined based on comparable cutting speed, recommended for machining Inconel 718. By the determination of the values, the aim was to determine the temperature drop in the material after the nozzle had moved across the plate. This can be compared to one workpiece revolution in the turning process. The design of experiments comprised 12 experiments at different nozzle moving speeds (5, 15, 25 or 35) m/min and at different depths at which the temperature in the material was measured (0.1 mm, 0.5 mm or 1 mm). Fig. 3 shows the experimental setup (the clamping of the nozzle onto the machine spindel and the detail that shows the diameter of the jet dispersion on the surface).

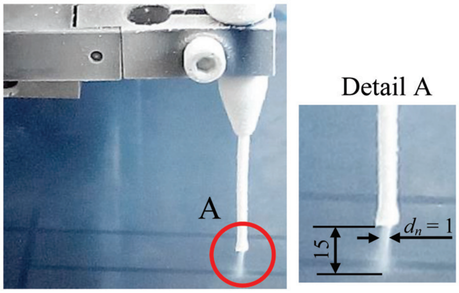

Fig. 3. *Cooling of the Inconel 718 plate with liquefied nitrogen (diameter of the nozzle d_n = 1 mm, distance nozzle-plate 15 mm)*

Fig. 4 shows the direction of the nozzle movement (the arrow) and the location of the thermocouples in different colours.

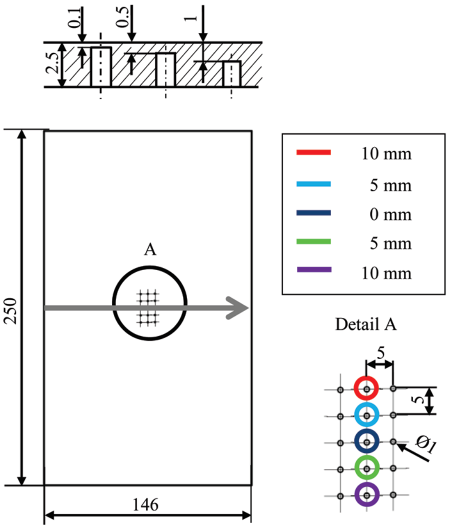

Fig. 4. *Shematic illustration of the moving nozzle with corresponding positions of the thermocouples and a cross section view of the holes at different depths*

Fig. 5 shows the measured temperature-time distribution for moving speed of v = 5 m/min. There are five temperature-time curves for each thermocouple positioned at the same depth (d = 0.5 mm) to provide enough information for describing temperature field in the plate.

The process of moving the nozzle across the plate lasted for 1.8 s, the difference to 2.4 s was predicted for balancing the heat flux in the system. It shows that the change in the material temperature is the biggest in the middle thermocouple marked with blue ΔT = 5.5 K.

The result is in accordance with the expectations since the nozzle moved across the middle of the plate. The minimum temperature was reached after 1.1 s, which means that there had been a delay in the process.

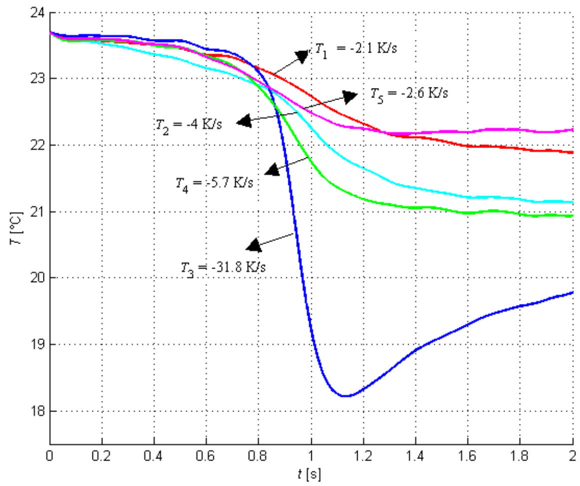

Fig. 5. *Temperature time distribution curve $T_{exp}(t)$ for Inconel 718 and time of the moving nozzle across the plate t = 1.8 s (v = 5 m/min and measured temperature at depth: 0.5 mm)*

The reason for this phenomenon is the forming of a gaseous nitrogen film which causes convective cooling of the material surface. While the nozzle was moving across the plate, it gradually pounded the convective insulated film which prevented higher cooling of the material.

The cooling rate is described by Eq. (4):

$$\left(\frac{dT}{dt}\right)_{max} = \frac{T_{max} - T_{min}}{t_2 - t_1}, \tag{4}$$

where T_{max} is temperature maximum and T_{min} is temperature minimum on the steepest part of the $T(t)$ curve. The results are shown in Table 2, where the cooling rates for all the mentioned curves are shown.

The results listed in Table 2 show that the middle thermocouple T_3 was subjected to cooling the most –31.8 K/s at the depth of 0.5 mm below the surface of Inconel 718. One of the reasons for slow cooling of Inconel 718 is also that it has low thermal conductivity (11.3 W/(mK)), as well as the above mentioned gaseous nitrogen film that is formed by the process of convection. For the numerical simulation design, the following parameters were chosen: v = 5 m/min, d = 0.5 mm, x = 0 mm and ΔT = 5.5 K, represented by curve T_3.

The cooling rate is also calculated, depending on the duration of the experiment, where the temperature at 0.1 mm below the surface was measured. The liquefied nitrogen jet was static and applied for such a long time until the balance between the liquid nitrogen jet and the temperature at the depth of 0.1 mm in Inconel 718 was reached. Fig. 6 shows the conducted experiment.

Table 2. *Maximum temperature rates at depth 0.5 mm from the surface*

Number of the curve	Distance from the moving nozzle x [mm]	$\left(\frac{dT}{dt}\right)_{max}$ [K/s]
T_1	10	–2.1
T_2	5	–4.0
T_3	0	–31.8
T_4	5	–5.7
T_5	10	–2.6

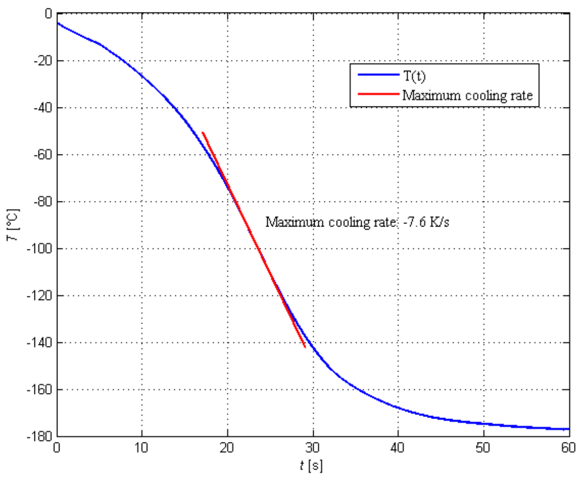

Fig. 6. *Temperature time distribution curve (experiment) corresponding to static nozzle and, measuring temperature at depth d = 0.1 mm*

The maxiumum cooling rate on the curve (Fig. 6) was calculated to be –7.6 K/s. The static experiment was conducted in order to show the impact of the static nozzle on the cooling rate of the Inconel 718 plate. The experiments with a moving nozzle show that there is a greater impact on the pounding of the convection gaseous film of nitrogen because the cooling rates were reached in a shorter time compared to the static nozzle experiment.

The static experiment tells that a static liquefied nitrogen jet has a lower capability to pound the gaseous nitrogen film, which consequently prolongs the time needed to reach the temperature balance. The convection of ambient air has impact on slower cooling of the plate.

3 NUMERICAL SIMULATION – SURFACE HEAT TRANSFER COEFFICIENT

In the current case, the numerical simulation was designed in Abaqus/Explicit 6.10. Finite element method was used. For simulating heat transfer through the mesh on the material, while using a fluid, the Eulerian formulation was used [23] and [25].

The reference parameters for the design of the numerical simulation were the following: v = 5 m/min, d = 0.5 mm in x = 0 mm. The depth of 0.5 mm was chosen since it had proven to be the most appropriate for simulating. At the depth of 0.1 mm, errors could have occured (measuring the temperature right under the surface).

The input parameters were: type of the formulation, mesh, the nozzle speed, the material mechanical and thermal properties data, as well as the initial and boundary conditions. The output parameter was the temperature. The mesh was chosen according to the geometry of each individual element in the system. The mesh was tetrahedral. All created components (the plate, the thermopaste and the thermocouple) had a finer net in the area of measuring temperature (Fig. 7). The length side of the triangle is marked with a (Fig. 7).

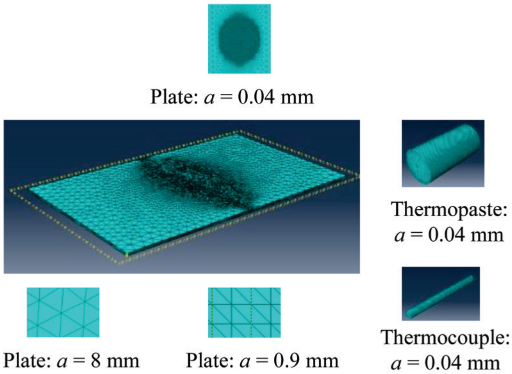

Fig. 7. *Mesh mode of the system*

Thermocouple and thermopaste were also created in the numerical simulation because of their different thermal properties, in order to describe the experiment completely and to reach the best possible result in the numerical simulation.

Fig. 8 shows the numerical simulation boundary conditions.

Dispersion of the liquefied nitrogen jet on the surface was assumed to be 4 mm × 4 mm. Two rectangles on the Fig. 8 present the liquefied nitrogen jet.

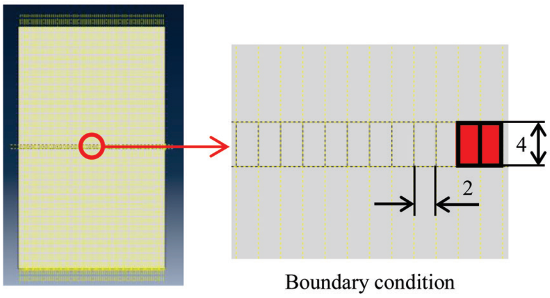

Fig. 8. *Boundary condition; the starting temperature of the system was 25 °C (initial boundary condition)*

Based on the width of the plate (146 mm), there were 73 rectangles. Based on the selected nozzle velocity (5 m/min) and the width of the particle (2 mm), the time period of the jet application was calculated. The temperature of the surface of each particle was –196 °C.

Mechanical (Young‘s modulus, Poisson ratio and density) and thermal (thermal conductivity and specific heat) properties of the materials used in the numerical simulation were adapted from the literature [26] to [28]. Because of a little temperature difference in Inconel 718, temperature dependant data for its properties were not considered. The thermocouple material for simulation was nickel which has approximately the same mechanical and thermal properties as chromium.

Temperature dependant thermal properties for the liquid nad gaseous phase of the nitrogen were adapted from Pušavec et al. [4]. The time gradient was 0.05 s.

According to the fitting of the two curves, the experimental $T_{exp}(t)$ and the simulation $T_{sim}(t)$, the thermal conductivity of the gaseous nitrogen film was determined (λ = 30 W/(mK)), as well as the surface heat transfer coefficient between liquid nitrogen and the workpiece.

According to this fact, it can be concluded that bubble boiling of the cryogenic media was suspected. It is assumed that the bubbles were dispersed and that they formed a gaseous nitrogen film.

Fig. 9 shows the temperature distribution in the nodals on the plate after the numerical simulation (t_{sim} = 2.4 s). In the numerical simulation, the cooling impact of the liquefied nitrogen jet on the whole surface of the Inconel 718 plate was taken into account. On the right side of the plate there is a wider area of cooling impact as a start point of entry to the nozzle plate. Fig. 10 shows the temperature distribution in the nodals across the depth of the plate after numerical simulation (t_{sim} = 2.4 s). The cooling impact of the liquefied nitrogen decreases with the increasing distance from the center where there were boundary conditions – velocity and the size of the surface jet on the plate.

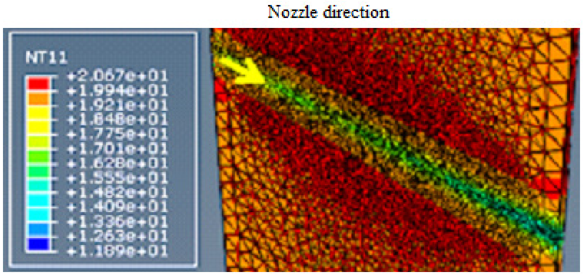

Fig. 9. Temperature distribution on the plate after numerical simulation, t_{sim} = 2.4 s (nozzle moving time, t_n = 1.8 s)

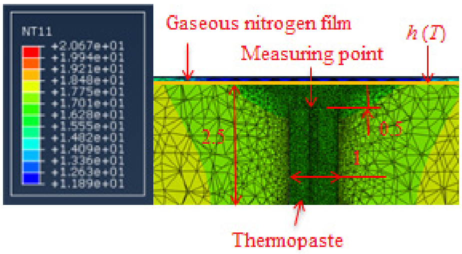

Fig. 10. *Temperature distribution across the Inconel 718 plate after numerical simulation, t_{sim} = 2.4 s*

At the transition between Inconel 718 and the thermopaste, the heat conductivity was defined, as well as at the transition between the thermopaste and the thermocouple.

The comparison between the experimental and the calculated $T(t)$ curve and consequently the values for the heat transfer coefficient between the coolant and the workpiece surface will be presented in the following part of the paper.

4 RESULTS

Fig. 11 shows the experimental and the simulation temperature-time $T(t)$ distribution curves. In the numerical simulation, a layer (l = 0.1 mm), which describes the gaseous phase of the nitrogen, has been designed.

A higher inconsistency between the curves occurs only in the initial part (t = 0 s to 0.9 s), where the experimental curve $T_{exp}(t)$ reaches a higher temperature gradient. This error in the numerical simulation is conditioned by the design of the gaseous nitrogen film which was constantly placed on the workpiece and did not change geometrically (simplification). The fitting between $T_{exp}(t)$ and $T_{sim}(t)$ curves is appropriate, given the simplification of the simulation conditions. At the start of the experiments, a preliminary experiment with input data: v = 1 m/min and d = 0.5 mm was conducted.

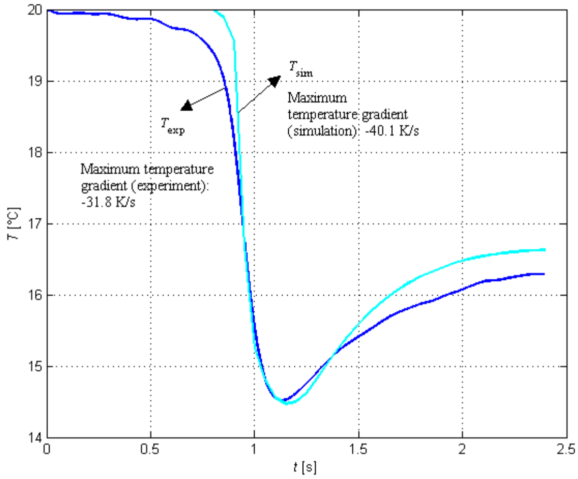

Fig. 11. *The comparison between experimental curve $T_{exp}(t)$ and simulation curve $T_{sim}(t)$*

Based on this experiment, a numerical simulation has been created to confirm the trend of the $T_{sim}(t)$ curve for v = 5 m/min and d = 0.5 mm. The trend was the same in both numerical curves and the same temperature difference as in the experiment was reached.

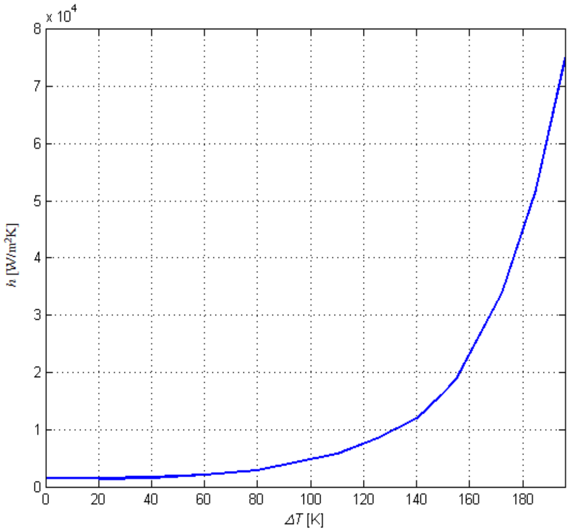

Fig. 12. *Surface heat transfer coefficent in dependance of the temperature difference between liquefied nitrogen and the workpiece (Inconel 718)*

According to the fitting of the two curves, the surface heat transfer coefficient between the coolant (gaseous nitrogen film) and Inconel 718 (Fig. 12) has been defined. The difference between the temperatures (the fluid T_{fluid} = –196 ˚C and the workpiece surface T_{body} = 25 ˚C) defines the surface heat transfer coefficient, calculated by the following Eq. (5) [17]:

$$q = h\left(T_{body} - T_{fluid}\right) = h \cdot \Delta T. \quad (5)$$

The comparable trend of the curve (Fig. 12) can be seen in the adapted paper [17].

5 CONCLUSIONS

For the past few decades, the increase of consumption of cooling lubrication fluids, which are not harmful to humans and the environment, was detected in researches. The idea has been developed in accordance to sustainable engineering. Liquefied nitrogen is one of the many media which can be used as a cooling lubrication fluid in green manufacturing. The benefits of the usage of liquefied nitrogen are: improved machinability of the material can be expected via improved (shorter) chips, reduced temperature in the cutting zone, improved surface roughness and more compressive residual stresses in the material.

The paper analyses thermal influences of liquefied nitrogen on workpiece material Inconel 718. It presents the process of solving the inverse problem for determining the surface heat transfer coefficient between liquefied nitrogen and workpiece depending on the temperature difference. The experiments where the temperature in the material was measured were performed in dependance on the different speeds of the moving nozzle across the plate.

Then the numerical simulation was designed to validate the experiment. The surface heat transfer coefficient between liquefied nitrogen and the workpiece surface was defined (based on the fitting of the experimental and simulation curves).

According to the results, the paper can give the following conclusions:

- The surface heat transfer coefficient is not a constant value but it decreases with increasing temperature of liquefied nitrogen (liquid to gas).
- The heat transfer coefficient between liquefied nitrogen and the Inconel 718 workpiece surface is the highest when nitrogen is in the liquid phase (around temperature difference ΔT = 196 ˚C, h = 75000 W/(m^{2}K)).
- Under temperature difference 160 K, a sharp fall to around 15000 W/(m^{2}K) can be detected, because of the nitrogen transformation from liquid to gaseous phase.
- The effect of conductance is reduced due to the formation of a gaseous nitrogen film (bubble boiling) which has got very low heat conductivity, around 0.03 W/(mK).
- The deviation between the experimental and the simulation curve is higher at the beginning of the process (t = 0 s to 0.8 s). It happens because of the nitrogen gaseous film which was being removed by the fluid jet which also cooled the workpiece surface in the experiment. In the simulation, the film was predicted and its characteristic did not change (were kept constant), therefore, such drop of temperature did not occur, contrary to the experiment.
- Summarizing the results, the limit where the heat transfer coefficient between liquefied nitrogen and the workpiece surface drops to the lowest value is when the temperature difference becomes 150 K. From there, it is possible to detect only air because whole nitrogen evaporates and there is only force air convection (1500 W/(m^{2}K)).

6 REFERENCES

[1] Maruda, R.W., Krolczyk, G.M., Feldshtein, E., Pusavec, F., Szydlowski, M., Legutko, S., Sobczak-Kupiec, A. (2016). A study on droplets sizes, their distribution and heat exchange for minimum quantity cooling lubrication (MQCL). *International Journal of Machine Tools and Manufacture*, vol. 100, p. 81-92, **DOI:10.1016/j.ijmachtools.2015.10.008**.

[2] Maruda, R.W., Legutko, S., Krolczyk, G.M., Raos, P. (2015). Influence of cooling conditions on the machining process under MQCL and MQL conditions. *Tehnički vjesnik – Technical Gazette*, vol. 22, no. 4, p. 965- 970, **DOI:10.17559/TV-20140919143415**.

[3] Pusavec, F., Deshpande, A., Yang, S., M'Saoubi, R., Kopac, J., Dillon, O.W. Jr., Jawahir, I.S. (2015). Sustainable machining of high nickel alloy - Inconel 718: Part 2 - Chip breakability and optimization. *Journal of Cleaner Production*, vol. 87, p. 941-952, **DOI:10.1016/j.jclepro.2014.10.085**.

[4] Pusavec, F., Courbon, C., Rech, J., Kopac, J., Jawahir, I.S. (2014). Importance of the nitrogen phase on the cryogenic machining performance. *ASME International Manufacturing Science and Engineering Conference*, **DOI:10.1115/MSEC2014-3992**.

[5] Pusavec, F., Hamdi, H., Kopac, J., Jawahir, I.S. (2011). Surface integrity in cryogenic machining of nickel- based alloy - Inconel 718. *Journal of Material Processing Technology*, vol. 211, no. 4, p. 773-783, **DOI:10.1016/j.jmatprotec.2010.12.013**.

[6] Thakur, A., Gangopadhyay, S. (2015). State-of-the-art in surface integrity in machining of nickel-based super alloys. *International Journal of Machine Tools and Manufacture*, vol. 100, p. 25-54, **DOI:10.1016/j.ijmachtools.2015.10.001**.

[7] Barron, R.F. (1999). *Cryogenic Heat Transfer Coefficient*. Taylor and Francis, Philadelphia.

[8] Yildiz, Y., Nalbant, M. (2008). A review of cryogenic cooling in machining processes. *International Journal of Machine Tools and Manafacture*, vol. 48, no. 9, p. 947-964, **DOI:10.1016/j.ijmachtools.2008.01.008**.

[9] Ding, Y., Hong, S.Y. (1995). *A Study of the Cutting Temperatures in Machining Processes Cooled by Liquid Nitrogen*. Socety of Mechanical Engineering, p. 95-113.

[10] Dhokia, V., Shokrani, C.A., Correa Paulino, D., Newman, S. (2012). Effects of Cryogenic Cooling on the Surface Quality and Tool Wear in End-Milling 6061-T6 Aluminium. *22nd International Conference on Flexible Automation and Intelligent Manufacturing*, p. 103-108.

[11] Pu, Z., Outeiro, J.C., Batista, A.C., Dillon, O.W. Jr., Puleo, D.A., Jawahir, I.S. (2011). Surface integrity in dry and cryogenic machining of AZ31B Mg alloy with varying cutting edge radius tools. *Procedia Engineering*, vol. 19, p. 282-287, **DOI:10.1016/j.proeng.2011.11.113**.

[12] Kida, M., Kikuchi, Y., Takahashi, O., Michiyoshi, I. (1981). Pool-boiling heat transfer in liquid nitrogen. *Journal of Nuclear Science and Technology*, vol. 18, no. 7, p. 501-513, **DOI:10.1080/18811248.1981.9733284**.

[13] Tsukamoto, O., Uyemura, T. (1980). Observation of bubble formation mechanism of liquid nitrogen subjected to transient heating. *Advances of Cryogenic Engineering*, Springer New York, p. 476-482, **DOI:10.1007/978-1-4613-9856-1_57**.

[14] Hong, S.Y., Ding, Y. (2001). Cooling approaches and cutting temperatures in cryogenic machining of Ti-6Al-4V. *International Journal of Machine Tools and Manufacture*, vol. 41, no. 10, p. 1417-1437, **DOI:10.1016/S0890-6955(01)00026-8**.

[15] Hong, S.Y., Ding, Y. (2001). Micro-temperature manipulation in cryogenic machining of low steel. *Journal of Material Processing Technology*, vol. 116, no. 1, p. 22-30, **DOI:10.1016/S0924-0136(01)00836-6**.

[16] Ambrosy, F., Zanger, F., Schulze, V., Jawahir, I.S. (2014). An experimental study of cryogenic machining on nanocrystalline surface layer generation. *Procedia CIRP*, vol. 13, p. 169-174, **DOI:10.1016/j.procir.2014.04.029**.

[17] Pusavec, F., Lu, T., Courbon, C., Rech, J., Aljancic, U., Kopac, J., Jawahir, I.S. (2016): Analysis of the influence of nitrogen phase and surface heat transfer coefficient on cryogenic machining performance. *Journal of Material Processing Technology*, vol. 233, p. 19-28, **DOI:10.1016/j.jmatprotec.2016.02.003**.

[18] Leinhard, J.H. IV, Lienhard, J.H. V (2008). *A Heat Transfer Textbook, 3rd ed.* Phlogiston Press Camridge, Massachusetts.

[19] Qpedia Thermal eMagazine (2015). Thermal-FluidsPedia Mass transfer, from *http://www.qats.com/Qpedia/Qpedia_Issue96.ashx* accesed on 2015-19-11.

[20] Chiavazzo, E., Ventola, L., Calignano, F. Manfredi, D., Asinari, P. (2014). A sensor for direct measurement of small convective heat fluxes: Validation and application to micro-structured surfaces. *Experimental Thermal and Fluid Science*, vol. 55, p. 42-53, **DOI:10.1016/j.expthermflusci.2014.02.010**.

[21] Maddox, D.E., Mudawar, I. (1989). Single- and two-phase convective heat transfer from smooth and enhanced microelectronic heat sources in a rectangular channel. *Journal of Heat Transfer*, vol. 111, no. 4, p. 1045-1052, **DOI:10.1115/1.3250766**.

[22] Azar, K, Tavassoli, B. (eds.) (2008) Understanding heat transfer coefficient. *Qpedia Thermal eMagazine*, vol. 1, no. 1-12, p. 32-35

[23] Arrazola, P.J., Özel, T., Umbrello, D., Davies, M., Jawahir, I.S. (2013). Recent advances in modeling of metal machining processes. *CIRP Annals – Manufacturing Technology*, vol. 62, no. 2, p. 698-715, **DOI:10.1016/j.cirp.2013.05.006**.

[24] Colaco, M.J., Orlande, H.R.B., Dulikravich, G.S. (2006). Inverse and optimization problems in heat transfer. *Journal of Brazilian Society of Mechanical Science and Engineering*, vol. 28, no. 1, p. 1-24, **DOI:10.1590/S1678-58782006000100001**.

[25] Arrazola, P.J., Özel, T. (2010). Investigations on the effects of friction modeling in finite element simulation of machining. *International Journal of Mechanical Sciences*, vol. 52, no. 1, p. 31-42, **DOI:10.1016/j.ijmecsci.2009.10.001**.

[26] Courbon, C., Sajn, V., Kramar, D., Rech J., Kosel, F., Kopac, J. (2011). Investigation of machining performance in high pressure jet assisted turning of Inconel 718: *A numerical model. Journal of Materials Processing Technology*, vol. 211, no. 11, p. 1834-1851, **DOI:10.1016/j.jmatprotec.2011.06.006**.

[27] Nickel Institute (2015). from *http://www.nickelinstitute.org/NickelUseInSociety*, accesed on 09-02-2015.

[28] ELPRO (2015). from *http://www.elpro.si/*, accesed on 2015-10-9.

Strojniški vestnik - Journal of Mechanical Engineering 62(2016)6, 340-350

DOI:10.5545/sv-jme.2015.3289
Original Scientific Paper
Received for review: 2015-12-11
Received revised form: 2016-03-23
Accepted for publication: 2016-04-18

Prediction of Cutting Forces in Ball-End Milling of Multi-Layered Metal Materials

Uroš Župerl* – Franci Čuš – Tomaž Irgolič
University of Maribor, Faculty of Mechanical Engineering, Slovenia

This paper outlines the experimental exploration of cutting forces produced during ball-end milling of multi-layered metal materials manufactured by the laser engineered net shaping (LENS) process. The research employs an artificial neural network (ANN) technique for predicting the cutting forces during the machining of 16MnCr5/316L four-layered metal material with a solid carbide ball-end mill. Hardness and thickness of the particular manufactured layer in above mentioned advanced material have been considered during training of the ANN model. Model predictions were compared with experimental data and were found to be in good agreement. Experimental results demonstrate that this method can accurately predict cutting force within a maximum prediction error of 4.8 %.
Keywords: end milling, cutting forces, multi-layered material, LENS, ANN

Highlights
- *Cutting forces generated in the machining of multi-layered metal materials were analysed.*
- *Hardness and thickness of the manufactured layer were considered in predictions.*
- *An artificial neural network methodology was used to predict the cutting forces.*
- *Verification of cutting force model is provided by comparison with experimental data.*

0 INTRODUCTION

End milling of multi-layered metal materials is an important manufacturing function in the automotive tool making industry. The most well-known process to fabricate the multi-layered materials was developed by Sandia National Laboratories and is known as laser engineered net shaping (LENS). The company Optomec makes and sells equipment based on Sandia's LENS process. LENS uses a laser power of up to 4 kW to fuse metal powders into three-dimensional structures layer by layer, guided by a CAD model. The process is enclosed in an airtight, argon environment which prevents oxidation. The closed-loop process controls ensure the geometric and mechanical integrity of the completed part [1]. Due to the inhomogeneous structure of multi-layered metal materials manufactured with the LENS process, the machining of these materials leads to undesirable effects such as tool breakage, rapid cutting tool wear, surface deterioration and shelling of the cladded layers (delayerization). All of these undesirable effects are directly connected to the cutting tool forces acting on the workpiece. Delayerization of material is tightly related to the cutting force normal to the layer deposition plane [2]. Cutting forces can be seen as a control parameter for many other phenomena involved in the milling of these materials. Therefore, there is a considerable practical interest to analyse and predict precisely the cutting forces during milling of multi-layered metal materials. Knowing the cutting forces is fundamental for understanding the cutting processes, optimizing the milling operations and evaluating the presence of instabilities that could affect the effectiveness of milling processes.

Many cutting force models have been developed for ball-end milling processes, especially the mechanistic models, including the work of Sui [3], Zhou [4] and Milfelner [5]. Mechanistic models try to relate the cutting forces to the chip geometry by experimentally determined cutting force coefficients. The major problem is the lack of cutting force coefficients for oblique cutting and for different tool/workpiece combinations, such as multi-layered laser based metal deposition (LBMD) materials. The coefficients are obtained by labour intensive and time-consuming cutting experiments and adjusting of model parameters. The problem is even more complicated due to the highly nonlinear and inhomogeneous nature of multi-layer LBMD materials as compared with metals. For these reasons, the generation of specific cutting energy data for LBMD materials is more challenging. No evidence of research efforts that attempts to model the cutting forces in milling LBMD materials has been found. Additionally, the obtained models are also difficult to extend to different tooling systems, conditions, and parameters.

An artificial neural network (ANN) can be used as an alternative to analytical approaches. The method has become widespread in the predictive modelling of milling processes [6] to [8]. ANNs determine an implicit relationship between the input(s) and output(s)

*Corr. Author's Address: University of Maribor, Faculty of Mechanical Engineering, Smetanova 17, Maribor, Slovenia, uros.zuperl@um.si

by learning from a training data set that represents the behaviour of a process. Zuperl [9] proposed a multilevel perceptron for on-line modelling of forces in ball-end milling. Das et al. [10] developed an ANN model to predict the surface roughness generated while machining a metal matrix composite. Dave et al. [11] also proposed a modified back-propagation ANN, which adjusts its learning rate and adds a dynamic factor in the learning process for the on-line modelling of the milling system. Mounayri et al. [12] replaced the back-propagation neural network with a new, more efficient and practical RBM neural network which is finally successfully implemented for the case of ball-end milling. Nevertheless, it should be mentioned that according to Navarro at al [13] the ANNs cannot produce better results than statistical methods when stochastic events are analysed. As a result, the ANN techniques in metal cutting are used less and less. Instead, intelligent statistical methods, such as the group method of data handling, are used.

This research employs a feedforward neural network in order to obtain a predictive cutting force model for the milling of four-layered metal material. The ANN predictive capabilities are used to capture the highly nonlinear relationship between machining parameters, tool angle rotation, LENS process parameters, and sensor readings.

The proposed method offers advantages such as automatic searching for the non-linear connection between the inputs and outputs, and no required knowledge of internal system parameters. The computational complexity of model does not increase much with the complexity of process, mathematically modelling-free and simple extending of the model with new input parameters and new data without modifying the existing model structure.

The most significant advantage of the proposed method is that once the experimental data are obtained and arranged, the prediction model for a specific tooling system can be built in a few minutes through training without any knowledge of statistics, machining cutting theory and programming.

By pressing a button in the application software, the processed data from experimental tests and corresponding parameters are automatically arranged in datasets for training and testing, then training and validating of the predefined architecture of ANN is performed. The validated neural model is then capable of predicting the cutting forces in end milling of specific multi-layered metal material.

This makes the proposed method more practical and appropriate for industrial application than predictive models based on cutting force coefficients.

The main drawback of the laser cladding process is the lack of knowledge about the machinability of the metal deposited materials. For LBMD materials, it is difficult to gather data related to the influence of the laser-cladding parameters on the produced cutting forces, flank wear, and surface roughness. Published research relating to the machinability of these materials is extremely scarce. Nevertheless, there are a few studies about the machinability of difficult-to-machine metal deposited materials, such as nickel-based alloys, titanium alloys, and composites. M´Saoubi [14] provided industrial perspectives in the context of machinability of specific alloys used in aerospace applications. He stated that the machinability of aerospace materials should be considered in much broader terms than machining tests that are directed at the tool performance/material removal rates. A group of researchers carried out mechanical [15] and machinability [14] assessment of a nickel-based superalloy (Inconel 718) in machining operations. Shokrani et al. [16] have reviewed and identified difficult-to-machine materials such as alloys used in the aerospace, nuclear and medical industries. Koyilada et al. [17] performed an evaluation of machinability characteristics of Nimonic C-263 using chemical vapour deposition (CVD) and physical vapour deposition (PVD) coated tools. Dong et al. [18] studied the chip formation during machining of nickel-based alloy Inconel 718 by observing chip metallographic graph. In this research, an experimental investigation was carried out to realize the machinability behaviour of the four-layered metal material in terms of the nature of the cutting force generated while performing the machining operation.

1 PREDICTIVE CUTTING FORCE MODELING

The aim of this research is to develop a methodology for predicting the cutting forces produced during ball-end milling of four-layered metal materials. This chapter outlines the adaptation of the ANN topology to the cutting force prediction problem. To carry out the modelling of the three cutting force components, a popular, three-layer architecture of feedforward neural network is used based on the back propagation learning algorithm. The developed ANN has seven input neurons for modelling: spindle speed n, feed rate f, axial depth of cutting A_D, radial depth of cutting R_D, the angle of cutting tool rotation Θ, cutting tool diameter D, the hardness of the machined material HV and the thickness of manufactured layer d. The number of hidden layers, the optimum number of neurons in the individual hidden layer and the training parameters were determined by simulations. The optimum ANN contains 3 and 6 neurons in hidden layers. The output from the ANN are three cutting force components; therefore, three output neurons are necessary. Signals passed through the neurons in the hidden and output layers are transformed by an ArcTangent activation function. Fig. 1 shows the detailed topology of the developed ANN-based cutting force prediction model.

Four steps are required to develop an ANN based cutting force model. In Step 1, the training and testing data sets were introduced to the ANN. A total of 525 scaled data points were utilized as the inputs and outputs to train the ANN.

Table 1 presents a list of 81 data sets (LENS test no. 6) used for training and testing of the ANN; 28 % of these data (highlighted sets) were used for ANN testing to verify the accuracy of the predicted values. Table 1 lists 11 % of the total 729 datasets (Table 2) obtained in the LENS end milling tests for the purpose of ANN modelling. The columns of Table 1 represent the ANN data set number, input vector, and output vector. The ANN topology and training parameters were defined in Step 2. A number of hidden layers, the number of neurons, momentum rate (β), learning rate (α), the overall error of the network and the maximal number of training iterations is defined. To evaluate the individual effects of training parameters on the performance of ANN 42 different networks were trained, tested and analysed. The ANN performances were evaluated using the two different criteria: average percentage error (APE) and the number of training iterations. The following conclusions can be drawn from the results of testing:

- The optimum number of hidden layer neurons for the prediction of cutting forces is 9; beyond this number, there is no significant improvement in the error prediction.
- If the training of the ANN is performed at learning rates (α) higher than 0.2, the network converges to a local minimum instead of the global minimum in the error space. It is set to 0.15 in hidden Layer 1 and 0.17 in Layer 2.
- To minimize the estimation errors, β should be between 0.008 and 0.01. It is set to 0.01 in both hidden layers.
- Networks trained with the ArcTangent transfer function give the least prediction errors, while those employing sigmoid and sine give the highest prediction errors respectively; Networks that employ the sine function require the lowest number of training cycles followed by the ArcTangent.

In Step 3, the training and testing phase is performed. During the training stage, the ANN adjusts its internal structure by adjusting the interconnection weights on the synapses in order to give correct output

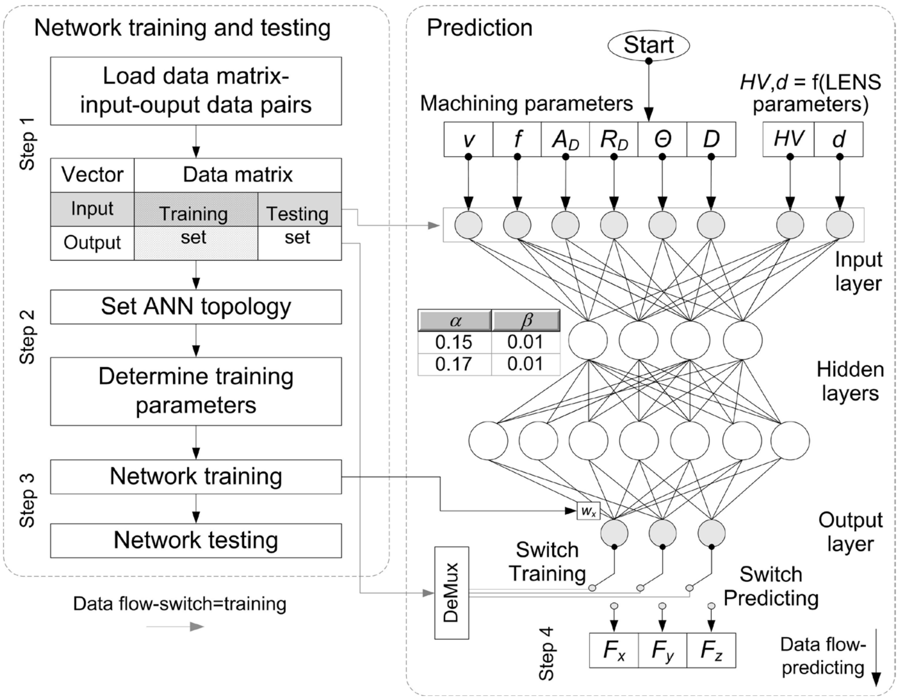

Fig. 1. *Flow chart for training and employing the ANN-based cutting force model with its detail structure*

Table 1. *81 datasets for training and testing of neural network (LENS test no. 6)*

No.	n [min-1]	t [mm/min]	A_D [mm]	Θ [°]	F_x [N]	F_y [N]	F_z [N]
406	3000	200	0.5	25	181.9	179.4	-59.9
407	3000	200	0.5	50	195.6	195	-65.8
408	3000	200	0.5	75	7	11.2	5.8
409	3600	200	0.5	25	89.3	104.2	-34.7
410	3600	200	0.5	50	96	112.6	-38.2
411	3600	200	0.5	75	7.2	11.8	6
412	4000	200	0.5	25	38.8	59.2	-20.1
413	4000	200	0.5	50	32.9	66.32	-21.7
414	4000	200	0.5	75	6.4	11.4	-7.6
415	3000	250	0.5	25	193.1	186.6	-61.8
416	3000	250	0.5	50	207.6	204.9	-68.7
417	3000	250	0.5	75	5.6	12.3	-6.4
418	3600	250	0.5	25	105.8	119.6	40.1
419	3600	250	0.5	50	117.6	130.1	-43.6
420	3600	250	0.5	75	4.8	11.0	-6.4
421	4000	250	0.5	25	78.9	101.2	-33.8
422	4000	250	0.5	50	85.8	110.3	-37.5
423	4000	250	0.5	75	7.2	9.8	-4.4
424	3000	300	0.5	25	203.1	196.2	-65.8
425	3000	300	0.5	50	223.2	218.1	-73.1
426	3000	300	0.5	75	6.4	13.9	-9.2
427	3600	300	0.5	25	121.2	133.0	-44
428	3600	300	0.5	50	133.2	134.4	-48.4
429	3600	300	0.5	75	4.8	12.2	-5.2
430	4000	300	0.5	25	88.8	130.6	-42.2
431	4000	300	0.5	50	99.1	138.6	-47.3
432	4000	300	0.5	75	7.2	-3.6	-2.4
433	3000	200	1	25	206.4	204.1	-68.6
434	3000	200	1	50	189.9	187.7	-63.8
435	3000	200	1	75	6.0	9.8	-6.9
436	3600	200	1	25	110.2	132.6	-45
437	3600	200	1	50	101.2	118.8	-41.7
438	3600	200	1	75	7.6	10.6	-6.8
439	4000	200	1	25	100.1	123.8	-41.2
440	4000	200	1	50	90.1	114.4	-37.1
441	4000	200	1	75	5.6	12.2	-7.6
442	3000	250	1	25	247.2	238	-79.9
443	3000	250	1	50	225.6	219.0	-73.5
444	3000	250	1	75	5.2	11.8	-4.8
445	3600	250	1	25	145.2	153.1	-51.0
446	3600	250	1	50	130.7	140.8	-47.0
447	3600	250	1	75	6.8	9.4	-7.6
448	4000	250	1	25	106.7	129	-43.4
449	4000	250	1	50	99.2	117.8	-39.1
450	4000	250	1	75	6.8	12.2	-7.6
451	3000	300	1	25	190.3	205.1	-68.6
452	3000	300	1	50	177	184.5	-63.8
453	3000	300	1	75	7.2	10.6	-4.4
454	3600	300	1	25	151.2	158.4	-53.5
455	3600	300	1	50	139.1	146.9	-48.7
456	3600	300	1	75	4.8	10.6	-7.2
457	4000	300	1	25	102.0	151.8	-49.6
458	4000	300	1	50	81.1	147.8	-51.1
459	4000	300	1	75	-3.9	12.9	-4.8
460	3000	200	1.5	25	208.6	200.7	-86.3
561	3000	200	1.5	50	229.2	223	-75
462	3000	200	1.5	75	4.4	12.6	-5.6
463	3600	200	1.5	25	114.1	132.9	-44.6
464	3600	200	1.5	50	125.4	146.9	-49.5
465	3600	200	1.5	75	5.2	12.2	-4.4
466	4000	200	1.5	25	110.4	122.8	-40.5
467	4000	200	1.5	50	120.3	132.9	-44.0
468	4000	200	1.5	75	6.4	9.4	-7.6
469	3000	250	1.5	25	233.7	223.9	-75.5
470	3000	250	1.5	50	256.8	246.1	-82.1
471	3000	250	1.5	75	7.2	10.2	-6.0
472	3600	250	1.5	25	148.4	148.5	-50.7
473	3600	250	1.5	50	159.6	165	-55.1
474	3600	250	1.5	75	4.4	11.8	-5.6
475	4000	250	1.5	25	113.2	129.2	-43.7
476	4000	250	1.5	50	121.0	142.6	-48.1
477	4000	250	1.5	75	6.0	12.2	-6.4
478	3000	300	1.5	25	217.6	211.1	-69.5
479	3000	300	1.5	50	234.1	227.3	-76.4
480	3000	300	1.5	75	6.6	11.2	-5.3
481	3600	300	1.5	25	146.3	159.3	-54.1
482	3600	300	1.5	50	157.3	175.9	-58.8
483	3600	300	1.5	75	6.0	10.6	-6.4
484	4000	300	1.5	25	133.0	145.8	-50.2
485	4000	300	1.5	50	143.0	162.74	-54.6
486	4000	300	1.5	75	5.6	12.6	-6.4

LENS test no. 6 (P = 380 W, c = 60 mm/s);
Cutting tests no. 136 to 162.

results according to the input features. 525 sets of experimental data are used to conduct 500 iterations of training.

Training of the ANN is stopped when the prediction error reaches its global minimum within 500 training iterations. After the ANN had been trained, it was applied to 204 additional input-output data pairs that were excluded from the training process. This time, the values of the output vector were not supplied so that the ANN had to predict them. The predictions were compared to the cutting force measurements and the prediction errors were calculated. It was found out that the error of testing for the 204 examples was converged to 4 %, which is higher than the error of training (2.8 %).

Finally, in the fourth step, the trained ANN is used to predict cutting forces. Fig. 1 shows the basic flow chart for training the ANN and predicting the cutting forces via ANN.

2 EXPERIMENTAL PROCEDURE AND EQUIPMENT

To build the ANN model, experimental results were obtained according to the following procedure:

1. Nine four-layered metal workpieces with different layer thicknesses were produced. LENS process parameters at three levels are indicated in Table 2.
2. Thickness d and hardness HV of manufactured layers were measured.
3. The impact of LENS process parameters on the HV and d of the manufactured layer was examined.
4. A total of 243 machining tests were carried out to obtain cutting forces in three directions (Table 2); 27 tests were conducted on each workpiece. Three machining factors at three levels are indicated in Table 1. Each test was repeated three times under the same operating parameters.
5. The results of measured cutting forces were analysed and prepared for ANN training.

Table 2. *LENS parameters and corresponding machining tests numbers*

LENS test	P [W]	c [mm/s]	Machining test no. (n; f; A_D ; Θ)	ANN data set no.
1	300	30	1 to 27	1 to 81
2	300	48	28 to 54	82 to 162
3	300	60	55 to 81	163 to 243
4	380	30	82 to 108	244 to 324
5	380	48	109 to 135	325 to 405
6	380	60	136 to 162	406 to 486
7	400	30	163 to 189	487 to 567
8	400	48	190 to 216	568 to 648
9	400	60	217 to 243	649 to 729

The machining experiments were carried out on the CNC milling machine (type HELLER BEA02), under dry cutting conditions. The cutting forces in the feed F_x, normal F_y and axial directions F_z were measured with a Kistler (Type 9257) piezoelectric dynamometer. The dynamometer expresses some limitations since it is conditioned by the vibration of the surrounding system and by the transducer's natural frequency [19]. These parameters could affect the measurement accuracy when measuring cutting forces in high-speed machining. Relevant distortions of cutting force signals are not experienced if low tooth passing frequencies are used [19]. The cutting force measurements experiment in this research showed no need for dynamic compensation at employed, low tooth passing frequencies (133 Hz). However, to cleanse measured force signals of possible errors induced by vibrations of the surrounding systems, the signals were conditioned through a dual mode charge amplifier (Type 5001) with a low pass filter of 1 kHz cut-off frequency. The used filter is a one pole passive filter with second order Butterworth characteristic. The low pass filter is set to about one-third of the natural frequency of the dynamometer. The analogue force signal is then output to an NI 925A board control by the Labview software. To avoid the distortion, the first natural frequency of the dynamometer has to be at least 3 times higher than the cutting frequency. When the spindle speed is 4000 min^{-1} using the 2-flute end mill, the cutting frequency is 133 Hz. The natural frequency of the dynamometer should be therefore higher than 400 Hz to measure cutting force signals at the spindle speed of 4000 min^{-1}. The frequency bandwidth of Kistler 9257 dynamometer is, therefore, adequate for all of the machining cutting-force frequency regimes in this research due to relatively low spindle speeds.

The solid ball-end milling cutting tools (Tornado) of 8 mm diameter with two cutting edges, of 29.9° helix angle and 2.28° rake angle were used. The ball-end mills were made of a sintered tungsten carbide material K88UF with the hardness of 1770 HV. The cutting edges were coated with PVD-TiAlN coating.

The machining tests were carried out for all combinations of machining parameters and LENS process parameters. One and/or three values for the radial and axial depth of cut have been selected: R_{D1} = 0.2 mm; A_{D1} = 0.5 mm, A_{D2} = 1 mm, A_{D3} = 1.5 mm. The following values for spindle speed and feed rate have been selected: n_1 = 3000 min^{-1}, n_2 = 3600 min^{-1}, n_3 = 4000 min^{-1}; f_1 = 200 mm/min, f_2 = 250 mm/min, f_3 = 300 mm/min. The combination of three values for the laser power (P) and the cladding speed (c) was used to make the four-layered material: P_1 = 300 W, P_2 = 380 W, P_3 = 400 W; c_1 = 30 mm/s, c_2 = 48 mm/s, c_3 = 60 mm/s.

The workpiece material is made of a 16MnCr5 basic material and 4 stainless steel (316L) layers with a singular 0.3 mm to 1.0 mm thickness, length of 50 mm and width of 15 mm.

Nine such belts of stainless steel layers were cladded on a singular workpiece with the 60 mm thickness, length of 180 mm and width of 70 mm. By varying the two LENS process parameters, 9 different test workpieces (9 tests) of four-layered metal material with different layer hardness and thickness were produced on the Optomec LENS 850-R machine. The overlapping in all layers was set to 40 %. The diameter of laser ray was 0.8 mm. The experimental setup can be seen in Fig. 2.

The Vickers hardness of manufactured layers was measured by 7061 Zwick 3212 hardness tester. Layer thicknesses *d* of the manufactured metal material were measured with a Nikon Epiphot 300 Inverted Metallurgical Microscope.

3 THE IMPACT OF LENS PARAMETERS TO THE HARDNESS AND THICKNESS OF THE MANUFACTURED LAYER

The results that were obtained from the 9 tests performed on LENS machine are presented in Fig. 3. Two plots have been worked out to determine the

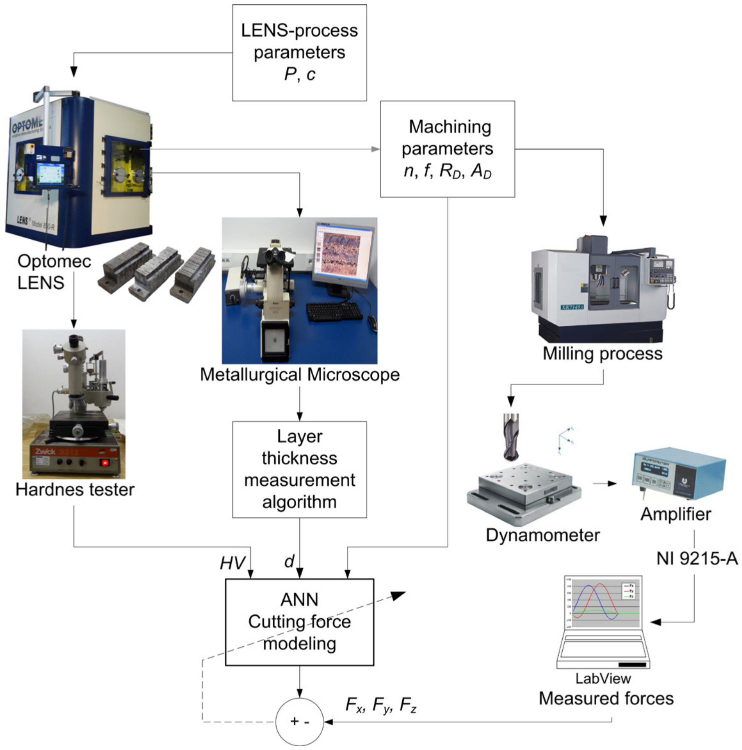

Fig. 2. *Experimental set-up*

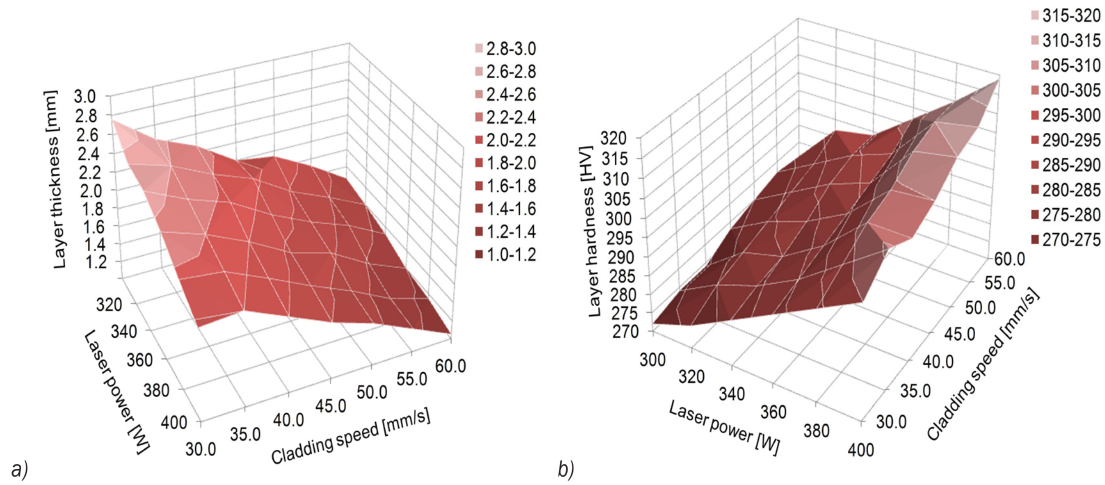

Fig. 3. *The impact of LENS parameters to the a) thickness and b) hardness of the manufactured layer*

variation of two LENS parameters with respect to the course of *HV* and *d*.

In the tests, it was found out that the laser power and a cladding speed have a significant impact on the *HV* and thickness *d* of the manufactured layer in the four-layered material.

Fig. 3b indicates that the layer hardness increases from 275 HV to 318 HV when the *P* increases from 300 W to 400 W at the constant cladding speed of 60 mm/s. Fig. 3b shows that the layer hardness increases gradually when the cladding speed increases at the same *P*. The relationship is close to a linear trend.

Fig. 3a shows that the manufactured layer thickness decreases when the cutting power and the cladding speed increases. The relationship is close to a linear trend. It was found out that the cladding speed has the largest impact on manufactured layer thickness.

4 INFLUENCE FACTORS AND ANALYSIS RESULTS OF MILLING FORCE

The prediction results and/or the values of measured cutting forces are graphically represented by means of diagrams depending on the angle of rotation of the cutting tool (Fig. 4). Samples of the cutting forces obtained during milling of the four-layered metal material are represented by a continuous line. The force signals outline the tool engagement in 1/2 revolution. Each force signal was obtained by averaging ten one-revolution engagements at different time periods in the cutting test in order to eliminate signal anomalies due to the inhomogeneity of the manufactured stainless steel layers. The force signals clearly outline one characteristic peak corresponding to the engagement of the one flute, separated by periods of no engagement. The rise of the cutting forces in each cycle is due to the increase of chip thickness from zero at the cutting edge entry to a maximum at the exit. The force signal is also influenced by the direction of layer cladding. The order in which the peak forces appear and the spacing between them is also related to the number of manufactured layers and their thickness.

The cutting forces for milling at the ratio A_D/d = 0.55 are relatively higher than expected for milling when the $A_D \approx d$ (Fig. 4). Force signals also exhibit more fluctuation. This is probably due to the material inhomogeneity at the border between

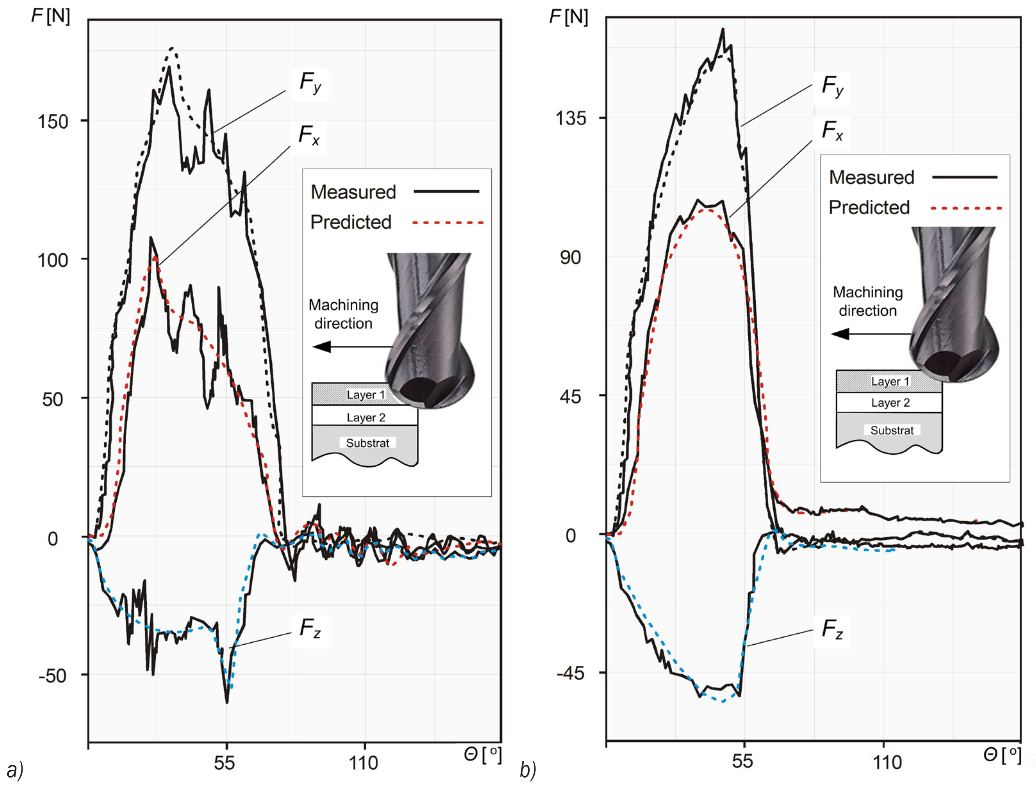

Fig. 4. *Comparison between experimental and predicted forces for 16MnCr5/316L four-layered material at: a) middle depth of cutting A_D = 0.45 d; (test no. 144); b) at high depth of cutting; $A_D/\approx d$; (test no. 163)*

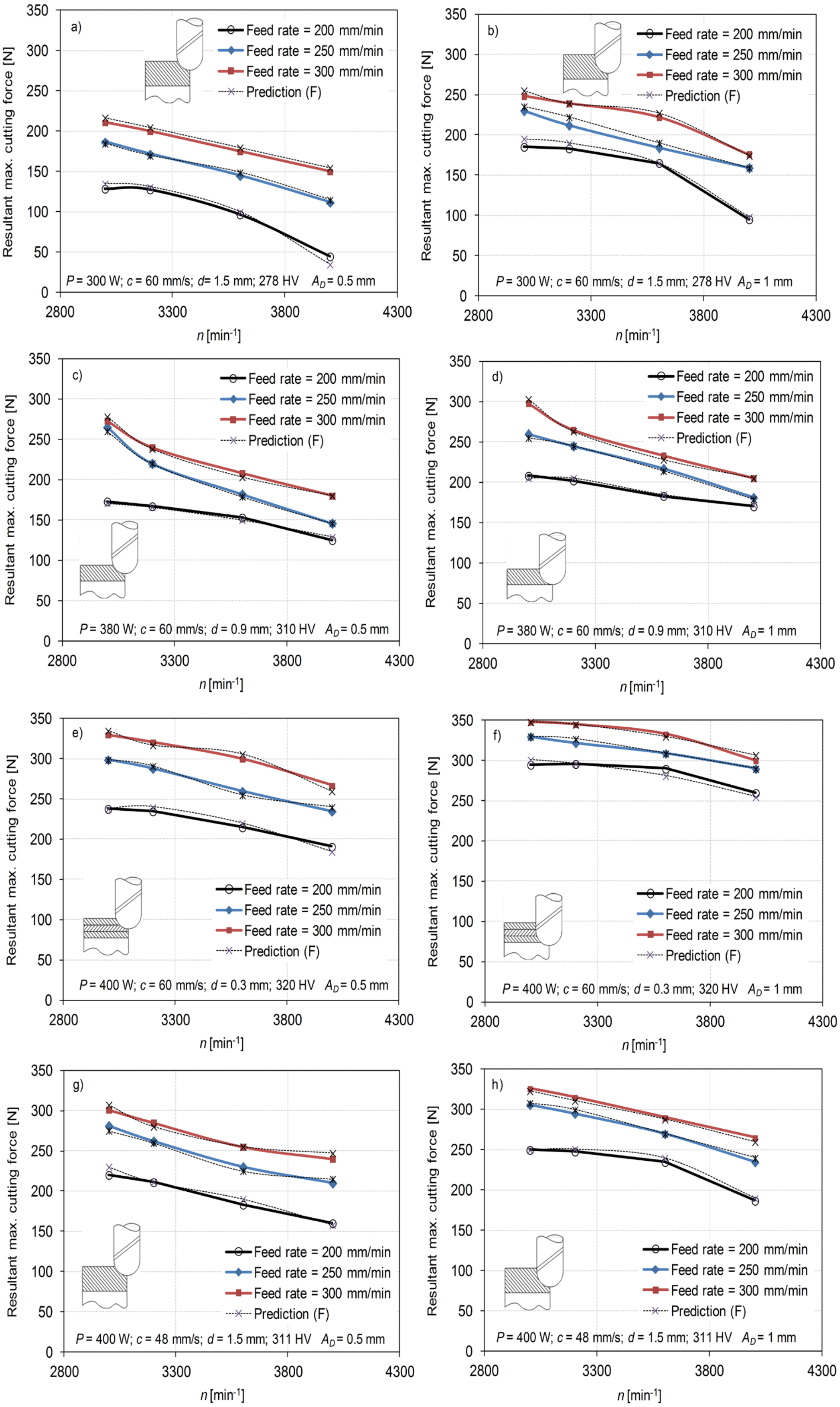

Fig. 5. *The effect of LENS and machining parameters to the directions of cutting force; comparison of the maximal values of measured and predicted cutting force*

separate stainless steel layers. The chip obtained in this region is heavily discontinuous and very small. Force fluctuations and magnitude increase slightly as A_D becomes larger than d.

Plots have been worked out to determine the variation of LENS and machining parameters with respect to the course of the resultant cutting force. A part of these plots were plotted in Fig. 5 to present the relationship of these operating parameters.

Fig. 5 shows that the cutting force decreases when the spindle speed increases at the same feed rate and depth of cut. The relationship is close to a linear trend. It was found that feed rate has the largest impact on cutting force.

The cutting force decreases when the feed rate decreases. It is also obvious that the force signal for the multi-layered material is characteristic of the architecture of the material, which depends on the LENS machine settings. Figs. 5a to f indicate that the cutting force increases significantly (up to 60 %) when the P setting increases from 300 W to 400 W at the constant c (60 mm/s) and constant machining parameters.

Figs. 5e and g outline that the F increases moderately (for 16 %) when the c increases from 48 mm/s to 60 mm/s at the constant P (400 W) and A_D. The analysis of the plots indicate that two-way (dual) effect interaction $P \times c$ has a significant effect on the value of the resultant cutting force F. It could be observed from Fig. 5 that the laser power setting has the second largest impact on the cutting force.

Figs. 5b, d, and f indicate that the cutting force increases significantly (by 40 %) when the manufactured layer thickness decreases (1.5 mm down to 0.3 mm) at the same cutting parameters.

By comparing Figs. 5f and g, it is found that when cutting with constant A_D = 1 mm at the ratio A_D/d = 3.3, the cutting forces are 8 % higher in comparison to cutting at the ratio A_D/d = 0.6. Therefore, the cutting forces are higher when the cutting involves more than one layer.

5 MODELING RESULTS AND DISCUSSION

Several experimental tests have been performed in order to validate the developed ANN model for different cutting conditions and LENS machine parameters.

The partial testing results of the ANN model are shown in Fig. 5. The results include data in which LENS parameters are different. The eight graphs on Fig. 5 compare the predicted values and measured values of maximal cutting forces. It could be observed from Fig. 5 that the predicted values of cutting force are very close to the experimental measurement values. The maximum percentage prediction cutting force error is found to be less than 4.8 % for all the cases tested.

A criterion in this experiment used to judge the efficiency of the model was the APE error, defined as:

$$APE = \frac{\sum_{i=1}^{m} \frac{\left| F^{\sim}{}_i - F_i \right|}{F^{\sim}{}_i} \cdot 100\,\%}{m}, \tag{1}$$

where $F^{\sim}{}_i$ is the actual cutting force component measured by the dynamometer, F_i is the predicted cutting force component generated by ANN and m is the size of sample data.

An example of test conditions for one LENS machine setting (LENS test no. 6) and cutting test no. 144 and 163 are given in Table 3. Table 3 lists the input and output of the prediction model results for cutting conditions, cutting tool rotation, layer thickness and cutting force components. It compares the experimental data and the predicted values of the cutting force components after training of the ANN model. The results mutually differ as follows: from 0.9 % to 4.7 % for F_x, from 0.3 % to 4.5 % for F_y and from 0.7 % to 3.7 % for F_z. Graphical comparisons between the experimental cutting forces and the predicted cutting forces for a machining example are shown in Fig. 4.

The results in Figs. 4a and b show that the ANN model provides good agreement with experimental results. The greatest difference between predictions and experimental results appear in the normal force on the boundary region between two cladded stainless steel layers (Fig. 4b). From Figs. 4a and b it can be seen that the values from prediction coincide well with the values from the experiments and, in addition, the process of the change of the cutting force with respect to the angle of rotation of the milling cutter and the amplitude agree well, with only slight differences in the peak and valley regions. The slight differences between the simulated and measured results are believed to be caused by the cutter runout, which is evident from the repeated tooth passing patterns in the measured forces. Fig. 6 shows the scatter diagram of the predicted values and measurement values of the F_x, F_y and F_z cutting forces of 100 sets of testing data. It shows that the predicted values of cutting forces follow the 45º line very closely. The predicted values are very close to the experimental measurement values. If the model is used outside training parameters or if the conditions are changed (tool/

Table 3. *Cutting force predictions, measurements, and APE errors for experiment with constant LENS machine settings (LENS test no. 6; P = 380 W, c = 60 mm/min)*

n [min^{-1}]	A_D [mm]	R_D [mm]	f [mm/min]	d [mm]	HV	Cutting test no. 144; ANN data set no. 460-432			
4000	0.5	0.2	300	0.9	310				
Angle of cutting tool rotation Θ [°]	Cutting force Measured F_x [N]	Cutting force Predicted F_x [N]	Error [%]	Cutting force Measured F_y [N]	Cutting force Predicted F_y [N]	Error [%]	Cutting force Measured F_z [N]	Cutting force Predicted F_z [N]	Error [%]
25	88.8	91.9	3.51	130.6	133.54	2.25	-42.2	-40.98	2.88
50	99.1	103.7	4.68	138.6	142.84	3.06	-47.3	-46.07	2.6
75	7.2	7.1	1.03	-3.6	-3.64	1.12	-2.4	-2.32	3.21
n [min^{-1}]	A_D [mm]	R_D [mm]	f [mm/min]	d [mm]	HV	Cutting test no. 163; ANN data set no. 457-459			
4000	1	0.2	300	0.9	310				
Angle of cutting tool rotation Θ [°]	Cutting force Measured F_x [N]	Cutting force Predicted F_x [N]	Error [%]	Cutting force Measured F_y [N]	Cutting force Predicted F_y [N]	Error [%]	Cutting force Measured F_z [N]	Cutting force Predicted F_z [N]	Error [%]
25	102.0	101.0	-0.95	151.8	153.48	1.11	-49.6	-48.33	2.56
50	81.1	78.8	2.89	147.8	152.32	3.06	-51.1	-51.62	1.01
75	-3.9	-3.7	-4.5	12.9	13.20	2.34	-4.8	-4.70	2.02

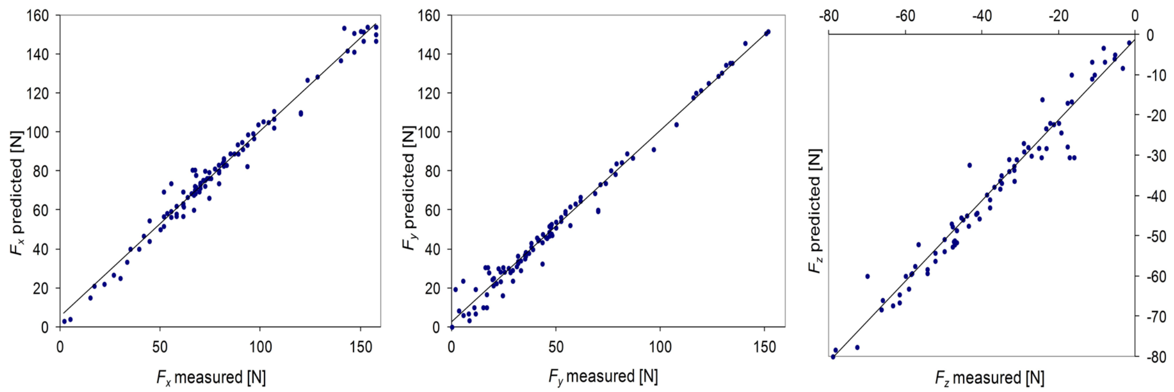

Fig. 6. *Scatter diagram of predicted and measured forces for testing data set*

workpiece combination), the ANN model has to be adapted via additional training with new experimental data in order to remain valid.

The reliability of an ANN model is determined by two factors: extrapolation and the local areas of poor fit. Finding exact reliability in multi-layered back-propagation network (BPN) is a non-deterministic polynomial-time hard (NP-Hard) problem [20], because BPNs do not have inherent ability to indicate the extrapolation and to calculate confidence limits on their predictions. If one attempted to train a BPN to recognize extrapolation, a comprehensive set of examples representing extrapolation would be needed. Forming such a training set is tantamount to solving the extrapolation problem in advance [20]. It is conceivable to add auxiliary outputs to a BPN to produce the output confidence intervals. However, this approach is also not efficient because of the need for extensive additional training [20].

6 CONCLUSIONS

The present research outlines the experimental investigation of cutting forces during computer numerical control (CNC) end-milling operation of four-layered metal material. Based on the experimental data the ANN approach was developed to predict the cutting forces while machining. Hardness and thickness of the particular manufactured layer in multi-layered metal material has been included in the input vector of the prediction model in order to improve the accuracy of predictions. The following conclusions can be drawn:

- Laser power and cladding speed have the largest impact on the hardness and thickness of the manufactured layer in the four-layered metal material.
- The layer thickness has a significant influence on predicted cutting forces.
- The cutting forces for milling at the ratio A_D/d = 0.55 are relatively higher than expected for milling when the $A_D \approx d$. Force signals also exhibit more fluctuation. This is probably due to the material inhomogeneity at the border between separate stainless steel layers. The chip obtained in this region is heavily discontinuous and very small. Force fluctuations and magnitude increase slightly as A_D becomes larger than d.
- The majority of the predicted cutting force values are equivalent to the appurtenant experimental values with negligible error.

Future activities will be carried out to implement the ANN model to the tool shop environment and to upgrade it with different tool/workpiece combinations.

7 REFERENCES

[1] Mahmoud, E.R.I. (2015). Characterizations of 304 stainless steel laser cladded with titanium carbide particles. *Advances in Production Engineering & Management*, vol. 10, no. 6, p. 115-124, **DOI:10.14743/apem2015.3.196**.

[2] Jahromi, A.S., Bahr, B. (2010). An analytical method for predicting cutting forces in orthogonal machining of unidirectional composites. *Composites Science and Technology*, vol. 70, no. 16, 2290-2297, **DOI:10.1016/j.compscitech.2010.09.005**.

[3] Sui, X.L., Zhang, J.T., Ge, J.H., Wang, Y. P. (2008). Modeling and simulation of milling force in virtual numerical control milling process. *Key Engineering Materials*, vol. 392, p. 697-702.

[4] Zhou, H.M., Deng, J.X., Xie, W.W. (2010). Milling force forecast of the matching of lengthened shrink-fit holder and cutter in high speed machining. *Advanced Materials Research*, vol. 139-141, p. 827-830, **DOI:10.4028/www.scientific.net/AMR.139-141.827**.

[5] Milfelner, M., Cus, F. (2003). Simulation of cutting forces in ball-end milling. *Robotics and Computer-Integrated Manufacturing*, vol. 19, no. 1-2, p. 99-106, **DOI:10.1016/S0736-5845(02)00066-2**.

[6] Aykut, Ş., Gölcü, M., Semiz, S., Ergür, H.S. (2007). Modeling of cutting forces as function of cutting parameters for face milling of satellite 6 using an artificial neural network. *Journal of Materials Processing Technology*, vol. 190, no. 1-3, p. 199-203, **DOI:10.1016/j.jmatprotec.2007.02.045**.

[7] Zuperl, U., Cus, F., Reibenschuh, M. (2012). Modeling and adaptive force control of milling by using artificial techniques. *Journal of Intelligent Manufacturing*, vol. 23, no. 5, p. 1805-1815, **DOI:10.1007/s10845-010-0487-z**.

[8] Klancnik, S., Ficko, M., Balic, J., Pahole, I. (2015). Computer vision-based approach to end mill tool monitoring. *International Journal of Simulation Modelling*, vol. 14, no. 4, p. 571-583, **DOI:10.2507/IJSIMM14(4)1.301**.

[9] Zuperl, U., Cus, F., Mursec, B., Ploj, T. (2006). A generalized neural network model of ball-end milling force system. *Journal of Materials Processing Technology*, vol. 175, no. 1-3, p. 98-108, **DOI:10.1016/j.jmatprotec.2005.04.036**.

[10] Das, B., Roy, S., Rai, R.N., Saha, S.C. (2016). Study on machinability of in situ Al–4.5% Cu–TiC metal matrix composite-surface finish, cutting force prediction using ANN. *CIRP Journal of Manufacturing Science and Technology*, vol. 12, p. 67-78, **DOI:10.1016/j.cirpj.2015.10.002**.

[11] Dave, H.K., Raval, H.K. (2010). Modelling of cutting forces as a function of cutting parameters in milling process using regression analysis and artificial neural network. *International Journal of Machining and Machinability of Materials*, vol. 8, no. 1-2, p. 198-208, **DOI:10.1504/IJMMM.2010.034496**.

[12] El-Mounayri, H., Kishawy, H., Briceno, J. (2005). Optimization of CNC ball end milling: a neural network-based model. *Journal of Materials Processing Technology*, vol. 166, no. 1, p. 50-62, **DOI:10.1016/j.jmatprotec.2004.07.097**.

[13] Navarro, H., Bennun, L. (2014). Descriptive examples of the limitations of artificial neural networks applied to the analysis of independent stochastic data. *International Journal of Computer Engineering & Technology*, vol. 5, p. 40-42.

[14] M'Saoubi, R., Axinte, D., Soo, S. L., Nobel, C., Attia, H., Kappmeyer, G., Engin, S., Sim, W.M. (2015). High performance cutting of advanced aerospace alloys and composite materials. *CIRP Annals-Manufacturing Technology*, vol. 64, no. 2, p. 557-580, **DOI:10.1016/j.cirp.2015.05.002**.

[15] Tabernero, I., Lamikiz, A., Martínez, S., Ukar, E., Figueras, J. (2011). Evaluation of the mechanical properties of Inconel 718 components built by laser cladding. *International Journal of Machine Tools and Manufacture*, vol. 51, no. 6, p. 465-470, **DOI:10.1016/j.ijmachtools.2011.02.003**.

[16] Shokrani, A., Dhokia, V., Newman, S.T. (2012). Environmentally conscious machining of difficult-to-machine materials with regard to cutting fluids. *International Journal of Machine Tools and Manufacture*, vol. 57, p. 83-101, **DOI:10.1016/j.ijmachtools.2012.02.002**.

[17] Koyilada, B., Gangopadhyay, S., Thakur, A. (2016). Comparative evaluation of machinability characteristics of Nimonic C-263 using CVD and PVD coated tools. *Measurement*, vol. 85, p. 152-163, **DOI:10.1016/j.measurement.2016.02.023**.

[18] Dong, G., Zhaopeng, H., Rongdi, H., Yanli, C., Muguthu, J.N. (2011). Study of cutting deformation in machining nickel-based alloy Inconel 718. *International Journal of Machine Tools and Manufacture*, vol. 51, no. 6, p. 520-527, **DOI:10.1016/j.ijmachtools.2011.02.011**.

[19] Scippa, A., Sallese, L., Grossi, N., Campatelli, G. (2015). Improved dynamic compensation for accurate cutting force measurements in milling applications. *Mechanical Systems and Signal Processing*, vol. 54-55, p. 314-324, **DOI:10.1016/j.ymssp.2014.08.019**.

[20] Kaushik, B., Banka, H. (2015). Performance evaluation of approximated artificial neural network (AANN) algorithm for reliability improvement. *Applied Soft Computing*, vol. 26, p. 303-314, **DOI:10.1016/j.asoc.2014.10.002**.

Strojniški vestnik - Journal of Mechanical Engineering 62(2016)6, 351-362

DOI:10.5545/sv-jme.2016.3423
Original Scientific Paper
Received for review: 2016-01-24
Received revised form: 2016-03-10
Accepted for publication: 2016-03-24

Nonlinear Vibrations of a Rotor-Fluid-Foundation System Supported by Rolling Bearings

Almatbek Kydyrbekuly[1] – Leyla Khajiyeva[1] – Alysher Ybraev Gulama-Garyp [1] – Julius Kaplunov[2]
[1]Al-Farabi Kazakh National University, Kazakhstan
[2]Keele University, United Kingdom

A generalized dynamic model taking into account coupled vibrations of a rotor-fluid-foundation system, linear eccentricity, damping, and rolling bearing nonlinearity is developed. The nonlinear equations of motion are formulated and analysed. Forced and free vibrations of the system are investigated. Peculiarities of the dynamic behaviour are revealed, including properties of vibration frequencies and amplitudes. The obtained results have the potential to be implemented in the optimal design of modern industrial devices.
Keywords: rotor, foundation, rolling bearing, nonlinear vibration, resonance, fluid, cavity

Highlights
- *A non-linear mathematical model for a rotor with a fluid filled cavity is developed.*
- *The equations of motion for a 'rotor-fluid-foundation' system are derived and solved.*
- *Simple explicit formulae for analysing eigen and forced vibrations are obtained.*
- *Conditions on problem parameters corresponding to the minimal pressure on supports and self-centring are presented.*

0 INTRODUCTION

High-speed rotating machines are widely spread in modern technology. Rotors and shafts are key components responsible for transmission of torque and rotation in the majority of power, electric and drilling systems [1] and [2]. In particular, these include gas turbines, compressors, separators, centrifugal pumps and textile machines, e.g. see [2] and [3].

Systems with fluid-filled cavities are an important class of rotating machines. Among them are elastic fluid turbines, fluid gyroscopes, centrifuges, and separators. A rotor with fluid-filled cavities is a non-conservative mechanical system [4] due to self-oscillation caused by the presence of fluid [5] and [6]. At supercritical speeds fluid converts rotor rotation energy into its transverse vibration energy resulting in instability [7] and [8]. Analysis of experimental data shows that fluid in rotor cavities is often the main cause of unstable regimes [9] and [10]. The underlying physics is that the fluid centrifugal acceleration is opposite to the pressure gradient leading to violation of equilibrium [11] and [12].

In addition to the above mentioned role of fluid, rotor dynamics is also affected by a few other parameters, e.g. see [13] and [14], including the variation of inertial characteristics, nonlinearity and stiffness of supports and shafts, rotor disbalance and asymmetry [15], specific properties of a lubrication layer in case of plain bearings [16] and, especially, performance of rolling bearings [17] and [18], internal and external damping, and some others.

Modern design and calculation of the vibration characteristics of rotating machines require treatment of the whole mechanical "rotor-fluid-foundation" system. Many theoretical and applied considerations on the subject concentrate on vibration of rotor and fluid only, neglecting foundation motion. Such assumption may considerably affect the accuracy of evaluation of the overall dynamic and kinematic behaviour of the system [19]. Experimental analysis clearly indicates the importance of taking into account foundation vibration along with the development of methods for its reduction [20] and [21].

Nowadays, the rotating machines widely used in industry mostly operate with rolling bearings [22] and [23]. Although plain bearings with liquid or gas lubrication have some advantages in comparison with rolling bearings, they have not yet found major industrial applications. The reason is that a lubrication layer induces high-amplitude self-oscillation in the system leading to a quick bearing failure [16] and [24]. In this case stresses in bearings are the result of the pressure in liquid films [25].

The increase in rotation speeds has natural restrictions due to the mechanical properties of rotating machines. At relatively low speeds design consists, as a rule, sufficient balancing. Ideally, dynamic stresses between the rotor and bearing supports and consequently induced vibrations disappear provided that the rotor principal inertia axis coincides with its

*Corr. Author's Address: School of Computing and Mathematics, Keele University, ST5 5BG, UK, j.kaplunov@keele.ac.uk

axis of rotation. In this case, some of the important bearing properties, including nonlinear deformability, are ignored [18]. However, at higher speeds the effect of bearing nonlinear deformability becomes essential.

Rotor dynamics in the case of nonlinear elastic supports, e.g. rolling bearings, has not been fully studied. A rolling bearing can be modelled as a rigid body support which is a hinge for a single row ball bearing and a clamped end for a support equipped with a pair of double row bearings. This simplified approach, however, does not produce a sufficiently accurate solution of the original engineering problem. The practice needs more general mathematical models incorporating far more specific features of rolling bearings, such as geometric uncertainties and gaps as well as their variation at exploitation [26] and [27], nonlinear stiffnesses [28] and [29], centrifugal forces, sophisticated behaviour of bearing rings, gyroscopic phenomena [30], friction in lubrication layers, variable thickness of lubrication layers along contact surfaces [16], etc.

In this paper, we investigate the nonlinear dynamics of a rotor with a fluid-filled cavity. The rotor is assumed to be supplied with rotation bearings and elastically supported by a foundation. The studied system models vertical centrifuges widely used for separation of various heterogeneous mixtures. The increase in rotation speeds along with the demand for a high precision performance motivates advanced modelling taking into account the deformability of rolling bearings. Their nonlinear behaviour seems to be essential for rotor dynamics. In particular, radial compression arises from deformations of rolling bodies along contact surfaces.

The challenge of the problem in question is also due to a strong coupling between the rotor and fluid motions affecting vibration frequencies and causing instability. The equations analysed in the paper govern rigid body fluid interaction. High-speed rotor modelling assumes evaluating the influence of the phenomena mentioned above in order to arrive at the most optimal problem formulation by preserving only its key features.

1 STATEMENT OF THE PROBLEM

Consider a symmetric vertical rotor of mass m with a cylindrical cavity of radius R partially filled with an ideal fluid, see Fig. 1. The angular speed of the rotor $\Omega_0 = const$ is considered to be greater than the associated critical speed. Let the rotor together with fluid perform rigid body rotation under dynamic equilibrium. We also assume static imbalance of the rotor, denoting it by e. The analysed system rests on rolling bearings. Elastic deformations arising in bearings are supposed to have both radial and axial components, demonstrating essential nonlinearity. The radial compliance of bearings is considered to occur due to the deformability of rolling elements and raceways along contact zones.

The equations of static equilibrium of a bearing may be derived from the Hertz theory. The nonlinear bearing stiffness is taken as $K(\delta) = c_0\delta + c_1\delta^3$, where δ is the minimal distance between the inner and outer rings of the bearing. The restoring force in radial bearings is obtained by a power series approximation. The outer ring is attached to a foundation of mass M resting on an elastic support with a linear stiffness coefficient c_2.

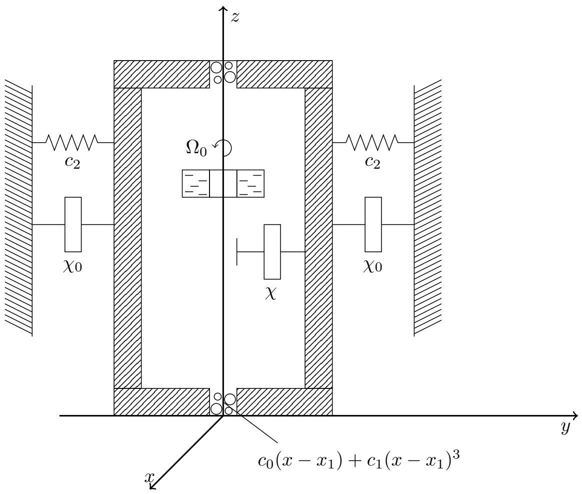

Fig. 1. *Rotor with rolling bearings resting on an elastic foundation*

Specify a Cartesian coordinate system *Oxyz* assuming that, in equilibrium, the geometric centre of the rotor and the centre of mass of the foundation both lie on the *Oz* axis. Below x and y are the coordinates of the rotor center, while x_1 and y_1 are the coordinates of the center mass of the foundation. We also use the notations c_0 and c_1 for rolling bearing stiffnesses, and χ and χ_0 stand for the coefficients of external damping.

We suppose that the rotor performs a plane-parallel motion, and the foundation has no rotation around coordinate axes. In this case, the equations of motion can be written as:

$$m\ddot{x}+2c_0(x-x_1)+2c_1(x-x_1)^3+\chi\dot{x}=$$
$$=me\Omega_0^2\cos\Omega_0 t+F_x,$$
$$m\ddot{y}+2c_0(y-y_1)+2c_1(y-y_1)^3+\chi\dot{y}=$$
$$=me\Omega_0^2\sin\Omega_0 t+F_y,\quad \text{and}$$
$$M\ddot{x}_1+2c_2x_1-2c_0(x-x_1)-2c_1(x-x_1)^3+\chi_0\dot{x}_1=0,$$
$$M\ddot{y}_1+2c_2y_1-2c_0(y-y_1)-2c_1(y-y_1)^3+\chi_0\dot{y}_1=0, \quad (1)$$

where F_x and F_y are the components of the fluid reaction force given by:

$$F_x=Rh\int_0^{2\pi}P|_{r=R}\cos(\Omega_0 t+\varphi)d\varphi, \quad (2)$$

$$F_y=Rh\int_0^{2\pi}P|_{r=R}\sin(\Omega_0 t+\varphi)d\varphi. \quad (3)$$

Here h is the height of the cavity and P is the fluid pressure along the wall of the rotor.

The equations of fluid motion can be written as, e.g. see [6],

$$\frac{\partial u}{\partial t}-2\Omega_0\upsilon=$$
$$=-\frac{1}{\rho}\frac{\partial P}{\partial r}-\ddot{x}\cos(\Omega_0 t+\varphi)-\ddot{y}\sin(\Omega_0 t+\varphi),$$
$$\frac{\partial \upsilon}{\partial t}+2\Omega_0 u=$$
$$=-\frac{1}{\rho r}\frac{\partial P}{\partial\varphi}+\ddot{x}\sin(\Omega_0 t+\varphi)-\ddot{y}\sin(\Omega_0 t+\varphi). \quad (4)$$

The continuity equation at $\rho = const$ is:

$$\frac{\partial(ur)}{\partial r}+\frac{\partial\upsilon}{\partial\varphi}=0. \quad (5)$$

The boundary conditions take the form: the impenetrability condition:

$$u|_{r=R}=0, \quad (6)$$

the condition on a free fluid surface:

$$P|_{r=r_0}=0 \quad \text{or} \quad \frac{\partial P}{\partial t}=-\rho\Omega_0{}^2 r_0 u|_{r=r_0}. \quad (7)$$

In the formulae above, u and υ are radial and circumferential components of fluid velocity, ρ is fluid density, r_0 is the free surface radius, r and φ are cylindrical polars.

2 SOLUTION OF EQUATIONS OF MOTION

First, solve the equations of fluid motion Eqs. (4) to (7) using the stream function Φ and the velocity potential ψ. In this case, the components of fluid velocity become:

$$u=\frac{\partial\Phi}{\partial r},\ \upsilon=\frac{1}{r}\frac{\partial\Phi}{\partial\varphi} \quad \text{or} \quad u=\frac{1}{r}\frac{\partial\psi}{\partial\phi},\ \upsilon=-\frac{\partial\psi}{\partial r}. \quad (8)$$

Then, on introducing the expressions for u and υ from Eq. (8) into the Eq. (4), we obtain:

$$grad\left\{\frac{\partial \$}{\partial t}+2\Omega_0\psi+\frac{P}{\rho}+r[\ddot{x}\cos(\Omega_0 t+\phi)+\right.$$
$$\left.+\ddot{y}\sin(\Omega_0 t+\phi)]\right\}=0. \quad (9)$$

Furthermore, the continuity equation can be rewritten as:

$$\Delta\Phi=0, \quad (10)$$

where Δ is the Laplace operator specified in cylindrical polar coordinates.

From Eq. (9), we determine the expression for fluid pressure as:

$$P=-\rho\left\{\frac{\partial\Phi}{\partial t}+2\Omega_0\psi+r[\ddot{x}\cos(\Omega_0 t+\phi)+\right.$$
$$\left.+\ddot{y}\sin(\Omega_0 t+\phi)]\right\}. \quad (11)$$

In terms of the complex variables:

$$x+iy=z,\ \text{and}\ \ x_1+iy_1=z_1. \quad (12)$$

Eq. (11) takes the form:

$$P=-\rho\left[\frac{\partial\Phi}{\partial t}+2\Omega_0\psi+\ddot{z}r\exp(-i(\Omega_0 t+\varphi))\right]. \quad (13)$$

In the case of time-harmonic vibrations of the rotor and foundation, the complex variables z and z_1 can be presented as, see [4] to [12],

$$z=A\exp(i\Omega_0 t)+B\exp(i\omega t), \quad (14)$$

$$z_1=C\exp(i\Omega_0 t)+D\exp(i\omega t), \quad (15)$$

where ω is the eigenfrequency.

The harmonic function Φ and the function ψ taking into account Eq. (14) become:

$$\Phi=R_2(r)\exp(i(\sigma t-\varphi)), \quad (16)$$

$$\psi=R_1(r)\exp(i(\sigma t-\varphi)), \quad (17)$$

where $\sigma=\omega-\Omega_0$.

On substituting the last expression for the stream function Φ into Eq. (10), we obtain:

$$R_2(r)=C_1 r+\frac{C_2}{r}. \quad (18)$$

We also get for the function ψ, see Eq. (8),

$$R_1(r) = i\left(C_1 r - \frac{C_2}{r}\right). \tag{19}$$

The constants C_1 and C_2 can be found from the boundary conditions in Eqs. (6) and (7). Then, by inserting Eq. (13) into Eqs. (2) and (3) and taking into account Eqs. (16) to (19), we obtain a formula for the complex force F_r. It is:

$$F_r = F_x + iF_y = Am_L\Omega_0^{\,2} exp(i\Omega_0 t) +$$
$$+Bm_L\omega^2 \frac{(\sigma^2 - 2\Omega_0\sigma - \Omega_0^{\,2})}{(\gamma\sigma^2 - 2\Omega_0\sigma - \Omega_0^{\,2})} exp(i\omega t), \tag{20}$$

with $q = \dfrac{R}{r_0}$, $\gamma = \dfrac{q^2+1}{q^2-1}$ and $m_L = \pi\rho R^2 h$. Here m_L is the mass of fluid inside the cavity, and γ characterises the relative fluid volume.

It is clear that in Eq. (1) the first and third equations are identical to the second and fourth equations, respectively. To this end, below we restrict ourselves to two equations in x and x_1:

$$\ddot{x} + n_0^{\,2}(x - x_1) + n_1(x - x_1)^3 + 2k\dot{x} =$$
$$= e\Omega_0^2 cos\Omega_0 t + Re\left(\frac{F_r}{m}\right),$$
$$\ddot{x}_1 + n_2^{\,2}x_1 - n_{01}^{\,2}(x - x_1) - n_{10}(x - x_1)^3 + 2k_0\dot{x}_1 = 0, \tag{21}$$

where

$$n_0^{\,2} = \frac{2c_0}{m},\ n_1 = \frac{2c_1}{m},\ 2k = \frac{\chi}{m},\ n_2^{\,2} = \frac{2c_2}{M},$$
$$n_{01}^{\,2} = \frac{2c_0}{M} = \mu n_0^{\,2},\ n_{10} = \frac{2c_1}{M} = \mu n_1,\ 2k_0 = \frac{\chi_0}{M},\ \mu = \frac{m}{M}.$$

On substituting the real parts of Eqs. (14), (15) and (20) into Eq. (21), we obtain, similarly to the derivations in **[6]** and **[12]**, a set of algebraic equations in the unknowns *A, B, C* and *D*. Then,

$$C = P_0 + iP_1 + A(P_2 + iP_3) \quad \text{and} \quad D = (P_4 + iP_5)B, \tag{22}$$

with

$$P_0 = \frac{\mu e\Omega_0^{\,2}(n_2^{\,2} - \Omega_0^{\,2})}{m_0},\ P_1 = -\frac{2k_0\Omega_0^{\,3}}{m_0},$$

$$P_2 = \frac{\mu[(1+\mu_L)\Omega_0^{\,2}](n_2^{\,2} - \Omega_0^{\,2}) - 4kk_0\Omega_0^{\,2}}{m_0},$$

$$P_3 = -\frac{2\mu[(1+\mu_L)\Omega_0^{\,2}k_0 + (n_2^{\,2} - \Omega_0^{\,2})k]\Omega_0}{m_0}$$

$$P_4 = \frac{\mu\omega^2(n_2^{\,2} - \omega^2)\left(1 + \mu_L\dfrac{D_3}{D_4}\right) - 4kk_0\omega^2}{m_1}, \text{ and}$$

$$P_5 = -\frac{2\mu[(1+\mu_L\dfrac{D_3}{D_4})k_0\omega^2 + (n_2^{\,2} - \omega^2)k]\omega}{m_0}.$$

In the above $\mu_L = \dfrac{m_L}{m}$ and

$$m_1 = (n_2^{\,2} - \omega^2)^2 + 4k_0^{\,2}\omega^2,$$
$$m_0 = (n_2^{\,2} - \Omega_0^{\,2})^2 + 4k_0^{\,2}\Omega_0^{\,2},$$
$$D_3 = \sigma^2 - 2\Omega_0\sigma - \Omega_0^{\,2},$$
$$D_4 = \gamma\sigma^2 - 2\Omega_0\sigma - \Omega_0^{\,2},$$
$$D = (P_4 + iP_5)B. \tag{23}$$

From the last formulae, we obtain algebraic equations for *A* and *B*, i.e.

$$\frac{3n_{10}P_{75}P_{23}}{2}\left(P_{23}A^2 - 2P_{01}A\right) - e_2P_{45} +$$
$$+(n_{01}^2 + \frac{3n_{10}}{2}P_{01}^{\,2})P_{75} + \frac{3n_{10}}{4}P_{75}^{\,3}B^2 = 0,$$
$$\frac{3}{4}n_{10}P_{23}^{\,3}A^3 - \frac{9}{4}n_{10}P_{01}P_{23}^{\,2}A^2 + [P_{23}(n_{01}^2 + \frac{9}{4}n_{01}P_{01}^{\,2}) -$$
$$-e_0P_{23}^{\,*}]A - (e_0 + n_{01}^{\,2} + \frac{3}{4}n_{10}P_{01}^{\,2})P_{01} +$$
$$+\frac{3}{2}P_{75}^{\,2}n_{10}(P_{23}A - P_{01})B^2 = 0. \tag{24}$$

Here

$$P_{01} = P_0 + iP_1,\ P_{23} = 1 - P_2 - iP_3,\ P_{45} = P_4 + iP_5,$$
$$P_{75} = P_7 - iP_5,\ P_7 = 1 - P_4,\ P_{23}^{\,*} = P_2 + iP_3,$$
$$e_0 = n_2^{\,2} - \Omega_0^{\,2} + 2ik_0\Omega_0,\ e_2 = n_2^{\,2} - \omega^2 + 2k_0 i\omega.$$

Now, we determine B^2 from the first equation in Eq. (24) and substitute it into the second equation. As a result, we obtain a third order equation for *A* which can be easily solved, for example, using the Cardano formula. Finally, we have the constants *C* and *D* from Eq. (22). The derived formulae for *A, B, C* and *D* are typical for nonlinear systems demonstrating a specific relation between coefficients.

The developed approach can be extended to a cavity filled with viscous fluid. It might be expected that the nonlinear elastic properties of bearings should not considerably affect the motion of a viscous fluid. In fact, the ideal fluid approximation assumed in the paper has been implemented only because this results in a relatively simple formulae useful for potential engineering applications.

3 FREE NONLINEAR VIBRATIONS OF THE ROTOR WITH CAVITY PARTIALLY FILLED WITH FLUID

Consider a rotating system neglecting imbalance and concentrating on nonlinear vibrations of a rotor with a partially fluid filled cavity resting on an elastic foundation. The equations of motion neglecting imbalance take the form:

$$\ddot{x}+n_0{}^2(x-x_1)+n_1(x-x_1)^3+2k\dot{x}=Re\left(\frac{F_r}{m}\right),$$

$$\ddot{x}_1+n_2^2x_1-n_{01}{}^2(x-x_1)-n_{10}(x-x_1)^3+2k_0\dot{x}_1=0, \quad (25)$$

where the former notations are adapted and the force F_r is expressed as [12]:

$$F_r=Bm_L\omega^2\frac{\left(\sigma^2-2\Omega_0\sigma-\Omega_0^2\right)}{\left(\gamma\sigma^2-2\Omega_0\sigma-\Omega_0^2\right)}exp(i\omega t). \quad (26)$$

As above, we seek the solution in the form:

$$x=B\exp(i\omega t), \quad (27)$$

$$x_1=D\exp(i\omega t). \quad (28)$$

On substituting Eqs. (27) and (28) into Eq. (25) and using the same procedure as in the previous section, we obtain:

$$D=P_8B, \quad (29)$$

where $P_8=P_9+iP_{10}$,

with $P_9=\dfrac{\mu\left[\tau^2D_6(n_{02}{}^2-\tau^2)-4k_{01}\tau^2\right]}{g_0}$,

and $P_{10}=\dfrac{-2\mu[k_{10}(n_{02}{}^2-\tau^2)+\tau^2k_{00}}{g_0}$.

In the above:

$$g_0=(n_{02}{}^2-\tau^2)^2+4k_{00}{}^2\tau^2,$$

$$D_6=1+\mu_L\frac{\tau^2-4\tau s+2s^2}{\gamma\tau^2-2(\gamma+1)\tau s+(\gamma+1)s^2},$$

and $n_{02}=\dfrac{n_2}{n_0}, k_{00}=\dfrac{k_0}{n_0}, k_{01}=\dfrac{k_0k}{n^2{}_0}, k_{10}=\dfrac{k}{n_0}.$

Here $\tau=\omega/n_0$ and $s=\Omega_0/n_0$ are dimensionless eigenfrequency of the system and rotor angular speed, respectively.

It follows from the second equation in Eq. (25) that:

$$g_1P_8=\mu\left(1-P_8\right)+\frac{3\mu c_{10}}{4}\left(1-P_8\right)^3B^2,$$

where $g_1=(n^2{}_{02}-\tau^2)+2ik_{00}\tau$ and $c_{10}=\dfrac{c_1}{c_0}$.

The formulae for B and D can be derived from the last equation and Eq. (29), respectively. They are:

$$B=\sqrt{\frac{4\left[g_1P_8-\mu(1-P_8)\right]}{3\mu c_{10}(1-P_8)^3}},$$

and $D=\left(P_9+iP_{10}\right)\sqrt{\dfrac{4\left[g_1P_8-\mu(1-P_8)\right]}{3\mu c_{10}(1-P_8)^3}}$.

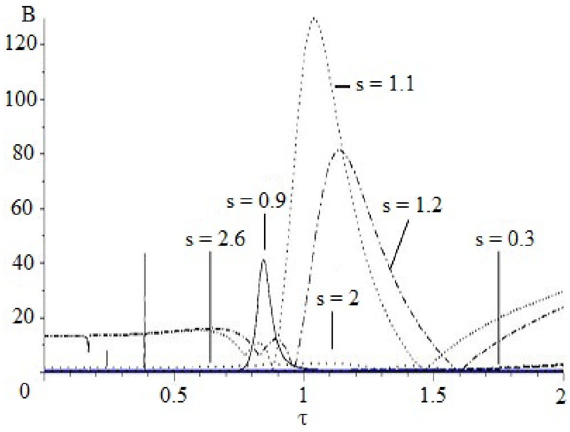

Fig. 2. *Rotor amplitude $B=B(\tau,s)$ at γ = 15.24, taking into account damping*

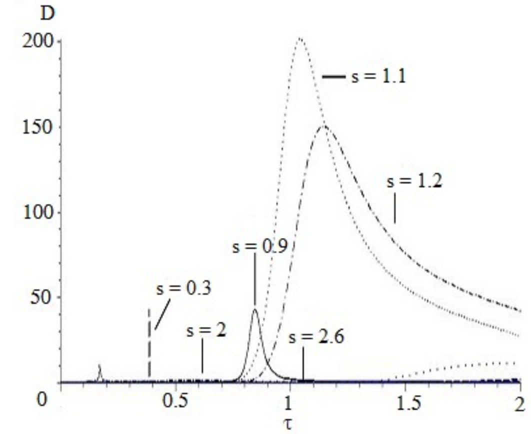

Fig. 3. *Foundation amplitude $D=D(\tau,s)$ at γ = 15.24, taking into account damping*

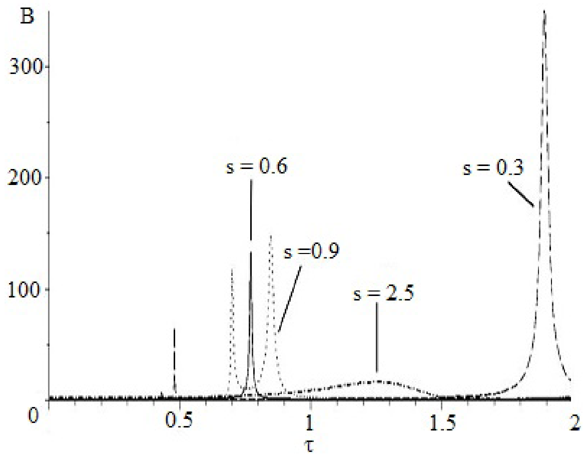

Fig. 4. *Rotor amplitude $B = B(\tau,s)$ at γ = 4.56, taking into account damping*

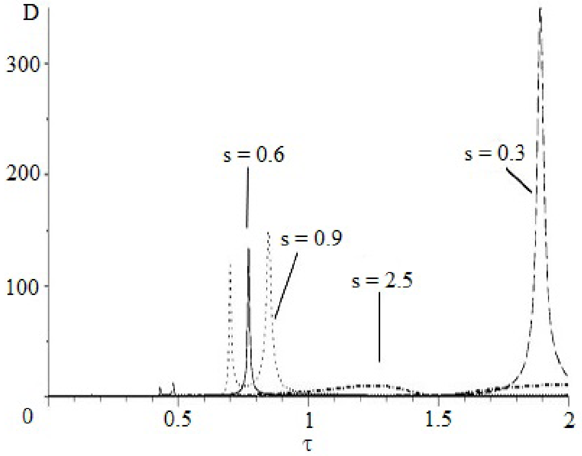

Fig. 5. *Foundation amplitude $D = F(\tau,s)$ at γ = 4.56, taking into account damping*

Below, we use the same notation for the modulae of these complex-valued quantities, i.e.

$$B \equiv \sqrt{\left(\operatorname{Re} B\right)^2 + \left(\operatorname{Im} B\right)^2}, \tag{30}$$

$$D \equiv \sqrt{\left(\operatorname{Re} D\right)^2 + \left(\operatorname{Im} D\right)^2}. \tag{31}$$

It is clear that the free vibration amplitudes of the rotor B and the foundation D depend on the vibration frequency ω of the nonlinear system in question. The formulae above enable calculating amplitude vs frequency graphs at a fixed angular speed of the rotor.

4 NUMERICAL RESULTS

Let us study the rotor and foundation amplitudes determined in the previous section. In Figs. 2 to 11 graphs demonstrating unstable self-oscillation zones of the rotor (B) and foundation (D) versus the parameters τ and s are presented for various values of the quantity γ characterizing the relative fluid volume in the cavity. A substantial increase in the self-oscillation amplitude, which is bounded due to external damping, is observed.

For a small fluid volume in the rotor cavity (γ=15.24 (r_0=0.93R) in Figs. 2 and 3) we obtain two zones of unstable self-oscillation of the rotor and foundation. Note that over the angular speed

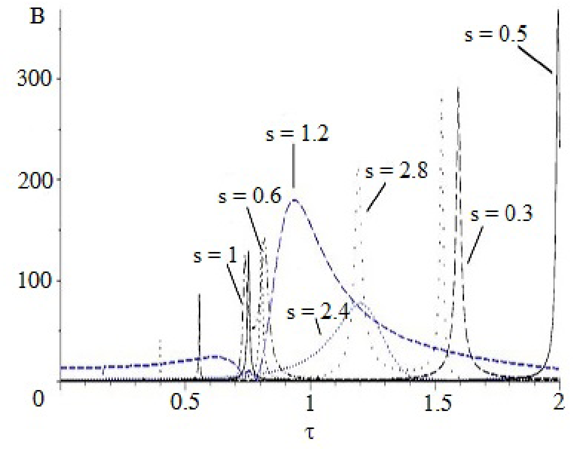

Fig. 6. *Rotor amplitude $B = B(\tau,s)$ at γ = 2.6, taking into account damping*

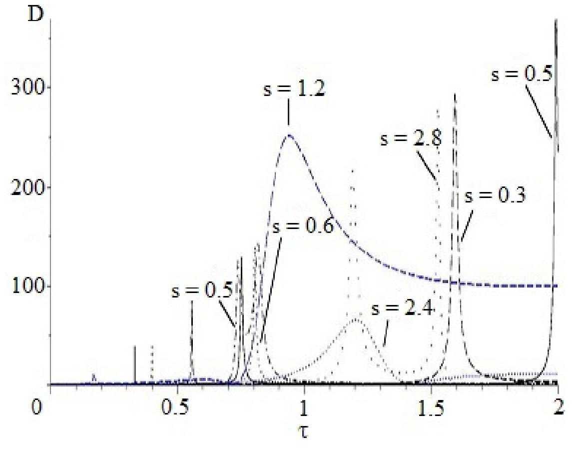

Fig. 7. *Foundation amplitude $D = D(\tau,s)$ at γ = 2.6, taking into account damping*

interval $0.3<s<0.9$ the rotor and foundation amplitudes monotonically increase. In this case, the eigenfrequency belongs to the range $0.25<\tau<0.85$. When s varies from 0.9 to 1.1, the rotor and foundation amplitudes decay quite rapidly, approaching zero values. For the studied fluid volume, third instability zone does not appear over the interval $0.3<s<1$. When the angular speed s increases from 0.5 to 0.85, the first two zones displace towards greater eigenfrequencies, namely $0.41<\tau<0.85$. Over the interval $0.9<s<1.2$ and in the vicinity of $\tau=0.85$ there is only one instability zone with small self-oscillation amplitudes.

Further increase in the angular speed ($s>1.2$) results in three instability zones, see Figs. 6 and 7. In these figures rotor and foundation amplitudes are small; in doing so, they first grow slowly and then slowly decay beginning from the value $s=2.8$. In this case, the eigenfrequencies associated with unstable regimes increase in s.

The third instability zone gradually disappears as the fluid volume in the cavity increases. For example, at $\gamma=4.56$ ($r_0=0.8R$), see Figs. 4 and 5, the third zone appears at $s>1$. Large rotor B and foundation D amplitudes occur over the interval $0.3<s<1$. In this case, the first instability zone belongs to the intervals $0.3<s<1$ and $0.45<\tau<0.85$, while the second one is over the interval $0.3<s<0.6$. The eigenfrequencies beginning with $\tau=1.4$ gradually decay approaching the value $\tau=0.6$. Next, over the interval $0.6<s<1$, the eigenfrequencies slowly increase. At $s>1.2$ three instability zones occur. However, the related rotor and foundation amplitudes are rather small.

In the case of a further increase of the fluid volume in the cavity, only two instability zones remain. In particular, if a third or half of the cavity is fluid filled, i.e. $\gamma=2.6$ ($r_0=2R/3$) in Figs. 6 and 7, or $\gamma=2.67$ ($r_0=0.5R$) in Figs. 8 and 9, respectively, the system performs large amplitude self-oscillation.

At $\gamma=2.6$ ($r_0=2R/3$) the self-oscillation amplitudes over the interval $0.3<s<0.5$ grow in s, see Figs. 6 and 7. The eigenfrequencies associated with unstable self-oscillation of the rotor and foundation also increase. Over the interval $0.5<s<0.6$ the values of τ rapidly decay, whereas over the interval $0.6<s<1$ they increase again along with self-oscillation amplitudes; in doing so, the latter are rather significant.

Over the interval $1<s<1.2$ the self-oscillation amplitudes and eigenfrequencies (or critical frequencies) τ corresponding to rotor and foundation instability zones experience a sharp decay. Over the interval $1.2<s<2.5$ the rotor and foundation perform small amplitude self-oscillation, and critical frequencies slowly grow. At $s>2.5$ the amplitudes sharply increase and the eigenfrequencies also rapidly grow.

The graphs of the rotor and foundation amplitudes B and D versus the dimensionless eigenfrequency τ are presented in Figs. 8 and 9 for several values of the rotor angular speed s. The effect of external damping is incorporated for a half-filled cavity, i.e. at $\gamma=1.67$. Inspection of the graphs shows that the maximal (minimal) values of the amplitudes B and D displace to larger (smaller) τ as s varies from zero to one. In this

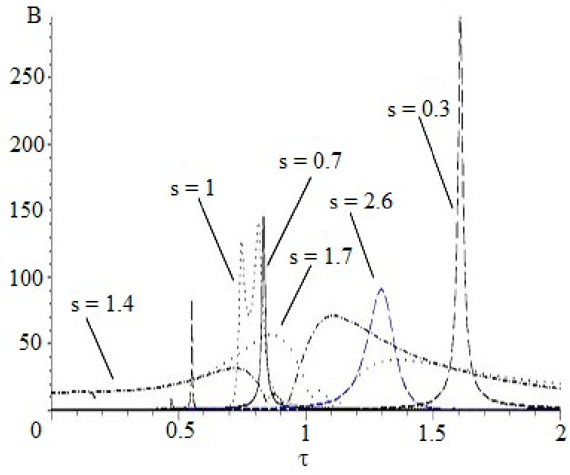

Fig. 8. *Rotor amplitude $B=B(\tau,s)$ at $\gamma=1.67$, taking into account damping*

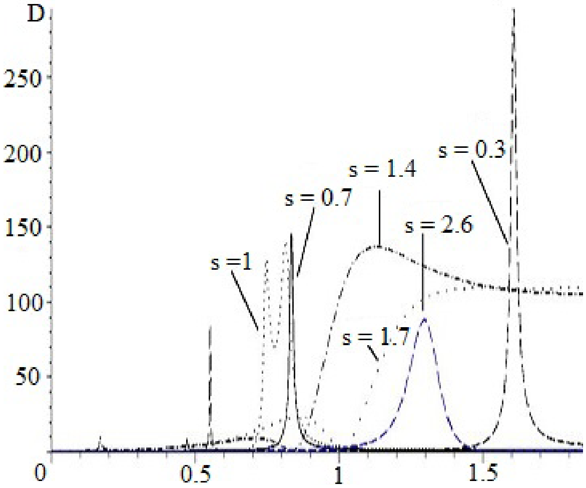

Fig. 9. *Foundation amplitude $D=D(\tau,s)$ at $\gamma=1.67$, taking into account damping*

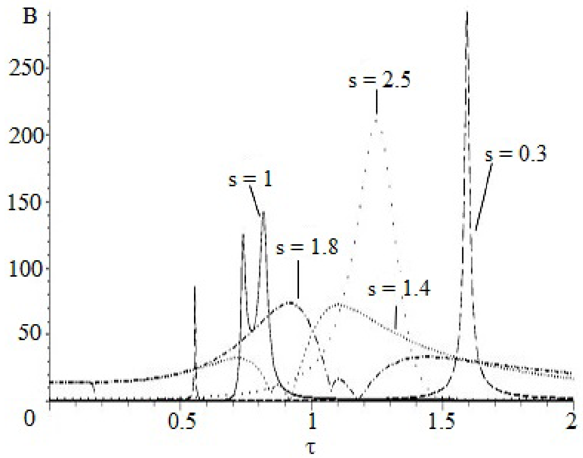

Fig. 10. *Rotor amplitude $B = B(\tau,s)$ at γ = 1.03, taking into account damping*

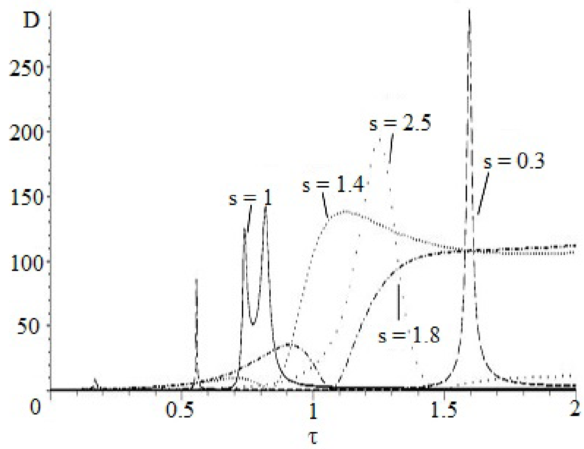

Fig. 11. *Foundation amplitude $D = D(\tau,s)$ at γ = 1.03, taking into account damping*

case the minima and maxima of B and D lie over the intervals $0.65<\tau<0.85$ and $0.85<\tau<1.8$, respectively.

Over the range $0.6<s<0.85$, the maxima and minima of B and D belong the interval $0.65<\tau<0.85$. Next, when s varies from 1 to 1.4, the B and D peaks as well as the frequencies τ decrease. For $s=1.7$ a B maximum is observed at $\tau=0.95$ and its minimum takes place at $\tau=1.2$. In this case, the D peaks have opposite locations. At larger angular speeds, when $s>1.7$, the B and D maxima and minima grow along with the eigenfrequencies τ. For more than a half fluid filled cavity amplitudes and frequencies behave similarly to the consideration above, see Figs. 6 to 9. In the latter case, self-oscillation amplitudes are lower than before. The second instability zone disappears at large fluid volumes in the cavity. At a very large relative volume corresponding to the value $\gamma=1.03$ ($r_0=1R/8$) rotor and foundation self-oscillation amplitudes related to the first instability, zone do not vary over a wide range of rotor angular speeds ($0.3<s<1$ and $s>1.8$), see Figs. 10 and 11. In this case, the eigenfrequency is $\tau=0.85$. The second instability zone arises over the intervals $0.3<s<0.5$ and $1.4<s<1.8$. It is characterized by small rotor and foundation self-oscillation amplitudes. Thus, self-oscillation amplitudes are not that significant for small fluid volumes in the cavity.

As the fluid volume approaches a third or half of the cavity, self-oscillation amplitudes take relatively large values, both for small and large angular speeds.

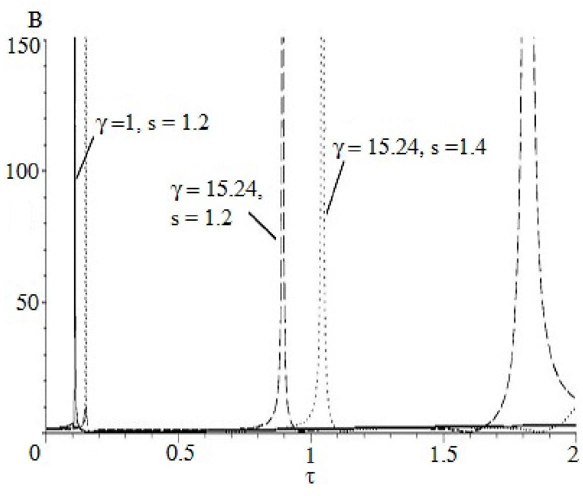

Fig. 12. *Rotor skeleton curves versus s and γ*

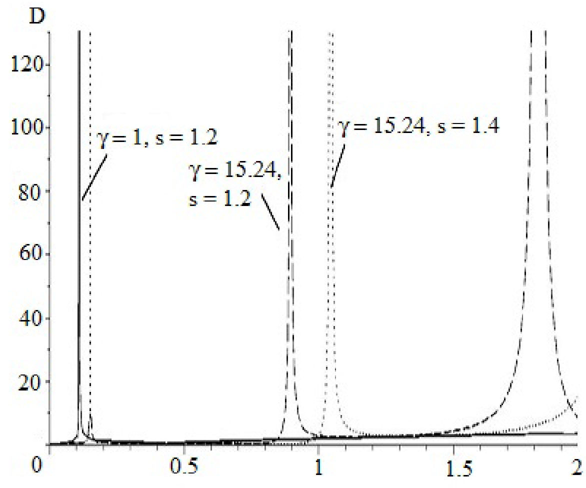

Fig. 13. *Foundation skeleton curves for several values of s and γ*

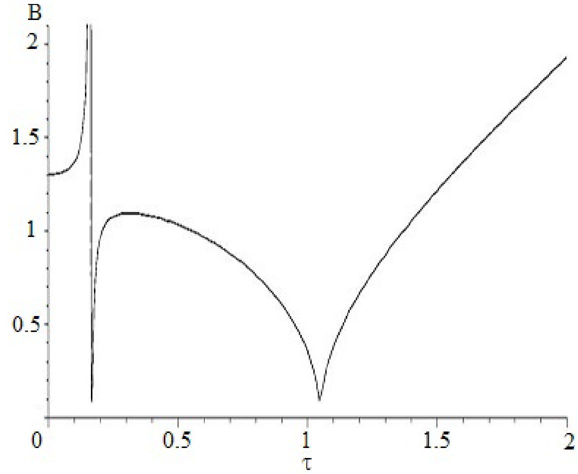

Fig. 14. *Rotor skeleton curve neglecting effect of fluid*

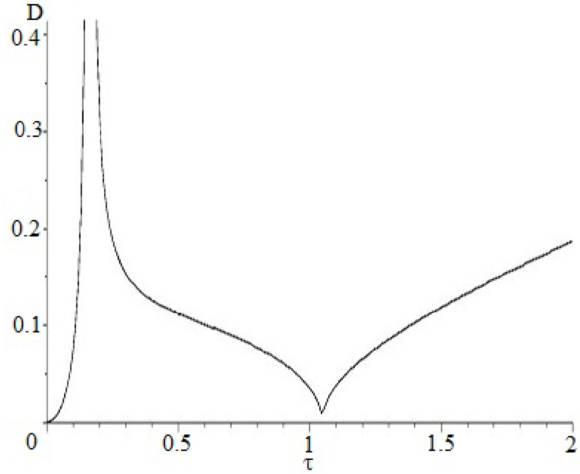

Fig. 15. *Foundation skeleton curve neglecting effect of fluid*

For a rotor cavity containing significant fluid volumes, there is a single instability zone characterized by the constant amplitude and eigenfrequency. The skeleton curves B and D of the rotor and foundation are shown in Figs. 12 and 13, taking into consideration the presence of fluid in the cavity. These figures display three critical values of τ corresponding to vertical asymptotes of skeleton curves. In the general case, they exist at any value of s over the whole range of the eigenfrequencies τ. The rotor and foundation amplitudes tend to infinity at the critical values, i.e. $B\to\infty$, $D\to\infty$. It is clearly seen that the first critical frequency lies in the vicinity of $\tau=0.11$. It virtually does not depend on the variation of the angular speed s and is very weakly dependent of the relative fluid volume γ. This frequency is slightly displaced towards greater values of τ as the relative fluid volume grows, i.e. $\gamma\to 1$. In this case, $\tau\leq 0.14$. The second critical frequency grows in s for any fluid volume.

At the same time its increase ($\gamma\to 1$) leads to a decrease of the second critical frequency. The third critical frequency mainly arises at low rotor angular speeds and quite small fluid volumes as well as at high angular speeds and large fluid volumes. The third critical frequency disappears when the fluid volume decreases, i.e. at $\gamma>1.03$ and $s>1$ or at $\gamma<15.24$ and $s<1.4$.

The increase of the rotor and foundation amplitudes B and D at a slow variation of the eigenfrequency τ below critical frequencies is very specific for all skeleton curves. After the passages through critical frequencies rotor and foundation amplitudes sharply decay over a narrow range of τ. Further increase in τ results in the growth of the amplitudes B and D. For the rotor and foundation skeleton curves incorporating the effect of fluid, we obtain $\omega=\sqrt{\dfrac{2c_2}{M(1+\mu D_6)}}$ with the vertical asymptote $\tau=n_{02}\sqrt{\dfrac{1}{1+\mu D_6}}$.

The occurrence of two (or three in the general case) peaks of rotor and foundation amplitudes (damping is incorporated) and of skeleton curves (damping is ignored) at any value of the parameters s and γ is caused by fluid vibrations along a free surface inside the rotor cavity. The graphs in Figs. 14 and 15, displaying rotor and foundation skeleton curves, illustrate the last observation.

For synchronous precession, i.e. at $\tau=s$, the rotor and foundation amplitudes do not depend on the fluid volume. In this case, they follow from Eqs. (30) and (31) with $D_6=1+\mu_L$.

5 SPECIAL CASES

The analytical solution obtained in the paper enables an immediate qualitative insight into practically important special setups. Below we study the limiting case of an empty rotor and also address the widely disputed phenomenon of self-centring. Consider first an empty rotor. In this case, the fluid force is zero, i.e. $F_r=0$. Free vibrations are specified by the coordinates:

$$x=a\cos\omega t \quad \text{and} \quad x_1=b\cos\omega t, \tag{32}$$

where a, b are amplitudes and ω is eigenfrequency.

Using the previous notations in the absence of imbalance in Eq. (25) and taking into account Eq. (32), we find rotor and foundation amplitudes, respectively:

$$a^2 = \frac{4\left[\omega^2\left(n_2^2-\omega^2\right)-n_0^2\left(n_2^2-(1+\mu)\omega^2\right)\right]\left(n_2^2-\omega^2\right)^2}{3n_1\left(n_2^2-(1+\mu)\omega^2\right)^3}, \quad (33)$$

$$b^2 = \frac{4\omega^4\mu^2\left[\omega^2\left(n_2^2-\omega^2\right)-n_0^2\left(n_2^2-(1+\mu)\omega^2\right)\right]}{3n_1\left(n_2^2-(1+\mu)\omega^2\right)^3}, \quad (34)$$

From the Eqs. (33) and (34) we can determine the dependence of the amplitudes on the frequency ω. The graphs of a and b versus ω are key curves characterizing the system. From the last formulae, it is clear that for $\omega \to \sqrt{2c_2/(m+M)}$ the amplitudes of a and b tend to infinity, i.e. a resonance occurs. The rotor amplitude a is equal to zero when the frequency ω is equal to $\omega=\sqrt{2c_2/M}$. In this case, the squared foundation amplitude becomes $b^2=-4n_0{}^2/(3n_1)$.

It is clear from the graphs in Figs 14 and 15 that rotor and foundation amplitudes grow over the interval $0<\tau<0.18$ approaching the vertical asymptote $\tau=0.18$ associated with the critical value of the eigenfrequency. Next, over the interval $0.18<\tau<0.25$ the rotor amplitude starts growing as τ increases. Then it slowly decays, approaching zero at $\tau=1.15$. At larger values of τ the amplitude increases along a parabola branch. The foundation skeleton curve has a similar shape. However, it also demonstrates a few peculiarities. In particular, it begins at the origin and grows approaching the asymptote $\tau=0.18$. At larger τ it slowly decays approaching zero at $\tau=1.15$. Finally, it grows along a parabola branch.

Forced vibrations are caused by an imbalance of the system. For the sake of simplicity, we insert a phase angle ε into the expression for the force $me\Omega_0^2\cos(\Omega_0 t+\varepsilon)$. The nonlinear forced vibrations of an empty rotor are governed by:

$$\begin{aligned} &\ddot{x}+n_0^2\left(x-x_1\right)+n_1\left(x-x_1\right)^3+2k\dot{x}= \\ &\quad =e\Omega_0^2\cos\left(\Omega_0 t+\varepsilon\right), \\ &\ddot{x}_1+n_2^2x_1-n_{01}^2\left(x-x_1\right)-n_{10}\left(x-x_1\right)^3=0. \end{aligned} \quad (35)$$

On substituting the formulae:

$$x=a_1\cos\Omega_0 t \quad \text{and} \quad x_1=b_1\cos\Omega_0 t. \quad (36)$$

Into Eq. (35) we finally get:

$$\begin{aligned} &\left(b_1\right)_{1,2}=\frac{\pm\Omega_0\sqrt{\mu^2e^2\Omega_0^2-4k_1^2a_1^2}+\mu\Omega_0^2a_1}{n_2^2-\Omega_0^2}, \\ &tg\varepsilon=\frac{2ka_1\Omega_0}{\left(n_0^2-\Omega_0^2\right)a_1-n_0^2b_1+\frac{3}{4}n_1\left(a_1-b_1\right)^3}, \end{aligned} \quad (37)$$

$$\frac{\left(n_2^2-n_{01}^2-\Omega_0^2\right)\left(\pm\Omega_0\sqrt{\mu^2e^2\Omega_0^2-4k_1^2a_1^2}+\mu\Omega_0^2a_1\right)}{n_2^2-\Omega_0^2}- \\ -n_{01}^2a_1-\frac{3}{4}n_{10}\left(a_1-\frac{\pm\Omega_0\sqrt{\mu^2e^2\Omega_0^2-4k_1^2a_1^2}+\mu\Omega_0^2a_1}{n_2^2-\Omega_0^2}\right)^3=0. \quad (38)$$

The Eq. (38) determines an amplitude-frequency characteristic of the rotor motion along Ox axis; a similar formula holds for Oy axis. This equation can be transformed to a sixth order polynomial in a_1. We also remark that for $n_{10}>0$ the system is rigid, whereas for $n_{10}<0$ it is elastic.

The studied nonlinear system supports multiple periodic regimes for the angular speed Ω_0 varying within certain limits. In this case, the vertical lines $\Omega_0=n_2$ are the asymptotes of the amplitude-frequency characteristic. On introducing the value of the rotor amplitude a_1 into Eq. (37), we may derive a formula for $b_1(\Omega_0)$ expressing the amplitude-frequency characteristic of the foundation.

Next, the issue related to self-centering and pressure on support will be discussed. The formulae in Eqs. (37) and (38) enable to find limiting values of the amplitudes a_1 and b_1, i.e. $\lim_{\Omega_0\to\infty} a_1=\mp e$, and $\lim_{\Omega_0\to\infty} b_1=-\left(a_1\pm e\right)\mu=0$. In particular, for regular precession we get $\lim_{\Omega_0\to\infty} a_1=-e$, $\lim_{\Omega_0\to\infty} b_1=0$. Hence, at an infinite increase of the angular speed the vector associated with static imbalance is directed towards the origin and tends to displace the rotation axis towards the vertical axis Oz. In the latter case, a static imbalance of the rotor has no effect. The observed self-centering of a rigid rotor on rolling bearings in the presence of an elastic foundation is an important feature of the system.

The pressure along the contact zone of the rotor and foundation can be evaluated by calculating the reaction forces at bearing supports. Let us replace the action of the rotor by its reaction forces. As each bearing support is subject to the same reaction force, the rotor performs the plane-parallel motion. The equation of foundation motion is then given by $M\ddot{x}_1+2c_2x_1=2R_{1x}$, resulting in $R_{1x}=b_1\left(c_2-M\Omega_0^2/2\right)$, which means that at $M=2c_2/\Omega_0^2$ the radial pressure along the contact of the rotor and foundation is zero.

Therefore, for a constant operating speed, we may define a stiffness coefficient of the elastic foundation for which the aforementioned pressure is zero. The foundation reaction force acting on the supports is $R_2=c_2 b_1$, where b_1 is the foundation amplitude. It tends to zero at an infinite increase in the angular speed Ω_0, i.e. in the case of self-centering.

6 CONCLUDING REMARKS

A generalized dynamic model of a rotor-fluid-foundation system taking into account the nonlinear stiffness of rolling bearings along with fluid and foundation vibrations is developed and investigated.

The obtained results enable optimising the parameters of the rotor, foundation, and fluid and are of interest for reducing stresses along the contact surfaces, forced vibrations amplitudes as well as the width of instability zones. There is also room for adapting the conditions supporting self-centering of the system.

Suppression of harmful rotor vibrations by choosing appropriate system parameters, including foundation deformability, is economically efficient and has the potential to be implemented in technology. In this case, an elastic foundation plays a role of a sort of counterbalance.

7 REFERENCES

[1] Tondl, A. (1965). *Some Problems of Rotor Dynamics*. Chapman and Hall, London.

[2] Penny, J., Friswell, M., Garvey, S., Lees, A. (2010). *Dynamics of Rotating Machines*. Cambridge University Press, Cambridge.

[3] Vance, J.M., Zeidan, F.Y., Murphy, B. (2010). *Machinery Vibration and Rotor Dynamics*. Wiley, Hoboken, **DOI:10.1002/9780470903704**.

[4] Bolotin, V.V. (1963). *Nonconservative Problems of the Theory of Elastic Stability*. Macmillan, New York.

[5] Derendyayev, N.V., Soldatov, I.N., Vostrukhov, A.V. (2006). Stability and Andronov-Hopf bifurcation of steady-state motion of rotor system partly filled with liquid: Continuous and discrete models. *Journal of Applied Mechanics*, vol. 73, no. 4, p. 580-589, **DOI:10.1115/1.2164514**.

[6] Rahimov, E.R., Rahmatullaev, A.Sh., Kydyrbekuly, A.B. (1987). Dynamics of unbalanced rotor in the interaction with the other physical fields. *Transactions of the 7th World Congress on the Theory of Machines and Mechanisms*, Sevilla, p. 532-539.

[7] Manasseh, R. (1994). Distortions of inertia waves in a rotating fluid cylinder forced near its fundamental mode resonance. *Journal of Fluid Mechanics*, vol. 265, p. 345-370, **DOI:10.1017/S0022112094000868**.

[8] Changsheng, Z. (2006). Experimental investigation into the effect of fluid viscosity on instability of an over-hung flexible rotor partially filled with fluid. *Journal of Vibrations and Acoustics*, vol. 128, no. 3, p. 392-401, **DOI:10.1115/1.2166857**.

[9] Lichtenberg, G. (1980). Experimentell Untersuchung des Schurngugsverhaltens eines flussig – keitsgefullten Rotors mit Kreiselwirkung. *VDI-Berichte*, no. 381, p. 161-166.

[10] Urbiola-Soto, L., Lopez-Parra, M. (2013) Liquid self-balancing device effects on flexible rotor stability. *Shock and Vibration*, vol. 20, no. 1, p. 109-121, **DOI:10.3233/SAV-2012-0731**.

[11] Changsheng, Z. (2001). Stability behaviour of an isotropic rotor system anisotropically mounted and partially filled with inviscous fluid. *Proceedings of IMAC-19, A Conference on Structural Dynamics*, p. 1278-1283.

[12] Kydyrbekuly, A.B. (2012). *Rotor-Liquid-Fundament System's Oscillation. Advances in Mechanisms Design*. Springer Science+Business Media, Dordrecht, p. 223-229, **DOI:10.1007/978-94-007-5125-5_30**.

[13] Silin, R., Royzman, V. (1999). The research into the automatic balancing process of rotors with vertical axis of rotation. *10th World Congress on the Theory of Machine and Mechanisms*, Oulu, vol. 4. p. 1734-1739.

[14] Childs, D. (1993). *Turbomachinery rotor dynamics phenomena. Modeling and Analysis*, Wiley-Interscience, New York.

[15] Zebin, Y., Dawei, D., Haiyu, G., Xiaodong, S., Rong, F., Huangqiu, Z. (2015). Rotor mass eccentricity vibration compensation control in bearingless induction motor. *Advances in Mechanical Engineering*. Article ID 168428, **DOI:10.1155/2014/168428**.

[16] Savin, L., Solomin, O., Ustinov, D. (1999). Rotor dynamics on friction bearings with cryogenic lubrication. *10th World Congress on the Theory of Machine and Mechanisms*, Oulu, vol. 4, p. 1716-1721.

[17] Harsha, S.P. (2005). Non-linear dynamic response of a balanced rotor supported on rolling element bearings. *Mechanical Systems and Signal Processing*, vol. 19, no. 3, p. 551-578, **DOI:10.1016/j.ymssp.2004.04.002**.

[18] Isayuk-Sayevskaya, A.R., Kelzon, A.S. (1995). Dynamics of a high-revolution scroll centrifuge. *Machine Vibration*, vol. 3, no. 4, p. 233-237.

[19] Krämer, E. (1993). *Dynamics of Rotors and Foundations.* Springer-Verlag, New York, **DOI:10.1007/978-3-662-02798-1**.

[20] Feng, N., Hahn, E. (1997). Vibration analysis of rotor-bearing-pedestal system. *Proceedings of the 5th International Congress on Sound and Vibration*, Adelaide, p. 2457-2464.

[21] Feng, N., Hahn E. (1998). Experimental identification of the pedestal in a rotor-bearing-pedestal system. *Proceedings of the 5th IFToMM International Conference on Rotor Dynamics*, p. 734-745.

[22] Sun, L. (1995). *Active Vibration Control of Rotor-Bearing System*. PhD Thesis, University of Melbourn, Melbourn.

[23] Bai, C., Zhang, H., Xu, Q. (2010). Experimental and numerical studies on nonlinear dynamic behavior of rotor system supported by ball bearings. *Journal of Engineering for Gas Turbine and Power*, vol. 132, no. 8, paper 082502, **DOI:10.1115/1.4000586**.

[24] Aktürk, N., Uneeb, M., Gohar, R. (1997). The effects of number of balls and preload on vibrations associated with

ball bearings. *Journal of Tribology*, vol. 119, no. 4, p. 747-753, **DOI:10.1115/1.2833880**.

[25] Guida, D., Pappalardo, C.M. (2009). Sommerfeld and mass parameter identification of lubricated journal bearings. *Applied and Theoretical Mechanics*, vol. 4, no. 4, p. 205-214.

[26] Tiwari, M., Gupta, K., Prakash, O. (2000). Effect of radial internal clearance of a ball bearing on the dynamics of a balanced horizontal rotor. *Journal of Sound and Vibration*, vol. 238, no. 5, p. 723-756, **DOI:10.1006/jsvi.1999.3109**.

[27] Tiwari, M., Gupta, K., Prakash, O. (2000) Dynamic response of an unbalanced rotor supported on ball bearings. *Journal of Sound and Vibration*, vol. 238, no. 5, p. 757-779, **DOI:10.1006/jsvi.1999.3109**.

[28] Harsha, S.P. (2006). Rolling bearing vibrations – the effects of surface waviness and radial internal clearance. *International Journal for Computational Methods in Engineering Science and Mechanics*, vol. 7, no. 2, p. 91-111, **DOI:10.1080/155022891010015**.

[29] Harsha, S.P. (2006). Nonlinear dynamic analysis of a high-speed rotor supported by rolling element bearings. *Journal of Sound and Vibration*, vol. 290, no. 1-2, p. 65-100, **DOI:10.1016/j.jsv.2005.03.008**.

[30] Jang, G.H., Jeong, S.W. (2003). Analysis of a ball bearing with waviness considering the centrifugal force and gyroscopic moment of the ball. *Journal of Tribology*, vol. 125, no. 3, p. 487-498, **DOI:10.1115/1.1538618**.

Strojniški vestnik - Journal of Mechanical Engineering 62(2016)6, 363-372

DOI:10.5545/sv-jme.2015.3194
Original Scientific Paper
Received for review: 2015-11-12
Received revised form: 2016-03-17
Accepted for publication: 2016-03-30

Direct Diode Laser Cladding of Inconel 625/WC Composite Coatings

Damian Janicki* – Małgorzata Musztyfaga-Staszuk
Silesian University of Technology, Faculty of Mechanical Engineering, Poland

Metal matrix composite coatings, composed of Inconel 625 alloy and tungsten carbide (WC), have been produced by laser cladding using a high power direct diode laser with a rectangular laser beam spot and a top-hat beam profile. The primary goal of the investigation was to understand the role of the shape of WC particles and the heat input level on the quality of the composite coating system used, especially on its erosion behaviour. The results indicated that angular WC particles are more susceptible to dissolution in the molten pool than spherical. However, the composite coatings containing angular WC particles exhibited significantly higher erosion resistance than those with spherical WC for both normal and oblique impacts. This is directly attributed to the excellent mechanical interlocking of the angular WC in the matrix. The WC/matrix interfacial decohesion has been observed in the coatings containing spherical WC at the oblique impact.

Keywords: metal matrix composite coating, Inconel 625, erosive wear, laser cladding, diode laser, tungsten carbide

Highlights

- *A diode laser with a rectangular beam spot and the uniform distribution of laser power (top-hat beam) was used to fabricate Inconel 625-based composite coatings (CCs) with angular and spherical WC particles.*
- *The degree of WC dissolution depends on the heat input level but also on the shape of WC particles.*
- *The shape of WC particles plays a crucial role in the erosion resistance of the CCs.*
- *The irregularly shaped (angular) WC particles, because of better mechanical interlocking with the matrix, provides higher erosion resistance of CCs for both normal and oblique impact.*
- *The spherical WC particles are prone to the WC/matrix interfacial decohesion at oblique impact.*

0 INTRODUCTION

In the previous decade, significant advances have been made in the fabrication of metal matrix composite coatings (MMCCs) via a laser-cladding process [1]. This process markedly reduces the high degree of dissolution of reinforcing particles (RP) that occurs during the plasma transferred arc (PTA) process [2]. Because of the precise control of the heat input and the rapid solidification associated with the laser-cladding process, the resulting MMCCs have a homogeneous distribution of the RPs and a very low degree of the RPs dissolution in the alloy matrix [3]. The high power direct diode laser (HPDDL) with uniform intensity distribution over rectangular beam spot (called a top-hat beam) is especially well suited for the fabrication of MMCCs via both *ex-situ* [4] and *in-situ* methods [5].

Alloy 625 (Inconel 625) is a nickel-based alloy that was originally developed for high-temperature turbine applications. However, because of its combination of good oxidation, corrosion resistance and moderate mechanical strength, Alloy 625 is utilized extensively as a coating material for marine environments and also for the hard-facing of tool and die steels [6]. Several studies have shown that this alloy is also a promising candidate for the alloy matrix in the MMCCs [7]. These MMCCs are a potential approach to achieve protective coatings for industrial applications requiring high resistance to both corrosion and erosion. It is well known that the MMCCs containing tungsten carbide (WC) are particularly suitable for erosive environments, due to excellent wear characteristic of this coating system [8]. In the case of the above-mentioned composite coating system, several important issues must be considered. Due to a low heat of formation, WC is prone to dissolution in the molten pool during the cladding process [9]. The dissolution of WC in the matrix alloy gives rise to the formation of secondary phases, which in turn leads to both the deterioration of wear properties of the coatings and increased sensitivity to cracking [10]. Scant data is available on the effect of WC particles shape on the nickel-based MMCCs' performance. However, the shape of WC particles in those coatings can influence their microstructure and especially erosion resistance that this study attempts to explore.

In this study, the MMCCs, composed of Inconel 625 alloy and tungsten carbide (spherical and angular in shape), have been produced by laser cladding using an HPDD laser with a rectangular laser beam spot and the uniform distribution of laser power (top-hat beam). The coatings were characterized in terms

*Corr. Author's Address: Silesian University of Technology, Faculty of Mechanical Engineering, Konarskiego 18A, Gliwice, Poland, damian.janicki@polsl.pl

of their structure, microhardness and erosive wear behaviour.

1 EXPERIMENTAL PROCEDURE

1.1 Materials

A commercially available Inconel 625 powder with a particle size range of 40 µm to 100 µm was chosen as the alloy matrix of the composite coatings. The chemical composition of this alloy is shown in Table 1. To study the effect of reinforcing particles' (RPs) morphology on the microstructure of the composite coatings and their erosion behaviour, angular and spherical cast tungsten carbide powders (WC/W_2C) were used. In both cases, the WC/W_2C particles size were in a range of 100 µm to 200 µm and their volume fraction in the cladding powders was 60 %. The size range of WC/W_2C particles was selected based on previous works [3]. In order to investigate the effect of the RPs addition to the cladding powder on the geometry of the single-pass clad and the microstructure of the alloy matrix, the pure Inconel 625 powder (without RPs) was also used as the coating material. A stainless steel AISI 304 plate of 10 mm in thickness was used as the substrate material. The chemical composition of the substrate material is also presented in Table 1. The SM was brushed with a stainless steel wire brush and cleaned with acetone prior to the cladding process.

1.2 Laser Processing

The laser-cladding process was carried out using an HPDD laser Rofin DL020 with a maximum output power of 2.0 kW. The rectangular beam of 1.8 mm × 6.8 mm at the focal plane was focused on the top surface of the substrate. The short axis of the beam was set parallel to the traverse direction. The cladding powder was injected into the molten pool using an off-axis flat powder injection nozzle. The molten pool was protected by a shielding gas: argon at a flow rate of 10 l/min. The cylindrical shielding gas nozzle with a diameter of 20 mm was set coaxially with the powder feeding nozzle.

To study the influence of the heat input level on the single-pass clad geometry, microstructure, and hardness, the experiments were conducted at four laser power levels, ranging from 800 W to 1400 W, while traverse speed and powder feed rate were held constant at 0.2 m/min and 0.8 cm³/min, respectively. The coatings were produced by the multi-pass overlapping cladding with an overlap ratio of 30 %. All cladding trials were performed without preheating the substrate.

2 RESULTS

2.1 Macro and Microstructure Analysis

The cross-sectional macrographs of single-pass clads with the angular and spherical WC particles produced at a laser power of 1000 W (heat input of 300 J/mm) are presented in Fig. 1. The laser-cladding conditions and geometrical parameters of the resulting single-pass clads are summarized in Table 2. The dilution rate of the clad was estimated using the Eq. (1):

$$U[\%] = \frac{F_{BM}}{F_{BM} + RA} \cdot 100, \qquad (1)$$

where F_{BM} is the melted cross-sectional area of the substrate and RA is the cross-sectional area of the reinforcement of the clad. The above-mentioned geometrical parameters were measured on cross-sectional macrographs of single-pass clads using an optical microscope and image analyser software.

The cross-sectional SEM microstructure of the metallic Inconel 625 coating produced at the heat input (HI) of 420 J/mm is presented in Fig. 2. Typical SEM images of the microstructure of composite coatings with the spherical and angular WC particles, produced at different heat input levels are shown in Figs. 3 and 4, respectively. For convenience, the composite coatings with angular and spherical WC particles have been labelled CCAs and CCSs, respectively. A summary of measurements of WC volume fractions and the matrix mean free path between the WC particles in the composite coatings is given in Table 2. The WC volume fraction and the matrix mean free path were measured using a Nikon NIS-Elements quantitative image analysis system. The measurements were conducted on cross-sections from the under surface and middle areas of the coatings, over a total area of 10 mm² for each coating.

Table 1. *Chemical compositions of the alloy matrix powder (Inconel 625) and substrate used (% weight)*

Materials	C	Cr	Mo	Fe	Mn	Nb	Al	Si	Ti	Ni
Inconel 625 powder	0.02	19.6	5.8	1.6	-	3.9	0.1	0.4	0.15	Balance
AISI 304 plate	0.08	18.9	-	Balance	2.0	-	-	1.0	-	10.0

Table 2. *Parameters of HPDDL cladding process and measured geometrical parameters of the single-pass clads and microstructural parameters of the composite coatings*

Clad/coating no.	WC shape	Laser power [W]	Heat input* [J/mm]	Dilution [%]	*RA*** [mm²]	Matrix mean free path [μm]	Volume fraction of WC [%]
A1	angular	800	240	28	2.3	46±25	54
A2		1000	300	35	2.7	48±25	52
A3		1200	360	40	3.1	52±30	49
A4		1400	420	42	3.4	62±35	45
S1	spherical	800	240	31	2.1	37±15	58
S2		1000	300	34	2.7	39±15	56
S3		1200	360	37	3.0	45±20	54
S4		1400	420	41	3.3	49±25	50
M1***	-	800	240	6	3.0	-	-
M2		1000	300	7	3.8	-	-
M3		1200	360	14	4.5	-	-
M4		1400	420	18	4.6	-	-

Remarks: * defined as the laser power divided by the traverse speed, ** the cross-sectional area of reinforcement of the single-pass clad, *** metallic Inconel 625 clad

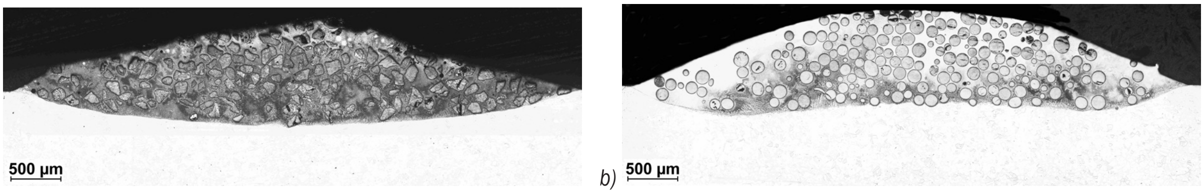

Fig. 1. *Macrographs of single-pass clads produced at the HI of 300 J/mm using powder with a) spherical WC (clad no. S2), and b) angular WC (clad no. A2)*

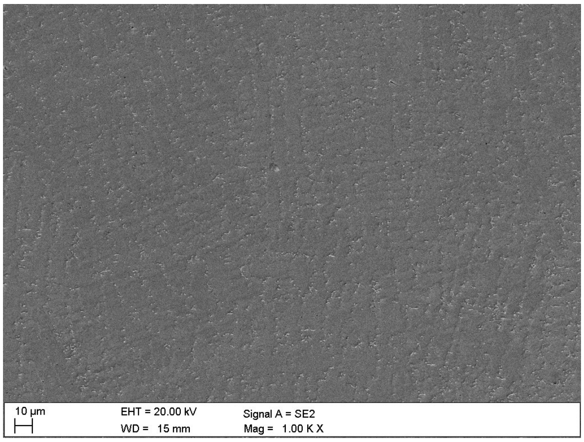

Fig. 2. *SEM micrograph taken from the mid-section of metallic Inconel 625 coating produced at the HI of 420 J/mm (coating no. M4)*

Typical dimensions of the composite single-pass clads are a width of approx. 5.5 mm and height in the range of 0.8 mm to 0.9 mm. The thickness of composite coatings fabricated by multi-pass overlapping with an overlap ratio of 30 % was about 1.5 mm, in the whole range of the heat input.

The X-ray diffraction patterns of the metallic Inconel 625 coating and composite coatings produced at the heat input of 300 J/mm are presented in Fig. 5. The X-ray diffraction measurements were performed using a PANalytical X'Pert PRO MPD X-ray diffractometer equipped with a Co-K_α (λ = 0.179 nm) source and an X'Celerator detector. The X-ray tube was operated at 40 kV and 30 mA. XRD analysis of the metallic Inconel 625 coating detected only the presence of the FCC γ-Ni phase. In turn, the composite coatings contain the FCC γ-Ni phase, WC, W_2C and also a relatively significant fraction of complex carbide Fe_3W_3C. Moreover, XRD analysis indicated that the fraction of Fe_3W_3C phase in the CCAs and CCSs is almost similar.

2.2 Hardness Testing

Microhardness testing was conducted using Wilson Wolpert 401 MVD Vickers hardness tester. To determine the hardness of the matrix and WC particles the load of 200 g for a dwell time of 10 s was used. The average hardness of the secondary phases was measured using 10 g load for a dwell time of 5 s. The

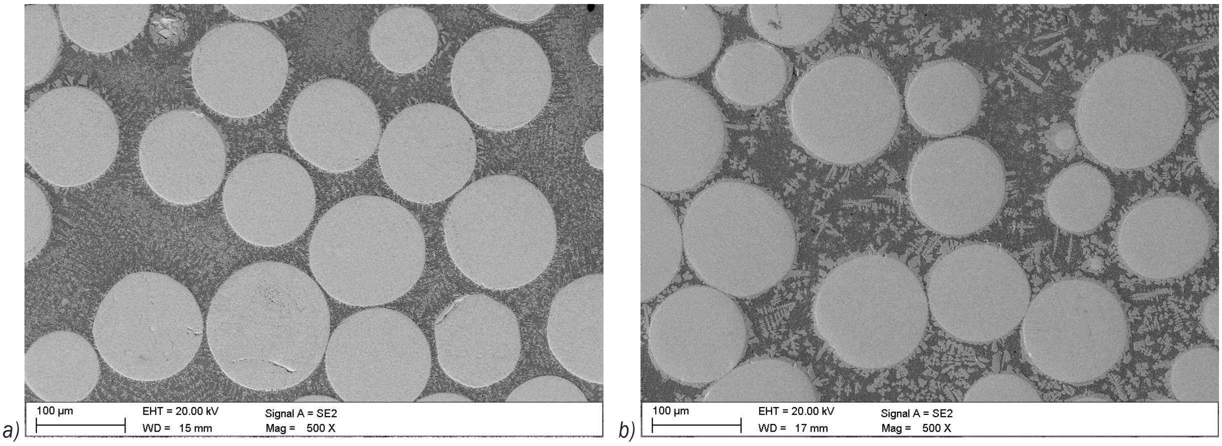

Fig. 3. *SEM micrographs taken from the mid-section of the CCSs produced at the HI of a) 240 J/mm (coating no. S1); b) 420 J/mm (coating no. S4)*

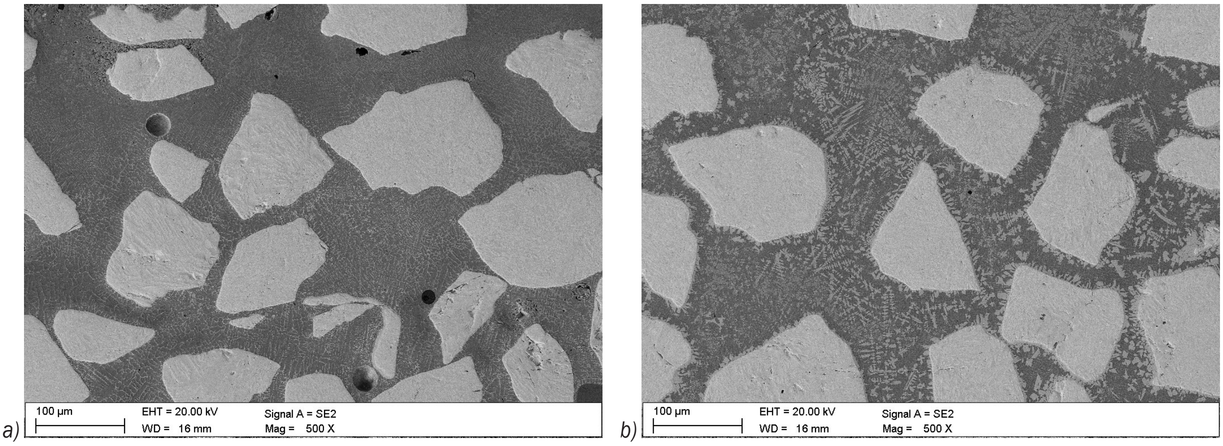

Fig. 4. *SEM micrographs taken from the mid-section of the CCAs produced at the HI of a) 240 J/mm (coating no. A1); b) 420 J/mm (coating no. A4)*

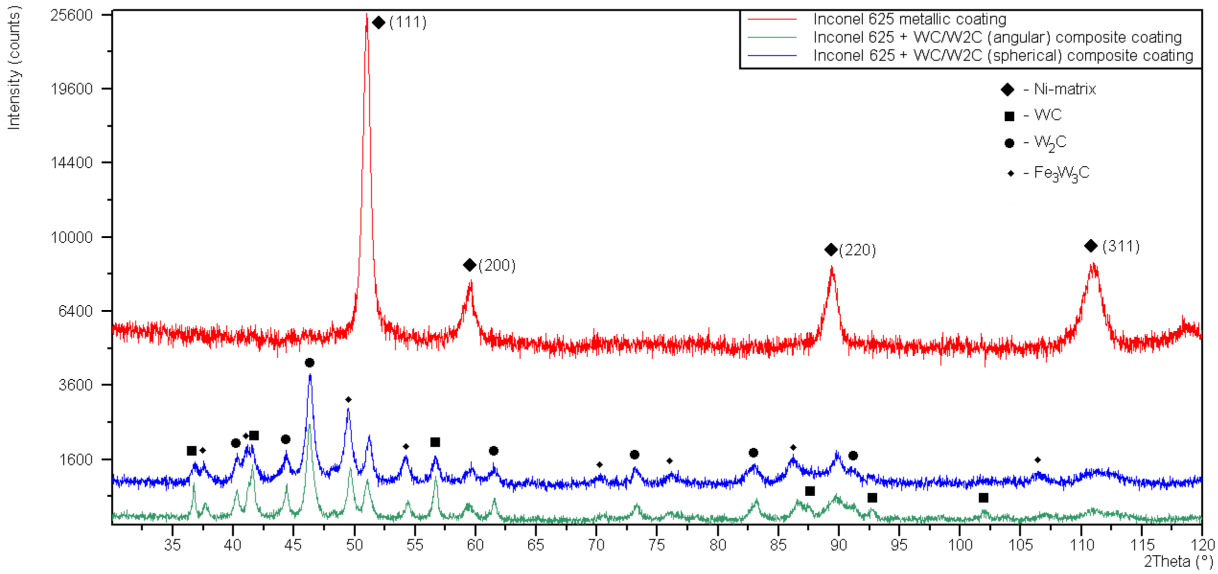

Fig. 5. *XRD patterns of the metallic and composite coatings produced at the heat input of 300 J/mm*

metallic Inconel 625 coatings exhibited a constant hardness of approx. 230 HV, in the whole range of HI. In the case of composite coatings, the average hardness of matrix increased from 300 HV at the lowest HI to 500 HV at the highest HI. The hardness of both types of WC particles was about 2100 HV. The average microhardness of the secondary dendritic and blocky Fe_3W_3C phases was found to be 1000 HV±100 HV.

2.3 Erosion Testing

Results of erosion tests of the metallic Inconel 625 coating (MC), CCAs and CCSs, produced at HI of 300 J/mm are given in Table 3.

Table 3. *Results of erosion tests of the MC and CCs*

Coating label	Impact angle [º]	Average erosion rate* [mg/min]	Average erosion value** [0.001 mm³/g]
MC	90	0.31	18.36
	30	0.60	35.54
CCA	90	0.61	24.80
	30	0.21	8.54
CCS	90	1.07	43,50
	30	0.34	13.82

Remarks: *calculated as the mass loss of the specimen divided by total test time; **calculated by dividing the erosion rate by the erodent flow rate and then dividing by the coating density.

The HI level used provided non-porous composite coatings (CCs) with low dissolution level of WC particles. The solid-particle erosion testing system used in this study was designed in accordance with standard ASTM G 76-95. Angular alumina powder (Al_2O_3) with an average particle size of 50 µm was used as erodent material. The erodent particles were accelerated in a stream of compressed air along a cylindrical tungsten carbide nozzle having an internal diameter of 1.5 mm and a length of 50 mm. The stand-off distance, from the end of the nozzle to the surface of the specimen, was 10 mm. All tests were performed at an erodent impingement velocity of 70 m/s ± 2 m/s. The feed rate of the erodent and the test period were 2.0 g/min ± 0.25 g/min and 10 min, respectively. The impingement angles selected were 30° and 90°. Prior to erosion testing, the surface of the coatings was ground to a smooth finish using a 400 grit diamond wheel. The weight loss of the erosion specimens was determined by weighting the specimens before and after the erosion tests to the nearest 0.01 mg. The specimens were ultrasonically cleaned in acetone before weighing. Following ASTM Standard G76 **[11]**, erosion values were calculated as the volume loss of erosion specimen per mass of erodent particles used over each test period. The wear surfaces were examined using scanning electron microscope (Figs. 10 and 11).

3 DISCUSSION

3.1 Macro and Microstructure Analysis

The dilution level of the composite single-pass clads was even 5 times higher than that of the metallic produced at the same HI levels (Table 2). This is associated with the higher absorption coefficient of tungsten carbide compared to the alloy matrix absorption coefficient. Furthermore, the dilution level is strongly affected by the laser power, which is connected to the intensity of the convection movement in the molten pool driven by surface tension. The higher laser power gives rise to more intensive fluid flow in the molten pool, and as a result higher dilution. In the investigated range of cladding parameters, the dilution level of the metallic and composite single-pass clads can be controlled from 6% to 18% and from 28 % to 42 %, respectively. Moreover, with increasing laser power level, the cross-sectional area of reinforcement of the single-pass clads increases, which in turn results from a higher powder capture efficiency occurring at the higher laser power, during the laser cladding with an off-axis powder injection system. Because of a short interaction time between the laser beam and the powder stream, during this cladding process, a melting of the powder particles occurs only when they enter the molten pool. In this case, the capture efficiency depends directly on the size of the molten pool. The higher laser power leads to the larger molten pool area and the larger amount of captured powder and, in consequence, the larger reinforcement area of the clad.

In comparing the reinforcement areas of the metallic and composite single-pass clads (Table 2), it can be seen that the capture efficiency of the metallic powder is approx. 25 % higher than that of the composite powder. It is consistent with the above-mentioned mechanism of powder capture. Generally, the WC particles undergo only partial melting in the molten pool; thus, their relatively high volume fraction in the cladding powder significantly limits the volume of the molten matrix alloy which is responsible for powder capturing. The shape of WC particles in the cladding powder has no significant effect on the geometry of single-pass clads and the powder capture efficiency (Fig. 1).

In general, the microstructure of the metallic Inconel 625 coatings consists of austenite grains and interdendritic areas enrich in Nb and Mo (Fig. 2). The morphology of austenite grains varies from the fusion boundary to the coating surface, due to changes in the local solidification conditions. The temperature gradient is the highest at the fusion boundary promoting columnar dendritic growth in a direction opposite to the direction of heat transfer. Towards the coating surface, the temperature gradient becomes lower, which (in combination with a higher solidification rate) results in significant undercooling leading to the formation of equiaxed dendrites. Based on energy-dispersive X-ray spectroscopy (EDS) analysis, the mean concentration of Fe in the metallic Inconel 625 coating produced at the highest HI (420 J/mm) was estimated to be 16.2 %. This value is in good agreement with the geometrical measurement of the dilution, listed in Table 2. The metallic coatings produced throughout the range of HI levels were free of porosity, microvoids, and microcracks.

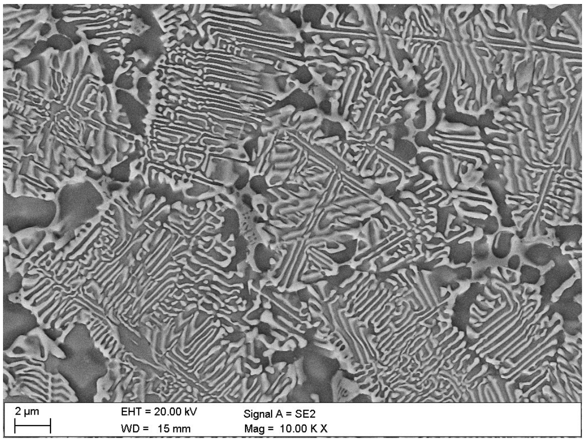

Fig. 6. *SEM micrograph showing the fishbone-like W-rich phases in the interdendritic areas in the composite coatings (coating no. A1)*

Both types of the RPs enable producing the composite coatings with a uniform distribution of the RPs throughout the alloy matrix (Figs. 3 and 4). Moreover, the top-hat beam profile of the HPDD laser prevents the RPs from dissolving in overlap zones between consecutive passes. A transition region (interphase) between the RP and the matrix is continuous and free of defects throughout the range of the HI. Both the CCAs and CCSs produced at the lowest HI (240 J/mm) exhibited a negligible dissolution of the RPs leading to the insignificant enrichment of the alloy matrix in the tungsten. In this case, the alloy matrix showed the dendritic growth of austenite grains and fishbone-like (herringbone-like) W-rich phases located in the interdendritic areas (Fig. 6). The dendrite cores were enriched in W and Fe up to 2 % and 36 %, respectively. The W and Fe content in the interdendritic areas was approx. 39 % and 28 %, respectively. The interdendritic areas also contain the Nb-rich eutectic-like structures, shown in Fig. 7. Furthermore, in comparison to the metallic coating produced at the same HI level, the austenite grain size was refined. EDS line-scan analysis collected in the transition region, presented in Fig. 8, revealed a relatively shape change in the concentration of W, Ni, Fe and Cr. This indicates the low decomposition of outer layers of the WC particles in the molten pool, at that HI level. Moreover, the minor porosity was observed in those composite coatings.

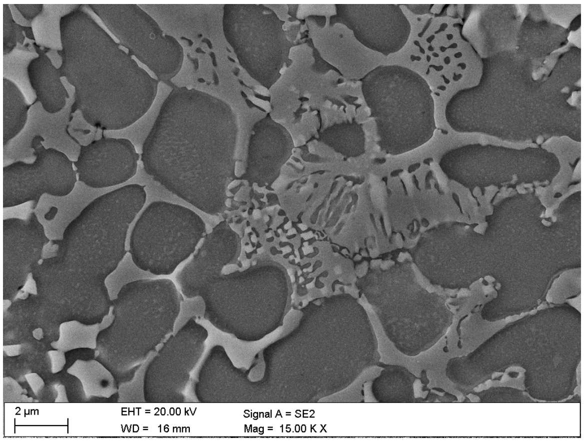

Fig. 7. *SEM micrograph showing the Nb-rich eutectic-like structures in the interdendritic areas in the composite coating (coating no. S1)*

Generally, the increase of the HI level gives rise to an increase of the RPs dissolution, which in turn leads to the formation of dendritic and blocky W-rich phases, as the results of the considerable enrichment of the alloy matrix in tungsten. Quantitative analysis of micrographs of the CCAs and CCSs produced at the HI of 240 J/mm indicates that the RPs occupy about 54 vol.% and 58 vol.%, respectively. In the case of the CCAs and CCSs produced at the HI of 420 J/mm, the volume fraction of the RPs was 45 % and 50 %, respectively. This implies that about 25 vol.% and 17 vol.% of the RPs have undergone dissolution in the above-mentioned composite coatings, respectively. Furthermore, it follows that the angular RPs are more susceptible to dissolution in the molten pool than spherical ones are. It can be attributed to the sharp ages of the angular RP that are easily melted in the molten pool, which is further confirmed by rounded RPs at the high HI levels (Fig. 4b). Moreover, the spherical

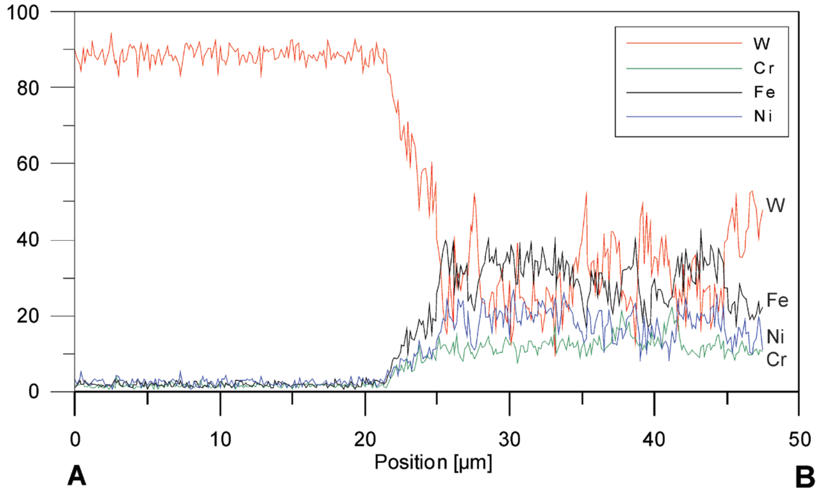

Fig. 8. *EDS line-scan analysis across the transition region in the CCS produced at the HI of 240 J/mm; profile taken along the line marked in Fig. 9a*

shape minimizes the contact area of molten metal and the RP, reducing, to the same extent, the amount of heat introduced to the RP in the molten pool.

Additionally, it is noteworthy that the morphology of the transition region between the RP and the matrix is affected by the HI level. At the lowest HI the transition region exhibits lamellar WC phases directly adjacent to the surface of RPs (Fig. 9a). The presence of these phases results from both a very slight decomposition of the outer layers of the RPs in the molten pool and the different thermodynamic stability of WC and W_2C carbides. The cast tungsten carbide used was a eutectic mixture of W_2C and WC. The W_2C carbide, due to the lower thermal stability at high temperature in comparison to the WC carbide, undergoes dissolution in the molten pool while the WC remains intact. The increase in the HI leads initially to the formation of thin layers of W_2C around the RPs. Further increase of the HI results in the formation of dendritic and blocky W-rich phases in the transition region (Fig. 9b). The presence of these phases provides a gradient distribution of all elements across the transition region but also leads to the widening of the transition region (up to 12 µm). In the case of the highest HI (420 J/mm), thus at the highest dissolution level of the RPs, the above-mentioned secondary W-rich phases are uniformly distributed throughout the spaces between RPs. The EDS spot analysis of those phases revealed a high W and Fe content, suggesting that they are complex carbides (M_6C) Fe_3W_3C. X-ray diffraction results confirmed the presence of Fe_3W_3C in both the CCA and CCS (Fig. 5). In addition, XRD analysis revealed the similar volume fraction of the Fe3W3C phase in both types of composite coatings. A relatively significant volume fraction of those complex carbide phases, at the highest HI, (up to about 14 %) is a result of both high dissolution of RPs and the dilution level. In the composite coatings produced at the highest HI level, the fishbone structure was observed mainly in the region near the fusion boundary. These observations indicate that the formation of the fishbone-like phases can be promoted by the high cooling rates and also high Fe concentration.

The matrix mean free path (MFP) between the RPs is affected by both the HI and the shape of the RPs. In the investigated range of the HI, as denoted in Table 2, an increase in the HI increased the MFP from 46 µm ± 25 µm to 62 µm ± 35 µm, and from 37 µm ± 15 µm to 49 µm ± 25 µm in the CCA and CCS, respectively. Differences in the MFP for those coatings can be explained by a different degree of the RPs dissolution but also by the fact that the spherical particles have a better packing ability.

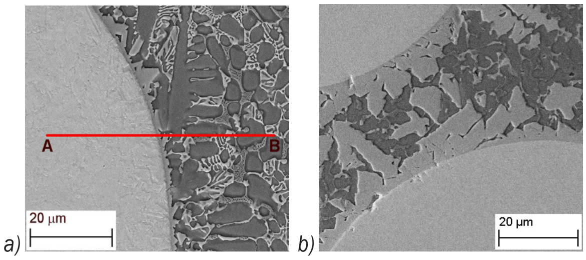

Fig. 9. *Microstructure of the transition region in the CCSs produced at the HI of a) 240 J/mm; and b) 420 J/mm*

All composite coatings contained a crack network induced due to a lack of preheating the substrate. The cracks propagated through the WC particles mainly perpendicular to the fusion boundary and did not affect the integrity of the metallurgical bonding between the coating and the substrate. The presence of Fe_3W_3C phases enhances the coatings' tendency for cracking.

3.3 Microhardness Analysis

Microhardness measurements indicate a general trend towards increasing hardness of the composite coatings with increasing HI levels. This is in qualitative agreement with the microstructural characteristics described in the previous section. Namely, the increase in the HI level leads to both the reduction of the WC volume fraction and the higher mean free path between the WC particles. However, simultaneously the dissolution of WC results in the formation of W-rich secondary phases in the matrix. The average microhardness of the dendritic and blocky Fe_3W_3C phases was found to be 1000 HV±100 HV. Their uniform distribution makes a significant contribution to the matrix hardness of the composite coatings.

3.4 Erosion Behaviour

It was found that erosion the values for both types of composite coatings at an erodent impact angle of 90º were about three (3) times higher than those at 30º. Whereas in the case of the metallic Inconel 625 coating, the relation between the erosion values and erodent angles was inverse: the erosion values at an impact angle of 30º was 100% higher than those at 90º. Additionally, the composite coatings at the impact angle of 30º exhibited even four (4) times higher erosion resistance when compared with that of the metallic coating. In turn, the metallic coating possessed a slightly higher erosion resistance for the 90º impact angle than the composite coatings did. These relationships are attributed to differences in the wear behaviour of the metallic and composite materials for selected erodent impact angles. The erosive wear behaviour of the metallic Inconel 625 coating is typical for ductile materials and has already been well described in the literature [12]. In the case of composite materials, the mechanism of the erosion process is much more complicated because of their complex microstructure. Generally, in this case, the erosion damage is a combination of the brittle and ductile manner of the material loss. That is, material is removed by both chipping and cracking of the RPs and through extrusion and scratching of the ductile matrix alloy. Typical SEM images showing the erosion damage within the wear crater of the CCS and CCA are shown in Figs. 10 and 11, respectively. The erosion degradation mechanism within the wear crater appears quite similar for both types of CCs. However, as denoted in Table 3, there is a significant difference between the erosion values recorded for the CCA and CCS, particularly in the impact angle of 90º. Taking into account the similar hardness of the matrix alloy in these coatings and, in particular, the fact that the CCSs exhibit the lower matrix mean free path (MFP), it can be considered that the above-mentioned difference in erosion resistance of the composite coatings is associated directly with the shape of the RPs. This is consistent with SEM examination of the wear surfaces, which revealed the RP/matrix interfacial decohesion in the CCSs eroded at the impact angle of 30º (Fig. 10b). This manner of RP removal involves the nucleation of a crack and its propagation along the interface between the RP and matrix alloy. It is interesting to note that, due to the smooth RP/matrix interface in the CCSs, the fracture propagates tangentially around the spherical RP, which also indicates a low interfacial bond strength. The EDS spot analysis of the fracture surface revealed high W and Fe content, suggesting that the crack propagation may occur between the RP and, precipitated on its surface, secondary phases. Such a mechanism of the RP removal was not observed in the coatings with the angular RPs. The irregularly shaped RP provides mechanical interlocking with the matrix alloy, significantly improving the RP/matrix interfacial strength.

In the case of the erodent impact angle of 90º, it was observed that the smooth spherical shape of RPs facilitates the removal of the matrix alloy, which consequently leads to cracking and chipping RPs into relatively large pieces. More precisely, the erodent particle impacting the RP, due to the smooth and convex RP/matrix interface, moves tangentially to the surface of RP, scratching it and simultaneously ploughing and cutting the matrix material in the direct vicinity of the RP. The resultant loss of matrix material and further impacts of erodent particles cause cracking of RPs and its dislodgement. The cracks propagate mainly parallel to the eroded surface resulting in the removal of relatively large pieces of the RP.

In contrast, the angular RPs are more effective in protecting the matrix alloy against ploughing and cutting action. In this case, the kinetic energy of erodent particles is dissipated into the work of the fracture of the RPs and also into the plastic

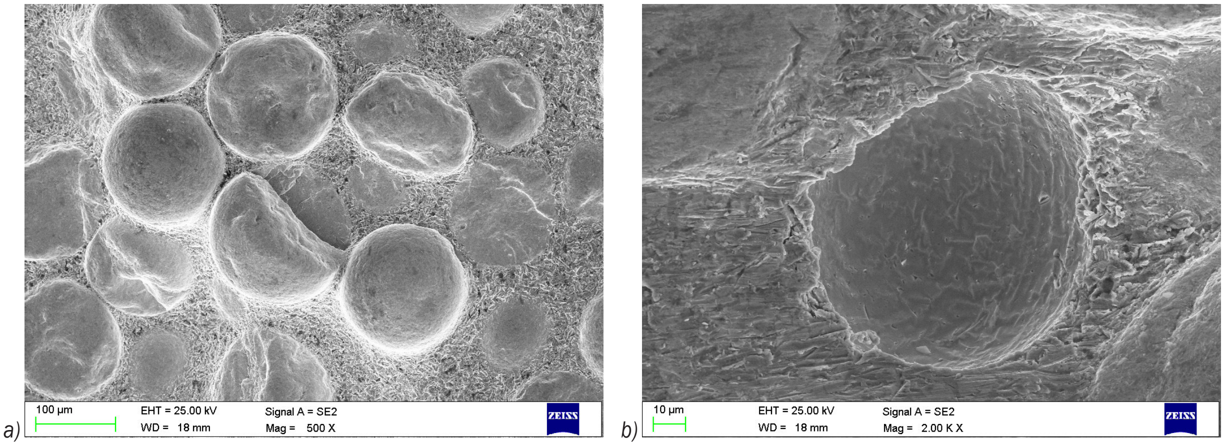

Fig. 10. *SEM image of worn surfaces of the CCSs at impact angle of a) 90°, and b) 30°*

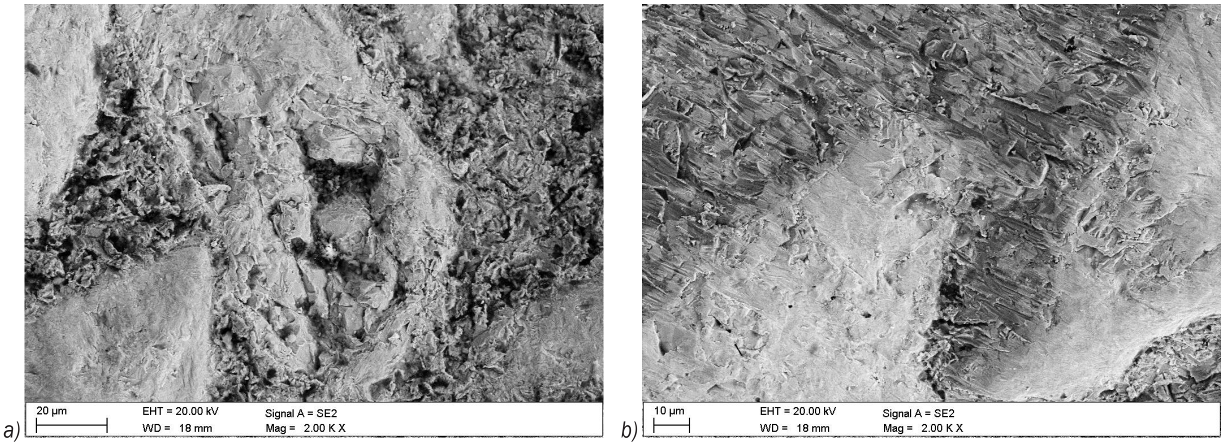

Fig. 11. *SEM image of worn surfaces of the CCAs at impact angle of a) 90°, and b) 30°*

deformation of the matrix. However, as can be seen in Fig. 11a, the angular RP, because of the mechanical interlocking with the matrix and neighbouring RPs, can contribute to the erosion resistance of the coating, even after crack formation. The alloy matrix is removed mainly by the detachment of plastically deformed lips, extruded to the sides of the crater by particle impact. Such erosion behaviour essentially reduces the erosion value.

4 CONCLUSIONS

The HPDD laser-cladded Inconel 625-based composite coatings with both angular and spherical WC reinforcing particles exhibited uniform distributions of WC throughout the matrix and defect-free transition regions between the WC particles and the matrix. With increasing HI, the dissolution of WC increases leading to the formation of secondary W-rich phases in the matrix and especially in the transition regions. The angular WC particles are more susceptible to dissolution in the molten pool than spherical ones are. The top-hat beam profile of the laser used enables to produce composite coatings at very low HI level, leading to a negligible dissolution of WC. At the lowest HI of 240 J/mm, the WC dissolution level was found to be approx. 3 vol% and 10 vol%, in the coatings with spherical and angular WC, respectively. The coatings with angular WC showed the higher matrix mean free path. However, despite the above-mentioned structural characteristic, the coatings with angular WC exhibited higher erosion resistance than those with spherical WC for both normal and oblique impacts. At an impact angle of 90°, erosion values of the coatings with spherical WC were almost 2 times higher than those containing angular WC. This is directly attributed to the excellent mechanical interlocking of irregular WC particles with the matrix and neighbouring WC particles. Whereas in the case of spherical WC, a very smooth interface with the matrix considerably facilitates a removal of the matrix at normal impact. Moreover, the spherical WC particles are prone to the WC/matrix interfacial decohesion at oblique impact.

5 ACKNOWLEDGEMENTS

Publication of this article was funded by a statutory grant of the Faculty of Mechanical Engineering, Silesian University of Technology.

6 REFERENCES

[1] Nurminen, J., Näkki, J., Vuoristo, P. (2009). Microstructure and properties of hard and wear resistant MMC coatings deposited by laser cladding. *International Journal of Refractory Materials and Hard Materials*, vol. 27, no. 2, p. 472-478, **DOI:10.1016/j.ijrmhm.2008.10.008**.

[2] Liyanage, T., Fisher, G., Gerlich, A.P. (2012). Microstructures and abrasive wear performance of PTAW deposited Ni-WC overlays using different Ni-alloy chemistries. *Wear*, vol. 274-275, p. 345-354, **DOI:10.1016/j.wear.2011.10.001**.

[3] Janicki, D. (2012). High power diode laser cladding of wear resistant metal matrix composite coatings. *Solid State Phenomena*, vol. 199, p.587-594, **DOI:10.4028/www.scientific.net/SSP.199.587**.

[4] Tański T. (2014). Determining of laser surface treatment parametres used for light metal alloying with ceramic powders. *Materials Science & Engineering Technology*, vol. 45, no. 5, p. 333-343, **DOI:10.1002/mawe.201400232**.

[5] Lisiecki, A. (2015). Titanium matrix composite Ti/TiN produced by diode laser gas nitriding. *Metals*, vol. 5, no. 1, p. 54-69, **DOI:10.3390/met5010054**.

[6] Cieslak, M.J., Headley, T.J., Roming, A.D., Kollie T., (1988). A melting and solidification study of Alloy 625. *Metallurgical Transactions A*, vol. 19, no. 9, p. 2319-2331, **DOI:10.1007/BF02645056**.

[7] Jiang, D., Hong, C., Zhong, M., Alkhayat, M., Weisheit, A., Gasser, A., Zhang, H. Kelbassa, I., Poprawe, R. (2014). Fabrication of nano-TiCp reinforced Inconel 625 composite coatings by partial dissolution of micro-TiCp through laser cladding energy input control. *Surface and Coatings Technology*, vol. 249, p. 125-131, **DOI:10.1016/j.surfcoat.2014.03.057**.

[8] St-Georges, L. (2007). Development and characterization of composite Ni-Cr+WC laser cladding. *Wear*, vol. 263, no. 1-6, p. 562-566, **DOI:10.1016/j.wear.2007.02.023**.

[9] Klimpel, A., Dobrzański, L.A., Lisiecki, A., Janicki, D. (2005). The study of properties of Ni–WC wires surface deposits. *Journal of Material Processing Technology*, vol. 164-165, p. 1046-1055, **DOI:10.1016/j.jmatprotec.2005.02.195**.

[10] Zhou, S., Huang, Y., Zeng, X., Hu, Q. (2008). Microstructure characteristics of Ni-based WC composite coatings by laser induction hybrid rapid cladding. *Materials Science and Engineering: A*, vol. 480, no. 1-2, p. 564-572, **DOI:10.1016/j.msea.2007.07.058**.

[11] ASTM G76-13 (2013). *Standard Test Method for Conducting Erosion Tests by Solid Particle Impingement Using Gas Jets*. ASTM International, West Conshohocken, **DOI:10.1520/G0076**.

[12] Levin, B.F., Vecchio, K.S., DuPont, J.N., Marder, A.R. (1999). Modeling solid-particle erosion of ductile alloys. *Metallurgical and Materials Transactions A*, vol. 30, no. 7, p. 1763-1774, **DOI:10.1007/s11661-999-0175-9**.

Strojniški vestnik - Journal of Mechanical Engineering 62(2016)6, 373-380
Received for review: 2015-10-07

Received revised form: 2016-02-15
DOI:10.5545/sv-jme.2015.3082
Original Scientific Paper
Accepted for publication: 2016-03-15

Lumped Parameter Modelling of Cavitating Orifice Flow in Hydraulic Systems

Junjie Zhou* – Jibin Hu – Chongbo Jing
Beijing Institute of Technology, National Key Laboratory of Vehicular Transmission, China

Gaseous cavitation is an important issue that introduces negative effects on the performance of hydraulic systems. The lumped parameter modelling approach is widely adopted in the research of hydraulic applications due to its quickness and convenience to apply at the system level. For this reason, a novel lumped parameter model of cavitating orifice flow based on a control volume concept is presented in this paper. In particular, a procedure of calibrating the unknown model coefficients is provided by using the computational fluid dynamic (CFD) method as well as test data. A test rig for studying cavitation in an external gear pump is set up with a variable orifice at the inlet port. The four coefficients in the CFD cavitation model is first identified by the measured mass flow rate through the test orifice; then the CFD simulated fluid field offers required information including the average air mass fraction in downstream region to determine the two coefficients of lumped parameter (LP) model. To further verify the calibrated models, another test at a different pump speed is carried out to compare it to the model prediction. Good matching with experiments justifies the proposed approach and the calibration procedure. Suggestions for future work include extending the approach to the study of hydraulic valves and high-speed pumps.
Keywords: gaseous cavitation; lumped parameter; orifice; hydraulic systems

Highlights

- *This paper presents a novel lumped parameter model of cavitating orifice flow based on the control volume concept.*
- *In the new model, a generalized gas evolution equation is used to calculate the air fraction in the orifice.*
- *A procedure of calibrating the unknown model coefficients in the presented model is proposed.*
- *The calibrated model is verified by experiments.*

1 INTRODUCTION

In hydraulic systems, air release has been considered to be the main reason of gaseous cavitation [1] and [2], which easily happens as the components are subject to low static pressure (air separation pressure). Particularly, due to the upstream side connecting to the oil reservoir, hydraulic orifices or restrictions in the supply system of open circuits, cavitation may be more easily induced [3]. In other cases, the large pressure drop produced by the narrow flow restrictions in hydraulic control valves or the insufficient flow in high-speed rotating hydraulic pumps also indicates a strong tendency of gaseous cavitation [4] and [5]. Nowadays, the bigger pressure ratio or higher shaft speed required by the increasing power density of systems brings a significant challenge to the modelling and designing on the new generation of hydraulic components. The adverse effects of air release including the reduction of flow capacity of hydrostatic units, severe fluid borne noise generation and structural erosion must be minimized in the entire system [6].

As part of the multi-flow subject in fluid dynamics, the cavitation problem has been broadly studied from the interphase mass transfer to various types of applications in recent decades. Significant numerical models of describing multidimensional cavitating flow have been proposed on the basis of the computational fluid dynamic (CFD) approach. Typical examples are given by the models by Singhal et al. [7] (also known as the "full cavitation model"), Zwart et al. [8] and Schnerr and Sauer [9], which are already implemented in commercial software such as ANSYS Fluent [10]. However, these models are very limited to simulate fluid power systems or complex pumps since many aspects which have a substantial impact on the unit performance are neglected, as done in the literature [5] and [11]. For this reason, the lumped parameter (LP) approach is often employed in fluid power research because it is effective, quick as well as robust for studying the dynamic features of hydraulic systems. Not only commercial software such as LMS, AMESim, DSHplus, and Easy 5 but also the advanced numerical models for positive displacement machines [12] and [13] have been developed under this methodology and been highly successful. Applying a homogenous flow method, several lumped parameter fluid models have been proposed by Imagine [14], by Gholizadeh et al. [15] and by Casoli et al. [16]. Researchers have developed a novel fluid model that takes the dynamic features of air release/absorption into account, specifically the one presented in [17]. This model is validated for predicting fluid properties

*Corr. Author's Address: Beijing Institute of Technology, National Key Laboratory of Vehicular Transmission, China, bit_zhou50082@163.com

in a closed control volume and further utilized in the study of outlet pressure oscillations in external gear pumps [6].

In this paper, the cavitating flow through hydraulic orifices is uniquely investigated with the LP approach based on control volumes in Section 2. A CFD model is derived referring to Zwart Model [8], including four empirical constants. Due to the unknown coefficients, Section 3 provides a procedure to calibrate the CFD model and LP model by comparing them with experimental results. Including a variable orifice at the pump inlet port, a test rig of studying cavitation in the hydraulic circuit is built. The measured mass flow rate through the orifice is first used to calibrate the CFD gaseous cavitation model and eventually with the calculated flow field, the coefficients in the LP model are determined. In Section 4, more applications are conducted to further verify the obtained coefficients and the proposed calibration method. Finally, the main conclusions of this work are outlined in Section 5.

2 MATHEMATICAL MODELLING

2.1 Gaseous Cavitation in CFD Approach

In addition to the generalized governing equations (continuity equation, Navier-Stokes equations, and turbulence equations) of describing the flow characteristics in the multi-dimensional fluid field, the vapour transport equation is introduced by researchers to specifically model the cavitation phenomenon in two-phase flow. The previous cavitation models are mainly developed on the basis of water evaporation and condensation [7] to [9]. The difference of existing models only lies in the formulation of describing the interphase mass transfer rates. However, they share the same theoretical basis: bubble dynamics.

Considering the gaseous cavitation (air release) in hydraulic oils, although the interphase mass transfer performs a different mechanism (air release and absorption in oil instead of evaporation and condensation), the gas bubble theory is still regarded to be valid. Therefore, the presented model closely refers to the one proposed by Zwart et al. [8]. Note here that the "gas" discussed in this paper indicates "air" if not specified.

The air volume fraction in the fluid mixture is governed by Eq. (1).

$$\frac{\partial}{\partial t}\left(\alpha\rho_{\mathrm{G}}\right)+\nabla\cdot\left(\alpha\rho_{\mathrm{G}}\vec{V}\right)=R_{\mathrm{r}}-R_{\mathrm{a}}, \tag{1}$$

where α is the gas volume fraction; ρ_{G} is gas density; $\vec{V}$ is the gas phase velocity; R_{r}, R_{a} are the mass transfer terms corresponding to the air release and absorption, respectively.

The Rayleigh-Plesset equation which describes the single bubble is written as [18]:

$$\Re_{\mathrm{b}}\frac{D^2\Re_{\mathrm{b}}}{Dt^2}+\frac{3}{2}\left(\frac{D\Re_{\mathrm{b}}}{Dt}\right)^2= \\ =\left(\frac{p_{\mathrm{b}}-p}{\rho_{\mathrm{L}}}\right)-\frac{4\nu}{\Re_{\mathrm{b}}}\frac{D\Re_{\mathrm{b}}}{Dt}-\frac{2\sigma}{\rho_{\mathrm{L}}\Re_{\mathrm{b}}}, \tag{2}$$

where, $\Re_{\mathrm{b}}$ is bubble radius; p_{b} is bubble surface pressure, which is set as air separation pressure; ρ_{L} is liquid (oil) density.

Similarly, by neglecting the second-order term, the effects of surface tension and liquid viscosity, the Rayleigh-Plesset equation can be deduced as:

$$\frac{D\Re_{\mathrm{b}}}{Dt}=\sqrt{\frac{2}{3}\frac{p_{\mathrm{b}}-p}{\rho_{\mathrm{L}}}}. \tag{3}$$

For simplicity, all the air bubbles in the fluid mixture are considered to be spheres of the same radius. By introducing similar empirical coefficients, the mass transfer terms in Eq. (1) can be given as:

$$R_{\mathrm{r}}=C_{\mathrm{r}}\alpha_{\mathrm{nuc}}\frac{3(1-\alpha)\rho_{\mathrm{G}}}{\Re_{\mathrm{b}}}\sqrt{\frac{2}{3}\frac{p_{\mathrm{b}}-p}{\rho_{\mathrm{L}}}}, \\ R_{\mathrm{a}}=C_{\mathrm{a}}\frac{3\alpha\rho_{\mathrm{G}}}{\Re_{\mathrm{b}}}\sqrt{\frac{2}{3}\frac{p-p_{\mathrm{b}}}{\rho_{\mathrm{L}}}}, \tag{4}$$

where, besides the bubble radius $\Re_{\mathrm{b}}$, the air release coefficient C_{r}, air absorption coefficient C_{a} and the nucleation site volume fraction α_{nuc} are unknown.

By comparing the simulation to the experimental data, Zwart et al. [8] proposed a set of values through the study of water vaporous cavitation. However, concerning hydraulic oils and the different mass transfer mechanism, the model coefficients may be different. Therefore, more work is necessary to confirm the suitable values of these four coefficients, hence extending the usability of the CFD cavitation model.

2.2 Lumped Parameter Modeling Approach

The lumped parameter approach for modelling hydraulic systems is based on control volumes (CV), in which fluid properties are taken as uniform. For our study, the main structure of a hydraulic orifice is illustrated in Fig. 1, including three CVs: the upstream region, the throat region (CV_1) and the downstream region (CV_2).

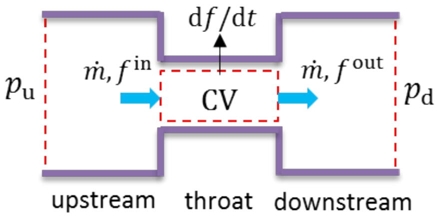

Fig. 1. *Control volumes and flow exchanges in hydraulic orifice*

The first significant step of modelling cavitating orifice flow is to predict the air content (mass fraction in this study) in each CV. This is easier for CFD method since all the information including air volume fraction distribution is calculated in the entire fluid field. To achieve this goal, a generalized formulation of governing the air mass fraction in the control volume has been presented in the authors' previous work **[19]**, as written in Eq. (5).

$$\frac{df}{dt}=\left.\frac{df}{dt}\right|_{IT}+\frac{1}{m}\left(\Sigma\dot{m}_{in}f^{in}-\Sigma\dot{m}_{out}f^{out}\right)-\frac{f}{V}\frac{dV}{dt}, \quad (5)$$

where f is the air mass fraction; $\left.\frac{df}{dt}\right|_{IT}$ represents the internal transport effect; m is the fluid mass in the control volume.

Regarding one open control volume connected to some other CVs, the basic idea of this formulation comes from the fact that the mass balance of air in the CV includes two important effects: the internal mass transport – air release or absorption driven by the pressure difference and the external mass exchange interacting with adjacent CVs. In order to acquire air release/absorption rates in the air-oil system, in the author's previous work **[17]** a simplified equation is derived from "Full Cavitation Model" and validated for the cases of cyclic compression/expansion processes using a closed chamber. In this study, a similar equation is employed to evaluate the internal mass transport:

$$\left.\frac{df}{dt}\right|_{IT}=z(1-f)\sqrt{p_b-p}, \quad (6)$$

where z also indicates a complex coefficient mainly related to geometric features of the studied structure and the operating condition.

Applying Eq. (5) and Eq. (6) on the cases of CV_1 and CV_2 of cavitating orifice shown in Fig. 1, since the volumes do not change, a set of equations of air content can be obtained:

$$\begin{cases}\dfrac{df_1}{dt}=z_1(1-f_1)\sqrt{p_b-p_1}+\dfrac{1}{m_1}\left(\dot{m}f_1^{in}-\dot{m}f_1^{out}\right)\\[2ex] \dfrac{df_2}{dt}=z_2(1-f_2)\sqrt{p_b-p_2}+\dfrac{1}{m_2}\left(\dot{m}f_2^{in}-\dot{m}f_2^{out}\right)\end{cases}. \quad (7)$$

Being focused on the steady-state study, it is reasonable to set the time-derivative of mass fractions of CV_1 and CV_2 as 0. The mass flow rate through each connecting boundary should be the same due to mass conservation. The pressure in both regions is assumed to be approximately the downstream boundary pressure p_d, and this point will be justified by the CFD simulation in Section 3.

In addition, due to that, air release mainly happens in CV_1 and CV_2, the flow coming from the upstream region is considered to be pure oil, meaning no air entrained in the entering flow of CV_1. Furthermore, the mass fraction in outlet flow is supposed to equal to the value of source volume. Therefore, the following relations are also imposed.

$$f_1^{in}=0,\quad f_1^{out}=f_2^{in}=f_1,\quad f_2^{out}=f_2. \quad (8)$$

Then, Eq. (7) can be deduced as:

$$\begin{cases}z_1m_1(1-f_1)\sqrt{p_b-p}=\dot{m}f_1\\ z_2m_2(1-f_2)\sqrt{p_b-p}=\dot{m}f_2-\dot{m}f_1\end{cases}. \quad (9)$$

In Eq. (9), all the unknown variables (m_1, m_2, f_1, f_2, $\dot{m}$) can be calculated from the CFD simulation results except the empirical constants (z_1, z_2). Therefore, it is possible to calibrate their values by using simulation data once the CFD cavitation model is successfully standardized. In other words, the CFD model will be first calibrated by experimental data, and then it will help to further calibrate the lumped parameter model.

Suppose that the reasonable coefficients (z_1, z_2) have been captured by the above procedure, there is still one problem in solving this equation (take the air mass fraction f_1, f_2 as unknowns) because the mass flow rate needs more consideration.

Fig. 2 illustrates the basic structure and boundary condition of the two-phase orifice flow, where, is the upstream pressure and p_u is the downstream pressure. The cross-sectional area of the throat is noted by A.

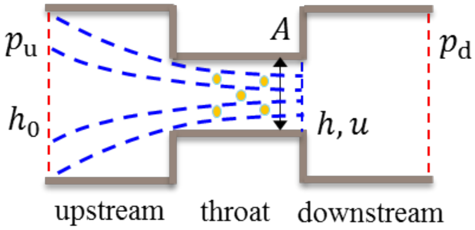

Fig. 2. *Fluid field of two-phase orifice flow*

Starting from the energy view, the specific enthalpy on both sides of fluid mixture is:

$$h_0 = h + \frac{u^2}{2} = fh_G + (1-f)h_L + \frac{u^2}{2}, \tag{10}$$

where u indicates the velocity of fluid mixture; h_G, h_L and h are the enthalpy of gas, liquid, and mixture, respectively.

Then the mass flow rate through orifice is obtained as:

$$\dot{m} = C_q A \rho_H u, \tag{11}$$

where the density of the fluid mixture is evaluated by Eq. (12).

$$\frac{1}{\rho_H} = \frac{f}{\rho_G} + \frac{1-f}{\rho_L}. \tag{12}$$

If the energy changes of gas and liquid are independent, one can derive:

$$h_0 - h = f\left(h_{G0} - h_G\right) + (1-f)\left(h_{L0} - h_L\right). \tag{13}$$

The pressure ratio is:

$$k = \frac{p_d}{p_u}. \tag{14}$$

The change of gas enthalpy is given as:

$$h_{G0} - h_G = c_p T_0 \left(1 - \frac{T}{T_0}\right), \tag{15}$$

where, c_p is specific heat of gas; T_0 is the constant temperature.

As the flow is considered to be the isentropic flow, the term $p^{1-\lambda}\ T^{\lambda}$ will be constant. Therefore, the following relation can be derived:

$$\frac{T}{T_0} = \left(\frac{p_d}{p_u}\right)^{\frac{\lambda-1}{\lambda}}. \tag{16}$$

Then, substituting Eq. (16) into Eq. (15), the first term in Eq. (13) becomes:

$$f\left(h_{G0} - h_G\right) = fc_p T_0 \left(1 - k^{\frac{\lambda-1}{\lambda}}\right). \tag{17}$$

For the liquid phase, if the slight change of the oil temperature in other words the internal energy through the orifice is ignored, one can obtain:

$$(1-f)\left(h_{L0} - h_L\right) = (1-f)\left(\frac{p_u}{\rho_L} - \frac{p_d}{\rho_L}\right) = $$

$$= (1-f)\frac{p_u}{\rho_L}(1-k). \tag{18}$$

Combining Eq. (11) to Eq. (18), the mass flow rate through the orifice is formulated as the function of air content as follows:

$$\dot{m} = C_q A \frac{\sqrt{B_1(f)\left(1 - k^{\frac{\lambda-1}{\lambda}}\right) + B_2(f)(1-k)}}{B_3(f)k^{-\frac{1}{\lambda}} + B_4(f)}, \tag{19}$$

where $B_1 = 2fc_p T_0$, $B_2 = 2(1-f)\dfrac{p_u}{\rho_L}$,

$B_3 = \dfrac{f}{\rho_{G0}}\left(\dfrac{p_u}{p_0}\right)^{-1/\lambda}$, $B_4 = \dfrac{1-f}{\rho_L}$.

Thus far, it is evident that the mass flow relates to the gas mass fraction. Because the pressure ratio is known from the boundary condition, the mass flow rate only depends on f. Combining with Eq. (19), Eq. (9) is closed.

3 CALIBRATION OF MODEL COEFFICIENTS

3.1 Experimental Setup

A test rig is built to offer the necessary data to perform the parameter calibration. The experimental setup, illustrated by the diagram of Fig. 3, permits the measurements of steady-state flow rate and pressure. A variable orifice is installed to create a desired low pressure at the pump inlet pipe. This orifice can be operated to induce different low pressures or insufficient flows at the inlet port; meanwhile, the pressure is measured by P2. Another variable orifice is placed in outlet pipe serving as the pressure load. The main fluid parameters and equipment specifications are presented in the next table.

The test data used in model calibration are obtained at the operation condition of 1500 rpm shaft speed, 100 bar outlet pressure. By adjusting the inlet orifice opening area at the same speed and load pressure, insufficient oil filling happens first, and then the downstream pressure (P2) starts to decrease.

When the inlet pressure drops under air separation pressure (about the same as the atmosphere pressure), the air separates from the oil, hence inducing gaseous cavitation. Three cases are run, and all the data of inlet pressure, outlet flow rate, and even pressure oscillations are collected. It should be mentioned here that the mass flow rate was evaluated from the test data of Q1 since the oil density is known.

Table 1. *Features of fluid and main elements of the apparatus*

Element	Type	Main features
Hydraulic oil	ISO VG 46 mineral oil	Density: 840 kg/m^3, Operating temperature: 298 K; Air separation pressure: 1.05 bar
P2	Strain gage	WIKA®, Scale: 0 bar to 40 bar, 0.25 % FS accuracy
P4	Strain gage	WIKA®, Scale 0 bar to 40 bar, 0.25 % FS accuracy
P3	Piezoelectric	KISTLER®, Scale: 0 bar to 1000 bar, 140 kHz Natural frequency, 0.8 % FS accuracy
Q1	Flow meter	VSE® VS1, Scale 0.05 l/min to 80 l/min, 0.3 % measured value accuracy

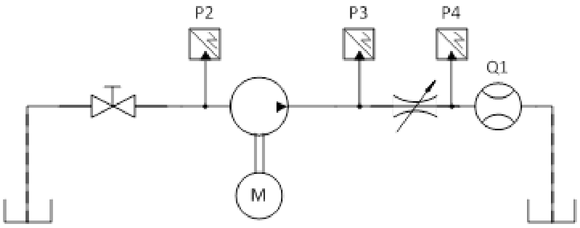

Fig. 3. *Diagram of the external gear pump test system*

3.2 Calibration of Model Coefficients

Due to the axisymmetric structure, the upper half area of the orifice is used as the 2D computational field, as shown in Fig. 4.

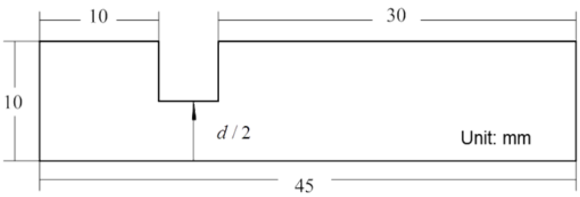

Fig. 4. *Main dimensions of test orifice fluid field*

In order to calibrate empirical coefficients in the CFD gaseous cavitation model, three parameter sets are carefully chosen based on the experience of previous research including Set A proposed by Zwart et al. [8], Set B proposed by Campo et al. [5] and Set C provided by the authors. All the values are shown in Table 2.

Table 2. *Tested coefficient sets for the CFD cavitation model*

Set	$\Re_b$ [μm]	α_{nuc}	C_r	C_a
A	1	5e-4	0.4	0.001
B	10	0.09	0.4	0.001
C	10	5e-4	0.09	0.01

Simulations are run in an ANSYS Fluent environment with meshes generated from Gambit. In the CFD model, the standard k-epsilon turbulence model is employed. The problem is simplified as a 2D model as it is an "axisymmetric swirl". Fig. 5 shows the quadrilateral mesh of the fluid field, and it consists of 3400 cells in the present selection. The grid independence is checked by comparing the results between the presented grid with one encrypted grid which includes four times the number of cells. The relative error for all the three simulated cases is limited to 2.7 %; thereby the present mesh is chosen.

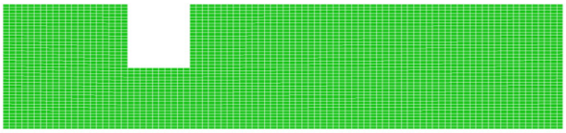

Fig. 5. *The CFD mesh used in the fluid field*

The outlet pressure used as the boundary condition in the CFD model is set according to the measured value of P2. Table 3 shows the operating parameters and simulated results obtained for each coefficient set tested. The pressures are given in absolute values in order to avoid negative numbers. Upstream pressure is calculated from the height of the tank position, and the throat diameter is estimated according to the valve-opening area. From the comparison to test data, it is clear that Set A and Set B have a strong tendency to overestimate cavitation effects, which do not match

Table 3. *Operating parameters and CFD simulation results*

Case	p_u [bar]	p_d [bar]	d [mm]	Q_t [L/min]	$\dot{m}_t$ [kg/m^3]	$\dot{m}_s$ - A [kg/m^3]	$\dot{m}_s$ - B [kg/m^3]	$\dot{m}_s$ - C [kg/m^3]
1	1.05	0.94	9.8	16.3	0.2309	0.1674	0.1561	0.2484
2	1.05	0.37	6.0	15.7	0.2198	0.1391	0.0811	0.2162
3	1.05	0.28	5.4	13.4	0.1876	0.1213	0.0683	0.1848

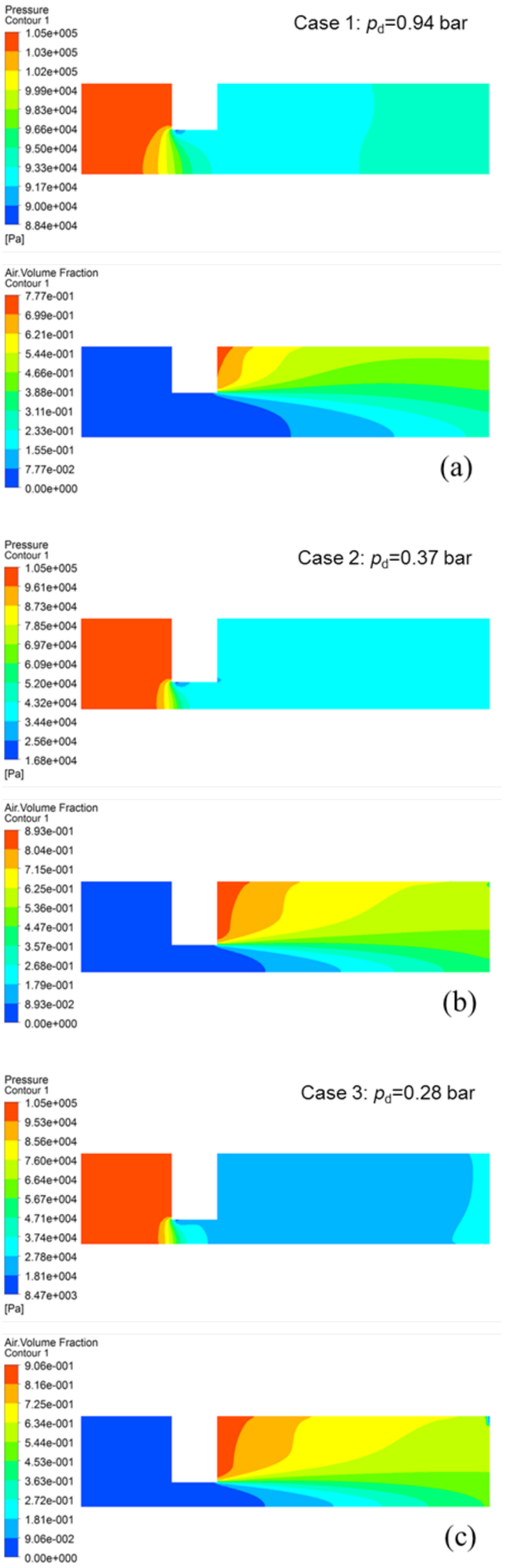

Fig. 6. *Static pressure and air volume fraction in the fluid field; a) case 1, b) case 2, and c) case 3*

the measured mass flow rates. The result predicted by Set C seems more reasonable for all three cases. Therefore, the coefficients of the gaseous cavitation model in hydraulic oil are calibrated as the values of Set C.

Fig. 6 displays the static pressure and air volume fraction for each case predicted by the Set C cavitation model. It is easy to understand, with lower downstream pressure, more air appears in CV_1 and CV_2. In all cases, the pressure distributions in CV_1 and CV_2 are relatively close to p_d, which confirms the assumption made in section 2.2. In addition, from the air volume fraction contours, the air content at the inlet of can be neglected as also done in Section 2.2.

From the CFD results, all the information, including average air mass fraction (f_1, f_2), mass of fluid mixture (m_1, m_2), which are needed to calibrate the lumped parameter model, are obtained in the post processing module. Then, depending on Eq. (9), the empirical coefficients (z_1, z_2) in the LP model are solved. Table 4 lists the key variables and the obtained coefficient values in the LP cavitation model.

Table 4. *Key variables and calculated coefficient values*

Case	f_1	f_2	z_1	z_2
1	3.52e-5	8.73e-4	3.47e-4	5.54e-4
2	5.31e-5	19.4e-4	3.80e-4	5.47e-4
3	5.24e-5	21.9e-4	3.74e-4	5.68e-4

In Table 4, due to the slight difference observed on the quantity of and , the LP model coefficients can be regarded as constant for the given orifice structure, although they may differ more for other orifices. From this point, the LP model is determined with the coefficients set as z_1 =3.6e-4 and z_2 =5.6e-4. Hence, the LP model will be applicable for other situation, because both the air mass fraction in CV_1, CV_2, and the mass flow rate passing the orifice can be obtained by solving Eq. (9) and Eq. (19) simultaneously.

4 MODEL APPLICATION

In order to further check the ability and applicability of the developed CFD and LP cavitation models, the tested pump is run at another shaft speed (1000 rpm) with four different opening positions of the inlet orifice. Using the proposed model coefficients, the mass flow rates predicted by both methods are compared to measured data, as depicted in Fig. 7.

From Fig. 7, it can be seen that the simulation results from both CFD model and LP model provide acceptable accuracy on predicting the mass flow rate, although they are not able to depict all measured aspects. Therefore, the calibrated coefficients are convincing and, more importantly, the proposed procedure of model calibration, particularly for the lumped parameter modelling approach, is justified. It is worth mentioning, although this method is built in terms of the employed orifice structure, it can be extended to other geometric configurations, such as various types of hydraulic valves.

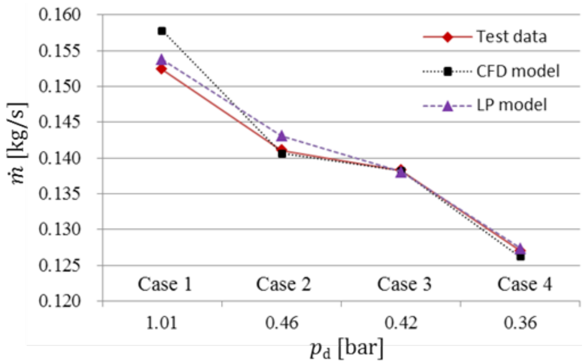

Fig. 7. *Measured and predicted mass flow rates from CFD model and LP model at 1000 rpm shaft speed*

5 CONCLUDING REMARKS

This paper presents a novel model for predicting gaseous cavitation in hydraulic orifices. By simplifying the orifice as three connected control volumes, the cavitating flow is described by using the lumped parameter modelling approach. In order to calibrate the model coefficients in LP model, the orifice flow is also studied with the popular CFD method because the CFD model is easy to compare with the real test. An experimental apparatus of testing cavitation in hydraulic pump circuit is built, where a variable orifice is placed at the inlet line to induce low pressure.

As the procedure of model calibration, the measured mass flow rate through the orifice at three downstream pressures is first used to calibrate the four coefficients in CFD model. After choosing the suitable values, the simulated fluid field from Fluent is captured to further calculate the required parameters of demarcating the LP cavitation model. Then, the obtained empirical coefficients in both approaches are employed in the simulation of other operating conditions with different pump speeds. The agreement with experimental data shows good potentials of the proposed lumped parameter cavitation model, which is considered more suitable for cavitation study happening in hydraulic systems.

The success of this research can drive future work on the study of gaseous cavitation in hydraulic control valves or high-speed pumps.

6 ACKNOWLEDGEMENTS

This research is funded by National Science Foundation of China (Grant No. 51505030).

7 NOMENCLATURES

A	cross-sectional area, [m²]
B_1, B_2, B_3, B_4	parameters for calculating mass flow rate
C_q	orifice flow coefficient
C_a	air release coefficient
C_r	air absorption coefficient
Q	flow rate, [L/min]
R_a	mass transfer due to air release
R_r	mass transfer due to air absorption
T_0	constant temperature, [K]
V	volume, [m³]
c_p	specific heat, [J/(kg·K)]
d	diameter, [m]
f	mass fraction of air
h	specific enthalpy of fluid mixture, [J/kg]
h_0	initial specific enthalpy of fluid mixture, [J/kg]
m	mass, [kg]
$\dot{m}$	mass flow rate, [kg/s]
$\dot{m}_t$	theoretical mass flow rate, [kg/s]
$\dot{m}_s$	simulated mass flow rate, [kg/s]
k	pressure ratio
p	pressure, [bar]
p_b	air separation pressure, [bar]
t	time, [s]
u	velocity, [m/s]
z	coefficients in LP model
$\Re_b$	bubble radius, [m]
α	volume fraction
α_{nuc}	nucleation site volume fraction
ρ	density, [kg/m²]
λ	polytrophic index of gas
σ	surface tension,
v	kinematic viscosity, [m²/s]

Subscripts

IT	internal transport
G	gas (air)
G_0	initial state of gas (air)
L	liquid
L_0	initial state of liquid
H	fluid mixture
in	inlet port

out outlet port
u upstream
d downstream
t test data
s simulation data
0 initial condition
1 control volume 1
2 control volume 2

7 REFERENCES

[1] Wylie, E.M., Streeter, V.L. (1978). *Fluid Transient*, Michigan University Press, Ann Arbor.

[2] Gholizadeh, H., Burton, R., Schoenau, G. (2011). Fluid bulk modulus: a literature survey. *International Journal of Fluid Power*, vol. 12, no. 3, p. 5- 16, **DOI:10.1080/14399776.2011.10781033**.

[3] Vacca, A., Klop, R., Ivantysynova, M. (2010). A numerical approach for the evaluation of the effects of air release and vapor cavitation on effective flow rate of axial piston machines. *International Journal of Fluid Power*, vol. 11, no. 1, p. 33-46, **DOI:10.1080/14399776.2010.10780996**.

[4] Wiggert, D.C., Sundquist, M.J. (1979). The effect of gaseous cavitation on fluid transients. *ASME Journal of Fluids Engineering*, vol. 101, no. 1, p. 79-86, **DOI:10.1115/1.3448739**.

[5] del Campo, D., Castilla, R., Raush, G.A., Gamez Montero, P.J., Codina, E. (2012). Numerical analysis of external gear pumps including cavitation. *ASME Journal of Fluids Engineering*, vol. 134, no. 8, article 081105, **DOI:10.1115/1.4007106**.

[6] Zhou, J., Vacca, A., Casoli, P., Lettini, A. (2014). *Investigation of the Impact of Oil Aeration on Outlet Flow Oscillations in External Gear Pumps*. International Fluid Power Expo, Las Vegas.

[7] Singhal, A.K., Athavale, M.M., Li. H.Y., Jiang, Y. (2002). Mathematical Basis and Validation of the Full Cavitation Model. *ASME Journal of Fluids Engineering*, vol. 124, no. 3 p. 617-624, **DOI:10.1115/1.1486223**.

[8] Zwart, P.J., Gerber, A.G., Belamri, T. (2004). A two-phase flow model for predicting cavitation dynamics. *Proceedings of the 5th International Conference on Multiphase Flow*, Yokohama.

[9] Schnerr, G.H., Sauer, J. (2001). Physical and numerical modeling of unsteady cavitation dynamics. *4th International Conference on Multiphase Flow*, New Orleans.

[10] ANSYS FLUENT 12.0 (2009). *Theory Guide - 16.7.4 Cavitation Models*, Ansys, Canonsburg.

[11] Saxena, D. (2008). *CFD Modeling of Cavitation in Axial Piston Pump*. Purdue University, West Lafayette.

[12] Vacca, A., Guidetti, M. (2011). Modelling and experimental validation of external spur gear machines for fluid power applications. *Simulation and Modeling Practice and Theory*, vol. 19, no. 9, p. 2007-2031, **DOI:10.1016/j.simpat.2011.05.009**.

[13] Pelosi, M., Ivantysynova, M. (2011). The influence of pressure and thermal deformation on the piston/cylinder interface film thickness. *Proceedings of the 52nd National Conference on Fluid Power*, Las Vegas.

[14] IMAGINE S.A. (2007). HYD Advanced Fluid Properties, *Technical Bulletin*, no. 117, Rev7.

[15] Gholizadeh, H., Burton, R., Schoenau, G. (2012). Fluid bulk modulus: comparison of low pressure models. *International Journal of Fluid Power*, vol. 13, no. 1, p. 7-16, **DOI:10.1080/14399776.2012.10781042**.

[16] Casoli, P., Vacca, A., Franzoni, G., Berta, G.L. (2006). Modeling of fluid properties in hydraulic positive displacement machines. *Simulation Modeling Practice and Theory*, vol. 14, no. 8, p. 1059-1072, **DOI:10.1016/j.simpat.2006.09.006**.

[17] Zhou, J., Vacca, A., Manhartsgruber, B. (2013). A novel approach for the prediction of dynamic features of air release and absorption in hydraulic oils. *ASME Journal of Fluids Engineering*, vol. 135, no. 9, article 091305, **DOI:10.1115/1.4024864**.

[18] Brennen, C.E. (1995). *Cavitation and Bubble Dynamics*, Oxford University Press, Oxford.

[19] Zhou, J., Vacca, A., Casoli, P. (2014). A novel approach for predicting the operation of external gear pumps under cavitating conditions. *Simulation Modelling Practice and Theory*, vol. 45, p. 35-49, **DOI:10.1016/j.simpat.2014.03.009**.

Strojniški vestnik - Journal of Mechanical Engineering 62(2016)6, 381-388

DOI:10.5545/sv-jme.2015.3202
Original Scientific Paper
Received for review: 2015-11-15
Received revised form: 2016-04-06
Accepted for publication: 2016-04-26

Measuring Selected Parameters of Polypropylene Fibre Heat Exchangers

Mária Čarnogurská[1,*] – Miroslav Příhoda[2] – Marián Lázár[1] –
Natália Jasminská[1] – Róbert Gallik[1] – Michal Kubík[1]
[1]Technical University of Košice, Faculty of Mechanical Engineering, Slovakia
[2]Technical University of Ostrava, Faculty of Metallurgy and Materials Engineering, Czech Republic

Heat exchangers whose heat exchange surfaces are made of the miniature polypropylene fibres are still under development. In the first phase of researching such exchangers, the possibility of attaching fibres into bundles was tested. The number of threads in one bundle ranges from several hundred to thousands of pieces. The sensitive element in the application of the fibres in a heat exchanger is the place where all the fibres are bundled together, into so-called potting, which must be perfectly tight. Pressure loss was measured in such bundles, depending on the water flow and the temperature at the entry and exit of the exchanger. The results allowed the definition of the overall heat transfer coefficient from one medium through the fibre wall to the other media and to determine the thermal performance of the exchanger. Experimental data shows that water-to-water heat exchanger reached the overall heat transfer coefficient value of to 800 W·m^{-2}·K^{-1}, depending on the release rate of the bundle. Subsequently, for the given conditions, the heat transfer rate depends only on the size of the heat transfer surface area, thus the number of fibres in the bundle.
Keywords: polypropylene fibre, heat exchanger, measurement

Highlights
- *A new type of heat exchanger whose heat exchange surface consists of polypropylene fibres has been designed and tested.*
- *A testing seal potting apparatus has been developed.*
- *Media temperature, flow rate and pressure drop in selected bundles of fibres with transparent and porous fibre were measured.*
- *The impact of fibre length on the value of the overall heat transfer coefficient for this new type of heat exchanger was examined.*

0 INTRODUCTION

Currently, the proposed design of heat exchangers and other equipment must satisfy complex requirements in terms of production technology [1] and [2], trouble-free operation [3] and economic feasibility [4] and [5]. The main requirements for heat exchangers include a large overall heat transfer coefficient, low flow resistance, a simple process of cleaning the heat transfer surface area, corrosion resistance in various transported media, adaptation of the shape of the heat exchanger to the specified manufacturing needs, as well as price [6] and [7].

The critical operating parameters being monitored in heat exchangers include [8] and [9]:
- Operating pressure: that can range from a deep vacuum in fractions of Pa to pressures reaching tens of MPa.
- Operating temperature: from values close to absolute zero up to 1000 °C and higher.
- Mass flow rate: from a few grams to hundreds of kilograms of media per second.
- Good accessibility to a heat exchange area (necessary condition for cleaning and checking the status of working surfaces, especially when working with corrosive chemicals or a heterogeneous suspension with a tendency to form deposits, encrustations and corrosion).

Decontamination and hygiene of a heat exchange surface is a specific condition for heat exchangers in the area of food and medical technologies. In addition to physical and chemical cleanliness, decontamination requirements also include bacterial cleanliness and harmlessness of heat exchange surfaces.

In industrial practice, the most often used heat exchangers are constructed of steel or other metals; plastic is used less commonly as a construction material.

As for plastic heat exchangers, the advantage is the durability of the material (up to 50 years), resistance to corrosion, chemicals and bacteria, high sanitary standards and low volume weight.

One of the disadvantages of plastic heat exchangers is their lower material strength in comparison to metal exchangers, low resistance to higher temperatures (max. 150 °C), lower resistance to mechanical damage, risk of penetration of the diffused oxygen into the cooling medium, as well as a lower connection quality [10] and [11].

*Corr. Author's Address: University of Košice, Faculty of Mechanical Engineering, Košice, Slovakia, maria.carnogurska@tuke.sk

Individual parts of a heat exchanger are connected by glue or are welded. Welded constructions of heat exchangers are of a better quality and also find application in highly aggressive environments.

A particular feature of plastic heat exchangers is that they are not produced in a gilled configuration because of the low thermal conductivity of the plastic.

A separate group of plastic heat exchangers are heat exchangers in which the heat exchange surface is made of polypropylene fibres (capillaries) [12] and [13].

Other cited works state the results of experiments by individual authors related to, for example, the possibility of using heat exchangers with polypropylene fibres to obtain waste heat from domestic and industrial water was assessed [14] and [15], the studies of the affinity of polypropylene fibres for biological pollution in comparison with stainless steel (Escherichia coli bacteria) [16], the use of exchangers with polypropylene fibres (as a source of heat) for thermal pumps was investigated [17], the interaction between the movement of fibres and heat transfer was monitored, the impact of the shape and size of the heat exchanging area upon the output of the exchanger was assessed the use of exchangers with polypropylene fibres (as a source of heat) for thermal pumps was investigated [18] and [19], etc.

The geometry of polypropylene fibres is shown in Fig. 1.

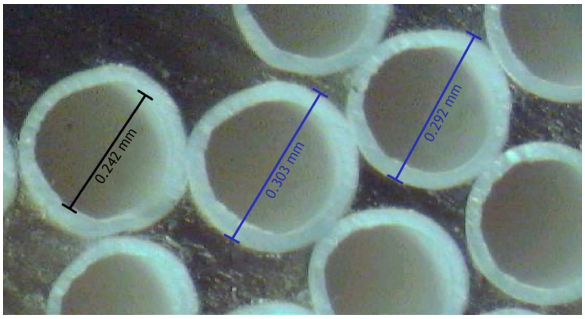

Fig. 1. *The polypropylene fibres - 200× magnifications*

Table 1. *Basic physical characteristics of propylene* [21]

Measured parameter	Value
Density [g·cm⁻³]	0.95 (crystal)
	0.895 (amorphous)
Melting point [°C]	173
Decomposition point [°C]	286
Thermal expansion [K⁻¹]	(100 to 180)·10⁻⁶
Specific thermal capacity [kJ·kg⁻¹·K⁻¹]	1.70 to 1.90
Water absorption [%]	0.03
Hardness [Rockwell]	R80 to R100
Thermal conductivity [W·m⁻¹·K⁻¹]	0.16 to 0.25

Polypropylene is a thermoplastic polymer selected from the group of polyolefins; it is colourless and odourless [20] and [21]. It has good stability, hardness and strength, but low impact strength. It is not susceptible to internal stress and can be appropriately welded. It has excellent electrical and chemical resistance. It becomes fragile at temperatures below zero. The basic physical properties of polypropylene are shown in Table 1.

1 STUDY AREA

In the first phase of designing a heat exchanger surface made of polypropylene fibres, research was carried out to see if there was the possibility of joining polypropylene fibres into bundles. A created bundle (Fig. 2) consists of 1400 pieces of fibre. Those fibres are inserted into a 20 mm diameter and 40 mm long PVC tube. The part of the fibres that is glued into a single unit, and forms a compact unit in a PVC tube, is the so-called potting. Fig. 3 shows a sectional view of an array of 18 pottings in a single shell of a heat exchanger. The manner in which the bundles are placed, and especially by their number, makes it possible to influence the thermal performance of the heat exchanger.

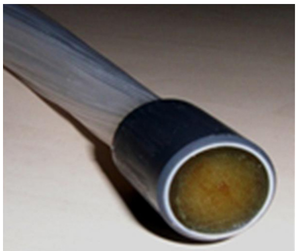

Fig. 2. *Fibre bundle in a potting*

Fig. 3. *System of pottings – side cut*

The fibres are produced by continuous casting of liquid polypropylene from an extruder. Subsequently, the fibre is cooled in an air stream, thereby shrinking into the given dimension. Fibres suitable for the use in a heat exchanger should have intact and smooth walls, i.e. so-called transparent fibres. In contrast, research is underway to examine the possibility of using a porous fibre mainly for medical purposes. The wall of such fibres consists of 30 % to 50 % air.

The second phase of the design tested the potting leaks. Table 2 contains the selected technical parameters of a bundle of polypropylene fibres.

The bundle is tested for the so-called *collapse pressure* and *burst pressure*. *Collapse pressure* is an overpressure from the outside of the fibre wall towards the inside wall, following which the fibre wall collapses. *Burst pressure* indicates the overpressure inside of the capillary against the external pressure, following which there is a rupture of the capillary wall.

Table 2. *Technical parameters of a polypropylene fibre bundle*

Parameter	Value
Capillary material	Polypropylene
Potting material	Polyurethane
Number of capillarie	1400
Total length	750 mm
Capillaries inner diameter	0.225 mm
Outer diameter of capillaries	0.275 mm
Collapse pressure	0.2 MPa
Burst pressure	0.4 MPa
Maximal operating temperature	70 °C
Approx. heat transfer area	1 m^2

2 CHARACTERISTICS OF POLYPROPYLENE FIBRES

Polypropylene fibres can deform or even break when cut, or after being glued in the potting. A rupture occurs when the adhesive does not completely fill the empty space between the fibres. A rupture is a permanent deformation of the fibre cross-section, i.e. reduced cross-section (Fig. 4).

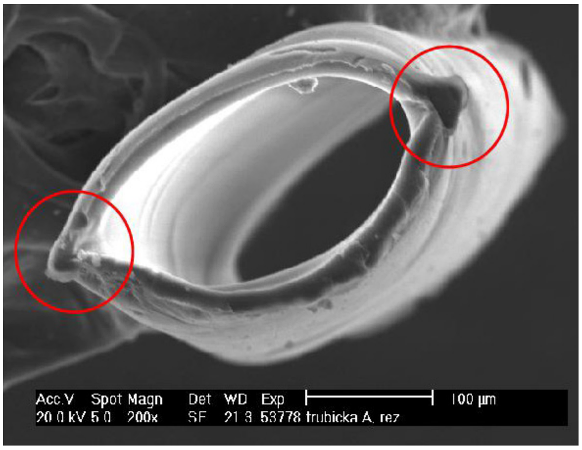

Fig. 4. *Polypropylene fibre cut- 200× magnification*

Wall thickness changes along the length of an intact fibre. Fig. 5 shows a microsection of the wall at 1500× magnification. The changing of the wall thickness is chaotic; it is not subject to any dependency, not only along the cross-section but also along the length of the capillary. The wall thickness of the presented capillary ranges from 30 µm to 33 µm.

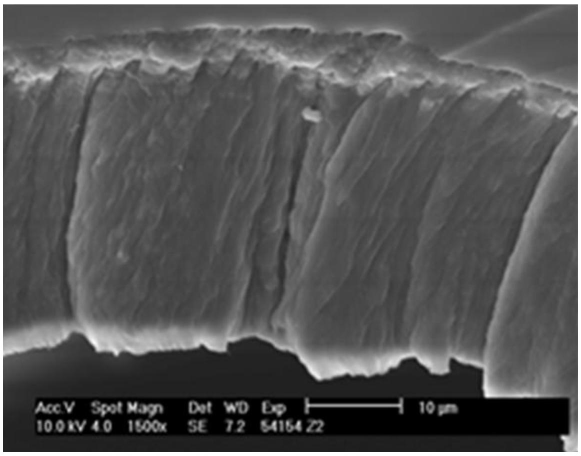

Fig. 5. *Microsection of the wall along the length of the fibre – 1500× magnification*

3 TESTING POTTING INTEGRITY

As a potting is made of three different materials with differing properties, it was necessary to conduct an integrity test. The test device is shown in Fig. 6.

Water coming from a pressurized water source passes through a water filter (1), continues through a closing valve (2) and after the control pressure gauge (3) it enters the first potting. The water flows through the fibre bundle and enters the second potting (5). Subsequently, the water flows through the control pressure gauge (6) and the closing valve (7), which flows into a collecting tank. The water pressure at the inlet of the water filter was set to 0.3 MPa. Water flowing under this pressure for 30 s expelled the air contained in the fibres of the bundle. Subsequently, the valves were closed before and after the bundle; the pressure drop in the fibre bundle was observed for 5 min.

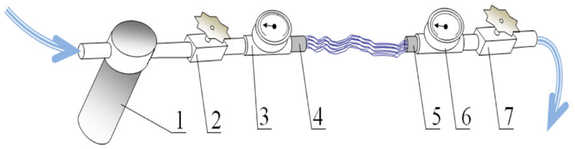

Fig. 6. *Scheme of a potting's' integrity measurement*

This particular experiment was conducted in order to identify a possible problem with the tightness of the bundle. A fibre bundle with detected leakage was immersed into a water tank at 50 °C to 70 °C together with a protective package perforated with about 30 holes, 3 mm in diameter. The packaging was tasked to protect fibres from mechanical damage during the repeat experiment. After cooling the fibre to the level of the inlet temperature, the fibre bundle was again exposed to a water pressure of 0.3 MPa. The potting was tested in this manner over several cycles. The number of cycles at the time of individual testing increased with the increasing success of previous pressure tests. Table 3 shows the results of the tested fibre bundle.

The same procedure was used for testing the tightness of the pottings at a high water temperature in a water bath into which the bundle was immersed after the test. The results showed that the potting's exhibited leakage at a temperature above 52 °C.

4 MEASUREMENT OF PRESSURE LOSS FIBRE BUNDLES

The pressure drop was measured on six selected fibre bundles. Three fibre bundles consisted of transparent fibres and the other three with porous ones. Potting tightness before the measurement was 100 %. All parameters of the tested bundles (outer diameter, number of fibres in a bundle, and their length) were identical. A source of the pressurized water was represented by a pressurized water supply network with a pressure of 0.45 MPa and a temperature of 18 °C. The fibre bundle was connected to the rubber hoses via an inlet (4) and an output potting (5) (Fig. 7).

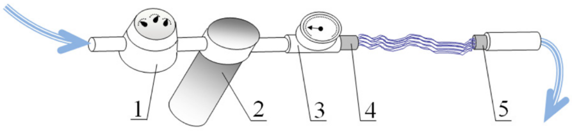

Fig. 7. *Schematic diagram of a fibre bundle during the measurement of a pressure loss*

The water flowed into the bundle through a flow metre (1) and a water filter (2). Water pressure was measured with a type PM 03.05 pressure gauge (3), with an amplitude between 0 MPa and 0.6 MPa and with an accuracy of ± 0.3 %. Fig. 8 shows the dependency of the pressure loss and water flow through the fibre bundle. The bundles of transparent fibres (t1 to t3) and bundles of porous fibres (p1 to p3) show an almost linear progression of the change in a pressure drop in the flow rate.

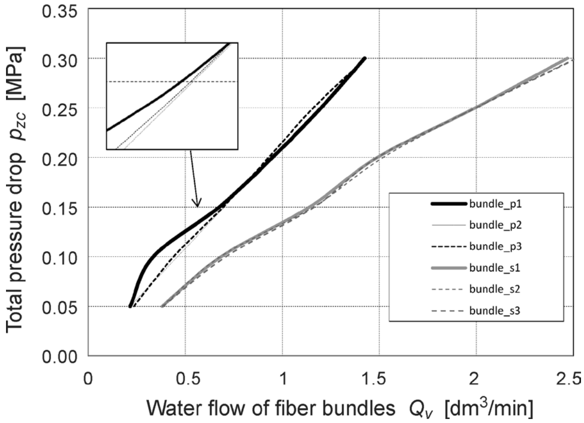

Fig. 8. *Pressure drop fibre*

5 MEASUREMENT OF TEMPERATURE AND FLOW

An experiment with an integrated bundle of transparent polypropylene capillaries was conducted on a heat exchanger that was constructed in a counter-current wiring with a tangential inlet of the secondary medium (Fig. 9).

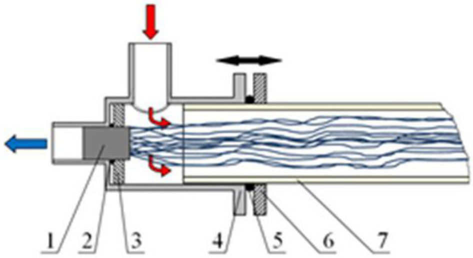

Fig. 9. *Heat exchanger with a tangential inlet and sliding head*

Table 3. *Integrity test – measurements results*

test number	Interval between individual tests [h]	Q_V [dm³·min⁻¹]	p [MPa]	t_i [°C]	l [m]	n_c [l]	t_w [°C]
basic test	–	1.61	0.3	19.2	0.726	–	–
2	18	1.61	0.3	19.1	0.724	3	52
3	15	1.58	0.3	18.8	0.722	13	52
4	151	1.63	0.3	18.3	0.720	13	52
5	151	1.66	0.3	18.1	0.716	18	52

Note: n_c the number of reheating cycles of the bundle and its subsequent re-cooling down, l bundle length, p pressure of water in the fibres during the test, t_i temperature of the test water in the capillaries before the test, t_w the temperature of the water in which the bundle was submerged.

The construction of the shell of heat exchanger allowed the release of fibres in a range from 0 % to 10 %. The exchanger has been studied for the impact of the fibres' tension on the intensity of the heat transport. A sliding head (4) placed on the shell of the heat exchanger (7) together with a rubber seal (5) and a thrustwasher (6) were used for this purpose. The potting of the investigated bundle itself (1) was sealed using a so-called O-ring (2) and pressed with a washer (3).

The experiment used three different versions of a fibre bundle. Each version had a different number of fibres, different outer fibre diameter and a variety of tensions. The parameters of the heat exchangers are shown in Table 4.

At zero tension, the fibre is at 100 % of its length, and the fibre axis is a straight line. When released, the bundle changes the distance between the clamping of the pottings; the fibre length remains constant. The bundle release Δl_u [%], expressed as a percentage of the total length of the fibres, is described by Eq. (1):

$$\Delta l_u = 100 - \frac{(l_z - \Delta_l)\cdot 100}{l_z}. \qquad (1)$$

Given the diameter and the size of fibres, the release of individual bundles was chosen as per Table 5.

View of the experimental stand is shown in Fig. 10.

Table 4. *Parameters of used bundles*

Type of a bundle	Number of fibres [pc]	Outer diameter [mm]	Fibre length [m]	Heat transfer area [m²]
A	400	0.65	0.71	0.580
B	900	0.35	0.70	0.682
C	1385	0.275	0.70	0.834

Table 5. *Release values for different types of bundles*

Type of a bundle		Δl_u [%]	
A	0	0.7	1.4
B	0	1.5	3
C	0	1.4	3.7

During the experiment, the temperatures were measured at the inlet and outlet of the primary and secondary circuits of the heat exchanger as well as the water flow through the fibres. The measured data was to define the overall heat transfer coefficient k (W·m^{-2}·K^{-1}) in accordance with Eq. (2):

$$k = \frac{P}{S \cdot \Delta T_{\ln}}, \qquad (2)$$

where S is the total heat exchanger area of the bundle of fibres [m²], P is the heat transfer rate of the exchanger [W] and $\Delta T_{\ln}$ is the logarithmic mean temperature difference (LMTD) [K].

Fig. 10. *Heat exchanger with tangential inlet and sliding head*

The heat exchanger's performance is determined from the heated water in the secondary branch, i.e. in fibres. This medium herein is indicated with an index 2. Eq. (3) is valid:

$$P = Q_{m2} \cdot c_p \cdot \left(T_2'' - T_2'\right). \qquad (3)$$

The mean temperature logarithmic gradient is calculated from the Eq. (4):

$$\Delta T_{\ln} = \frac{\Delta T_0 - \Delta T_S}{\ln \dfrac{\Delta T_0}{\Delta T_S}}. \qquad (4)$$

At the counterflow heat exchanger, the individual differences of temperatures are determined from the Eqs. (5) and (6):

$$\Delta T_0 = T_1' - T_2'', \qquad (5)$$

$$\Delta T_S = T_1'' - T_2', \qquad (6)$$

where index 1 is the primary medium; one bar represents the incoming temperature and two bars the outgoing temperature of the medium [K].

6 DISCUSSION

Bundle type A was characterized by a large outer diameter of fibres (0.65 mm) and the fibres were relatively solid. When released by 0.7 %, the fibres were evenly deployed over the cross section and they were washed thoroughly. When released by 1.4 %, the fibres already touched the wall of the heat exchanger, which resulted in a decrease in the overall heat transfer coefficient. The course of the factor *k* according to the flow rate of the fibre bundle (bundle A) is shown in Fig. 11.

The course of the heat transfer coefficient for bundle B is shown in Fig. 12 and for bundle C in Fig. 13.

In all three bundle types, the smallest overall heat transfer coefficient values were obtained at 0 % release.

In a larger flow cross-section of fibres, higher overall heat transfer coefficients are reached when releasing a bundle up to circa 1 %. In smaller flow cross-sections of fibres, a greater release is more suitable (over 3 %). For example, with a flow of 100 $dm^3 \cdot h^{-1}$ and approximately the same bundle release (1.4 % to 1.5 %), a greater overall heat transfer coefficient value is shown by a B-type bundle (circa 590 $W \cdot m^{-2} \cdot K^{-1}$). With the same flow, bundles A and C reach value *k* of circa 420 $W \cdot m^{-2} \cdot K^{-1}$.

In terms of evaluating the influence of measurement inaccuracies upon the results obtained, the following can be stated. The measured values included temperature, flow and pressure. The instruments that were used for measuring the stated values caused a so-called primary inaccuracy. A secondary inaccuracy resulted from the measurement of individual values of the given parameters due to the instruments used. A so-called tertiary inaccuracy should show what influence a particular parameter has upon the calculated value, i.e. upon overall heat transfer coefficient *k*.

If, in Eq. (2), we take into account the Eqs. (3) and (4), for overall heat transfer coefficient *k* we obtain an equation in the shape:

$$k = \frac{Q_{m2} \cdot c_p \cdot \left(T_2'' - T_2'\right)}{S \cdot \left[\left(T_1' - T_2''\right) - \left(T_1'' - T_2'\right)\right]} \cdot \ln \frac{\left(T_1' - T_2''\right)}{\left(T_1'' - T_2'\right)}. \qquad (7)$$

The equation shows that the *k* value is influenced by an inaccuracy in measuring temperature and flow.

The development of a percentage deviation (error) in the final value of overall heat transfer coefficient *k* depend on the measurement error of the given parameters (each individually) is shown in

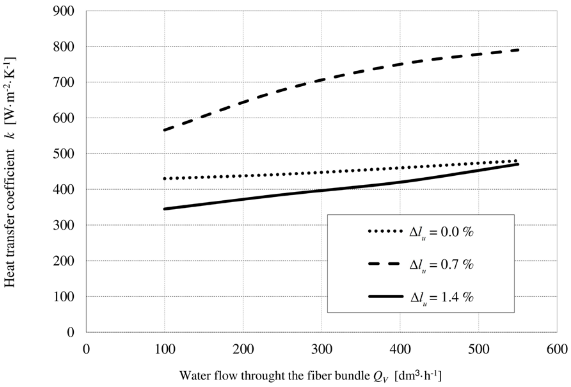

Fig. 11. Overall heat transfer coefficient for bundle type A

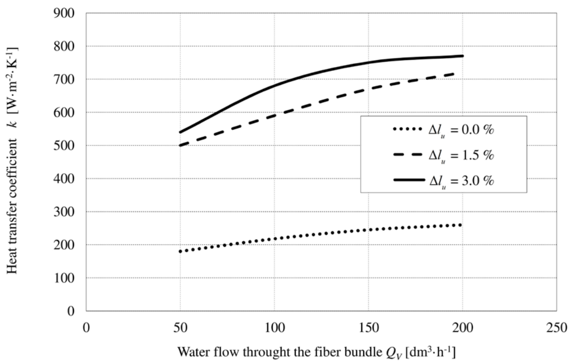

Fig. 12. *Overall heat transfer coefficient for bundle type B*

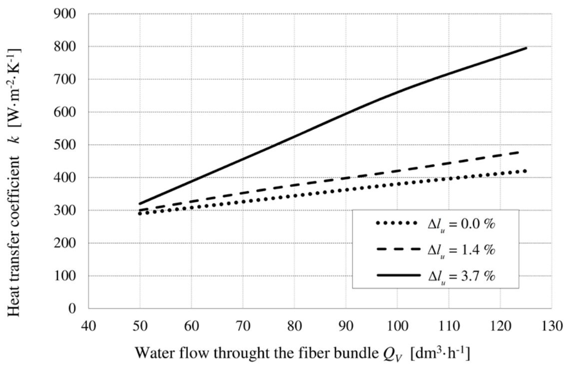

Fig. 13. *Overall heat transfer coefficient for the bundle type C*

Fig. 14 on the vertical axis. The horizontal axis shows the measurement error for the appropriate temperature and flow. The diagram shows a strong dependence of the overall heat transfer coefficient *k* upon the temperature of outlet water from the exchanger T_2'' and flow Q_{m2} and relatively weaker dependence upon temperatures T_1', T_1'' and T_2'.

In order to achieve the required accuracy when determining the overall heat transfer coefficient at a level of 3 %, thermal sensors with an accuracy of

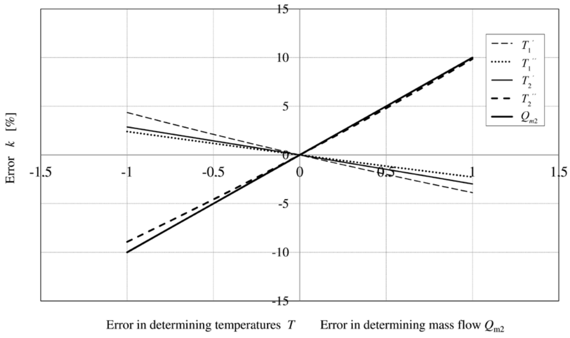

Fig. 14. *The influence of inaccuracies in measured values upon the heat transfer coefficient*

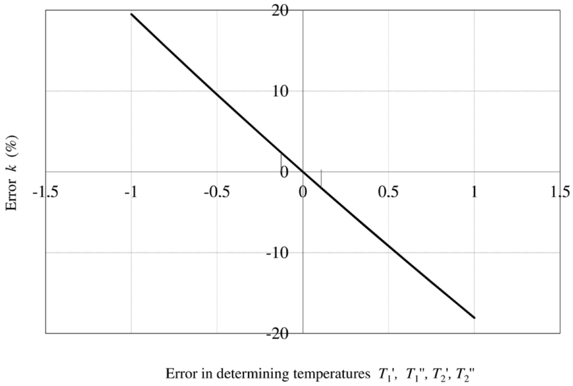

Fig. 15. *Overall heat transfer coefficient error depending upon the measured temperature*

±0.1 °C must be used. This can be seen in Fig. 15 where there is a visible influence of deviations of the red values of all temperatures upon the k value. For example, if temperature T_2'' were read with an inaccuracy of +0.5 °C and other temperatures with an inaccuracy of –0.5 °C, the resulting deviation in the overall heat transfer coefficient k would be as much as ±10 %.

7 CONCLUSIONS

Examination of the heat exchangers made of polypropylene fibres showed that one of the fundamental problems in their application is the tightness of fibres in the potting. It has been established that at a water temperature above 52 °C, it is very difficult to ensure a leak-proof performance of the exchanger.

It is clear from the above that heat exchangers made of polypropylene fibres may only achieve faultless operation up to 50 ºC. Above this temperature, a breakdown in potting occurs, since it consists of three varying materials (metal, adhesive, polypropylene) whose change in shape depending upon temperature is expressed in different ways (each material has different thermal conductivity).

At the same time, measurements confirmed that a heat exchanger using fibres of a certain degree of release have a better performance in comparison to a design where fibres are under tension. To a certain degree, this result is related to the slight movement of the fibres along the cross-section which, at a certain release of fibre tension, causes a more intensive exchange of heat between the primary and secondary medium.

Testing the tightness of pottings took place at a pressure of 0.3 MPa. This pressure represents a sufficient reserve during application of the given exchangers in real operation when using low potential heat from waste water.

Finally, it is important to emphasize that the use of the heat exchangers of the polypropylene fibres is limited by the thermal, pressure, or strength resistance, respectively.

8 ACKNOWLEDGEMENTS

This paper was written with the financial support of Project VEGA No.1/0004/14 and SP2016/110-FMMI at Technical University of Ostrava.

9 NOMENCLATURES

l_z is the length of the bundle without tension, [m]
Δl_z the size of release, [m]
S the total heat exchange area of given fibre bundle, [m^2]
P heat transfer rate, [W]
ΔT_{ln} logarithmic mean temperature difference, [K]
Q_{m2} mass flow, [kg·s^{-1}]
c_p mean specific heat capacity, [J·kg^{-1}·K^{-1}]
T_2' incoming water temperature, [K]
T_2'' temperature of the exiting water, [K]
ΔT_0 temperature difference between the primary and the secondary medium at the beginning of the exchanger, [K]
ΔT_S similar difference but at the end of the exchanger, [K]

10 REFERENCES

[1] Brestovič, T., Čarnogurská, M., Příhoda, M., Kubík, M. (2015). Simulation of heat transport at the cooling of the sugar solution in a recuperation exchanger. *Acta Polytechnica*, vol. 55, no. 3, p. 140-145. **DOI:10.14311/AP.2015.55.0140**.

[2] Duransky, P., Papucik, S., Jandacka, J., Holubcik M., Nosek, R. (2014). Design of heat exchanger for Ericsson-Brayton piston engine. *The Scientific World Journal*, p. 1-6, Art. ID 138254, **DOI:10.1155/2014/138254**.

[3] Čarnogurská, M., Příhoda, M., Širillová, Ľ. (2014). Power losses and the efficiency of industrially used gearboxes. *AIP Conference Proceedings*, vol. 1608, p. 16-21, **DOI:10.1063/1.4892699**.

[4] Stritih, U., Bombač, A. (2014). Description and analysis of adsorption heat storage device. *Strojniški vestnik - Journal of Mechanical Engineering*, vol. 60, no. 10, p. 619-628. **DOI:10.5545/sv-jme.2014.1814**.

[5] Čarnogurská, M., Příhoda, M., Popčáková, D. (2010). Modelling the flow conditions in the tunnel and its reduced model. *Journal of Mechanical Science and Technology*, vol. 24, no. 12, p. 2479-2486, **DOI:10.1007/s12206-010-0810-9**.

[6] Honus, S., Němček, O, Juchelková, D. (2013). The analysis of the heat transfer into reactor walls in the thermal system and the verification. *Advanced Materials Research*, vols. 694-697, p. 771-777, **DOI:10.4028/www.scientific.net/AMR.694-697.771**.

[7] Příhoda, M., Rédr, M. (1998). *Heat Transfer and Fluid Mechanics*. VŠB-TU Ostrava, Ostrava. (in Czech)

[8] Vahidinia, F., Miri, M. (2015). Numerical study of the effect of the Reynolds numbers on thermal and hydrodynamic parameters of turbulent flow mixed convection heat transfer in an inclined tube. *Strojniški vestnik - Journal of Mechanical Engineering*. vol. 61, no. 11, p. 669-679, **DOI:10.5545/sv-jme.2015.2818**.

[9] Lienhard IV. J.H., Lienhard V. J.H. (2012). *A Heat Transfer Textbook*. 4th ed. Phlogiston Press, Cambridge.

[10] Jones, J.B., Hawkins, G.A. (1986). *Engineering Thermodynamics*, John Wiley, New York.

[11] Zaheed, L., Jachuck, R.J.J. (2004). Review of polymer compact heat exchangers, with special emphasis on a polymer film unit. *Applied Thermal Engineering*, vol. 24, no. 16, p. 2323-2358, **DOI:10.1016/j.applthermaleng.2004.03.018**.

[12] Zarkadas, D.M., Sirkar K.K. (2004). Polymeric hollow fiber heat exchangers: An alternative for lower temperature applications. *Industrial & Engineering Chemistry Research*, vol. 43, no. 25, p. 8093-8106, **DOI:10.1021/ie040143k**.

[13] Raudensky, M., Dohnal, M. (2012). Large scale capillary based plastic heat exchangers. *Chemical Engineering Transactions*, vol. 29, p. 1477-1482, **DOI:10.3303/CET1229247**.

[14] Dohnal, M., Vesely, T., Raudensky, M. (2012). Low cost membrane contactors based on hollow fibres. *EPJ Web of Conferences*, vol. 25, p. 1-10, **DOI:10.1051/epjconf/20122501009**.

[15] Raudensky, M., Dohnal, M. (2015). Fouling of polymeric hollow fiber heat exchanger by wastewater. *Chemical Engineering Transactions*, vol. 45, p. 949-951, **DOI:10.3303/CET1545159**.

[16] Pohl, S., Madzgalla, M., Manz, W., Bart, H.J. (2015). Biofouling on polymeric heat exchanger surfaces with E. coli and native biofilms. *The Journal of Bioadhesion and Biofilm Research*, vol. 31, no. 9-10, p. 669-707, **DOI:10.1080/08927014.2015.1094691**.

[17] Chen, Z.F. (2011). Application prospect of plastic heat exchanger in sewage source heat pump systems. *International Conference on Management Science and Industrial Engineering*, p. 1184–1187, **DOI:10.1109/MSIE.2011.5707631**.

[18] Wicaksana, F., Fane, A.G., Chen, V. (2006). Fibre movement induced by bubbling using submerged hollow fibre membranes. *Journal of Membrane Science*, vol. 271, no. 1-2, p. 186-195, **DOI:10.1016/j.memsci.2005.07.024**.

[19] Oshman, Ch., Li, Q., Liew, L.A., Yang, R., Bright, V.M., Lee, Y.C. (2013). Flat flexible polymer heat pipes. *Journal of Micromechanics and Microengineering*, vol. 23, art. 015001, **DOI:10.1088/0960-1317/23/1/015001**.

[20] Astrouski, I., Raudensky, M., Dohnal, M. (2013). Particulate fouling of polymeric hollow fiber heat exchanger. *International Conference on Heat Exchanger Fouling and Cleaning,* Budapest, p. 233-239.

[21] Wikipedia (2015). from *http://goo.gl/tqBofN* accessed on 2015-11-15.

Strojniški vestnik - Journal of Mechanical Engineering 62(2016)6, 389-397

DOI:10.5545/sv-jme.2016.3470
Original Scientific Paper
Received for review: 2016-02-01
Received revised form: 2016-03-15
Accepted for publication: 2016-03-30

Do Organisational Innovations Have Impact on Launching New Products on the Market?

Rolando Koren[1] – Jasna Prester[2] – Borut Buchmeister[1] – Iztok Palčič[1,*]
[1] University of Maribor, Faculty of Mechanical Engineering, Slovenia
[2] University of Zagreb, Faculty of Economics and Business, Croatia

The main purpose of this paper is to define which organisational innovation concepts have the more significant impacts when launching new products on the market. We present an overview of 22 organisational innovative concepts used in Slovenian manufacturing companies. The results are based on data from a sample of 89 manufacturing companies, obtained within a European manufacturing survey (EMS). A detailed analysis based on correlation and regression analysis was performed on more frequently used organisational innovative concepts, where we found interdependence between these concepts. There were significant correlations between organisational innovation concepts such as total quality management (TQM) and total productive maintenance (TPM); task integration and total productive maintenance; methods for continuous improvement (CIP) and total productive maintenance. We also found out that the more complex is the product the use of the majority of organisational innovation concepts has a greater impact. The results showed that the use of selected organisational innovative concepts had a positive impact on launching new products on the market. Multiple regression analysis and correlation analysis showed that the organisational innovative concept TQM, task integration, ISO 9000 and CIP had a significant positive impact on launching new products on the market.
Keywords: innovation, organisational innovation, new products, market, survey research

Highlights
- *The impact of organisational innovative concepts was researched when launching new products on the market.*
- *Interdependence is presented between the more frequently used organisational innovative concepts in the Slovenian manufacturing industries.*
- *Interdependence is presented between the more frequently used organisational innovative concepts and launching new products on the market.*
- *Results present the impact of individual organisational innovative concepts on launching new products on the market.*
- *Research was based on a sample of 89 Slovenian manufacturing companies, the data of which were obtained through a European manufacturing survey.*

0 INTRODUCTION

Innovations have always been considered as important drivers of economic progress and civilisation in general [1]. Companies that do not invest in innovation are entering into their future with a risk of losing their market share. With no innovative thinking companies decline, which certainly reduces their innovative potentials, competitiveness and, consequently, the likelihood for future business success [2]. Therefore, companies have to constantly explore, invent, innovate and create new values, which will ensure the existence and further development [3]. The term "innovation" is still extremely popular. The more common innovations are associated with research and development (R&D) activities of a new product's development. Numerous studies have proved that increasing investment in R&D activities leads to innovative products, which enables companies to achieve competitive advantages and greater market shares [4] and [5]. The introduction of new practices into business systems is important for companies in their quests to upgrade their productivity, improve service quality and maintain competitiveness [6].

There are several types of definitions and classifications of innovation. In the earlier 20-th century Schumpeter described different types of innovation, namely: new products, new methods of production, new resources, research of new markets and new ways of organising production and operations [7]. Among numerous classifications of innovative types, one of the more commonly accepted definitions [8] which distinguishes four types of innovation: product innovation, process innovation, marketing innovation, and organisational innovation (OI). OIs are emerging approaches, as they were not recognised as innovations until qualified as such in [8]. According to Camisón and Villar-López [9], OIs currently represent one of the more important and sustainable sources of competitive advantages for businesses but they have not been sufficiently studied, nor has been their impacts on the innovative and financial effects of companies. Read [10] defines OIs as multidisciplinary areas of research; they are dynamic and iterative

*Corr. Author's Address: University of Maribor, Faculty of Mechanical Engineering, Smetanova ulica 17, 2000 Maribor, iztok.palcic@um.si

processes of creating, developing, and producing products, services, processes or policies that are new to organisations.

The paper deals with the analysis of OI concepts and their impacts on launching new products on the market. We present the frequent uses of 22 OIs in manufacturing companies. We also present characteristics of companies' products in terms of their complexities and their relationships with the more frequently used OIs. Given that today innovations are a key competitive tool [11], the aim is to identify those OIs that have the greatest impact on launching new products on the market. Regression and correlation analysis were performed to evaluate how the more frequently used OIs influence each other. Regression analysis shows how each individual OI concept affects the launching new products on the market as the dependent variable.

1 LITERATURE REVIEW

Hong et al. [12], who have studied how our understanding of innovation has developed over the past few decades, say that understanding innovation and the role of innovation in business systems greatly evolved over the years. Gunday et al. [13] claim that innovativeness is one of the fundamental instruments of growth strategies to enter new markets, to increase existing market share and to provide a company with a competitive edge. Mumford argues that with rapid changes in technology, and global competition, the success of many organisations has become more dependent on their abilities to bring innovative products to market [14].

Today, innovations are regarded as a multidimensional issue that can be addressed within several contexts. Keupp et al. [15] made an extensive literature review on innovation management, where when analysing more than 342 papers, they found that there were a low number of papers dealing with the field of non-technical innovation, while the number of papers in the field of product innovation was very high. Camisón and Villar-López [16] also argue that the majority of research on innovation followed a technical focus, concentrating more on product development. Similarly, they concluded that OIs are not researched enough and that their impact on innovation and financial results are not obvious. Armbruster et al. [17] and Palcic et al. [18] claimed that non-technical innovations play an increasingly important role in a better understanding of innovation and its impact on the competitiveness of companies. They also emphasise that the existing literature on OI is diverse and dispersed or does not yet exist.

There are many definitions on OI and sometimes in the literature they can be found as administrative innovation [19] and [20]. Damanpour and Aravind [21] undertook a major study in which they defined OI as the use of new management and business concepts and practices. They showed an overlap of administrative, organisational and managerial innovations. Currently the most accepted definition is the OECD version, which defines OI as the implementation of a new organisational method within a company's business practices, workplace organisation or external relations. The distinguishing features of OI compared to other organisational changes in a company is the implementation of an organisational method (in business practices, workplace organisation or external relations) that has not been used before in the company, usually suggested or enforced by upper management. OI has a tendency to increase company performance by reducing administrative and transaction costs, improving work-place satisfaction (and thus labour productivity), gaining access to non-tradable assets (such as non-codified external knowledge) or reducing costs of supplies. An example would be an introduction of practices for codifying knowledge by establishing databases of best practices, solutions and other codified knowledge. This knowledge is thus more easily accessible to others in the company. Another example might be introduction of training programme for employee developments, improved employee retention by better working conditions, or the initiation of supplier development programmes [8].

Crossan and Apaydin [22] concluded on the basis of a comprehensive meta-analysis that the papers on the topic of OI are narrowly focused. Different groups of OI concepts lead to different objectives. The current literature does not specify which OI contributes to which sources of competitiveness and measures of competitiveness. Perhaps that is one of the reasons why scholars neglect OI as the success of the innovative process is rather difficult to measure. Wright et al. [23] went even further and claimed that managerial and organisational innovations are not really innovations and can be in fact highly standardised. According to Jin et al. [24] only a few studies have examined the relationship between innovative types and company performance, especially within the field of OI. However Gunday et al. [13] proved that teamwork and quality management systems, which fall within the domain of organisational work, ultimately lead to higher financial performance.

Delarue et al. [25] came to similar conclusions and showed that teamwork improves organisational performance. Jiménez-Jiménez and Sanz-Valle [26] proved that organisational learning (which falls into the domain of human resources management) does in fact lead to greater innovation and business performance. Bolivar-Ramos et al. [27] showed that organisational learning and OI, as competencies and strategic capabilities, can have positive effects on improving organisational performance. Mol and Birkinshaw [6] found that management innovation (another term for OI) is positively associated with company performance in the form of subsequent productivity growth. Evangelista and Vezzani [28] proposed a model showing that OI influences sources of competitiveness such as product performance and efficiency, ultimately leading to higher market share and financial results. However, they tested correlations between sources of innovation rather than testing OI on sources of competitiveness. Laforet [29] found that OI usage results in enhanced productivity, margin, market leadership, and working environments but does not lead to operational efficiency and employees' retention. Hamel [30] argued that OI should have a positive impact on competitive advantage. Prester and Bozac [20] found that usage of some organisational practices, such as interdisciplinary teams, quality circles, system for collection of employees' proposals, planned job rotation, significantly lead to innovation.

As we found very few studies on how OIs are interrelated with new product development [11] and [24], we investigated the more frequently used OI practices in Slovenian manufacturing companies and examined if they had an impact on launching new products on the market.

2 METHODOLOGY

Survey method research was used for collecting data in this study. The data was obtained within the largest European research on manufacturing activities, the European manufacturing survey (EMS). The coordinator of the project is the Fraunhofer ISI Institute from Germany. EMS covers indicators within the areas of technical and organisational innovation, relocating of production, energy issues, human resource issues etc. It also covers the future competitive priorities of the company, characteristics of the production process and the characteristics of the company's core product, and innovation issues measured in terms of generated profits by significantly improved products that are new to the company and new products that are new to the market. The target group are companies from the manufacturing sector with more than 20 employees. The first EMS survey in Slovenia was carried out in 2004. It was repeated in the years 2007, 2010 and 2013. The questionnaire has 20 sections and it is eight pages long.

The study includes 22 OI concepts, divided into 4 groups: Organisation of production (6), Organisation of work (5), Standardisation and conformity assessment (6), and Human resource management (5). Companies had to reveal information about the degree of OI use in terms as low use (first contact with the concept), medium use (partial use of the concept) and high use (full application of the concept – at least 70 % of employees are involved in the OI concept).

In 2012 791 questionnaires were sent out and 89 responses were returned, representing 11.25 % response rate. Companies that completed the questionnaire in 2013 were 29.2 % small companies, 44.9 % medium-sized and 25.8 % large companies in terms of the number of employees.

Product complexity was divided into simple products, medium-complex products (e.g. pumps, several parts and technologies using simple assembly) and complex products (machines or manufacturing systems). The results showed that the majority of companies (around 52 %) manufactured medium-complex products. A little over a third of companies (36 %) produced complex products and the remaining companies produced simple products. This analysis started with descriptive statistics in which the results of usage of OI were shown, followed by correlation and regression analysis where the interactions between individual groups of OI concepts and new products were analysed.

3 RESULTS AND DISCUSSION

3.1 Organisational Innovative Concepts Use

Descriptive statistics are shown in Table 1. Companies were asked which of the selected OI concepts were they using and when it was first introduced. If they are not using a specific OI concept, they were asked if they were considering implementing it in the next three years. Among the top 10 more frequently used OI concepts we found five concepts from the "Organisation of the work" group. Two OI concepts from the "Organisation of production" group and two OI concepts from the "Human resources management" group from among the more frequently used concepts and only one OI concept from the "Standardisation and assessment" group. Teamwork in production and assembly was considered as the more widespread

Table 1. *Usages of OI in Slovenian manufacturing companies*

Organisational concepts		Fist introduction (on average)	Share [%]	Rank	Share of use until 2015 [%]
Organisation of production	Value Stream Mapping	2007	13.5	19	10.1
	Customer-oriented cell / line	2002	28.1	11	3.4
	Zero stock principle	2005	27.0	12	7.9
	Single-minute exchange of die (SMED)	2003	19.1	14	4.5
	Total Productive Maintenance (TPM)	2003	49.4	6	5.6
	Total Quality Management (TQM)	2002	40.4	8	10.1
Organisation of work	Method of 5S	2004	52.8	4	5.6
	Standardised work instructions	2000	77.5	2	3.4
	Task integration	2001	40.4	8	3.4
	Met. for cont. process improvement (CIP)	2004	43.8	7	3.4
	Teamwork in production and assembly	2000	78.7	1	2.2
Standardisation and assessment	Visual display of process and equip. status	2005	25.8	13	4.5
	ISO 9000 and other	2000	77.5	2	4.5
	6 Sigma	2007	14.6	18	6.7
	ISO 14001	2004	16.9	17	9.0
	ISO 50001: 2011	2009	2.2	21	6.7
	Total cost of ownership (TCO)	2008	5.6	20	7.9
Management of human resources	Formalized workshops to generate ideas	2003	34.8	11	4.5
	Instruments for retention of knowledge	2000	18.0	15	9.0
	Part-time dedicated to creativity	2005	18.0	15	5.6
	Program of staff development	2004	39.3	10	9.0
	Training to enhance creativity	2002	52.8	4	5.6

method of organising work, as more than 78 % of Slovenian manufacturing companies used it. The only other two OI concepts with high shares of use were standardised work instructions and implementation of ISO 9000 standards; both of them being present in more than 77 % of manufacturing companies.

It is worth mentioning two more concepts, which are implemented in more than half of Slovenian manufacturing companies namely the concept of the method of 5S (52.8 %) from the “Work organisation” group and concept training to enhance creativity (52.8 %) from the “Human resource management” group. The other OI concepts are implemented in less than 50 % of Slovenian manufacturing companies. As we can see in Table 1, Slovenian manufacturing companies have been using OI concepts for quite some time and they are not something new for the companies. This is in line with the findings of several authors [23] and [31] to [33] that OI in the business environment have been present for a long time.

For further analysis we have selected OI concepts used in at least 30 % of companies, meaning that we only selected 10 of the more frequently used OI concepts. Firstly, we have looked at degree of using the selected OI. The analysis shows that only the ISO 9000 concept is highly used in more than 50 % of the manufacturing companies. Only one tenth of the companies considered the use of ISO 9000 concept as low. The share of all other highly used OI concepts in companies is less than 50 %, where the medium use of OI is more dominant ranging from 38 % to 62 %. The lowest shares of the highly used concepts are linked to the management of human resources (staff development programmes 22.9 % and training of employees 12.8 %).

3.2 Organisational innovative Concepts, Product Complexity and New Product Launching

We also analysed how product complexity depends on the frequency of use of the 10 more widely used OIs. Fig. 1 presents the average shares of selected OI concepts – lower black bar within each OI. The three bars above it represent the share of products based on their complexities within companies that had implemented specific OI (complex, medium complex and simple products). For example, teamwork in production and assembly was considered as the most widespread OI concept, as more than 78 % of companies were using it. Fig. 1 shows that 43.3 % companies with implemented teamwork concept in production and assembly produce complex products.

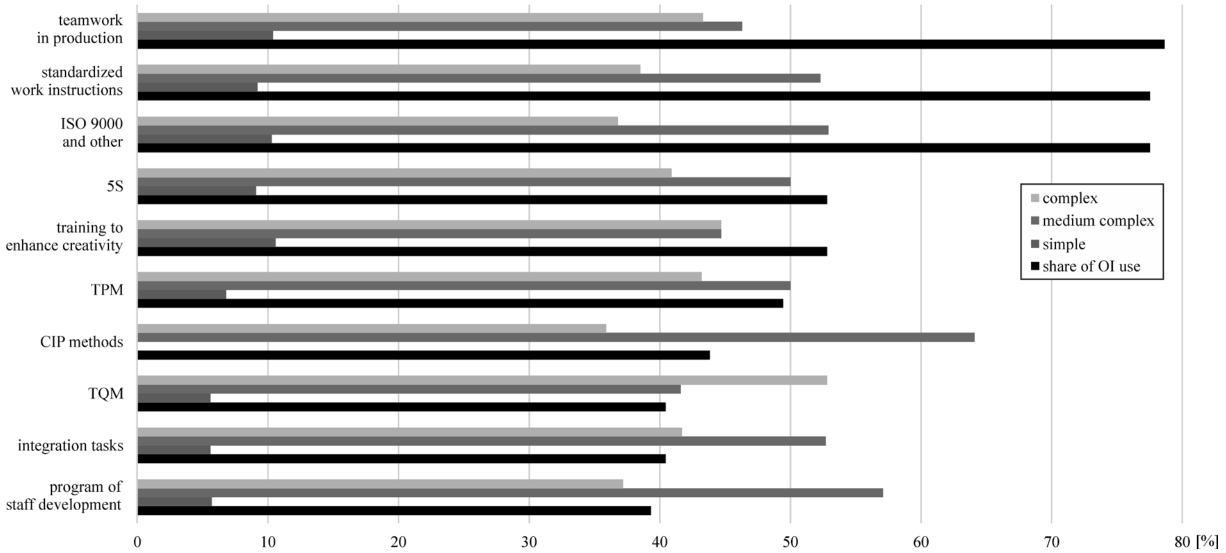

Fig. 1. *Characteristic of the product complexity depending on the level of use for the 10 most widely used OI*

The share of medium-complex products was 46.3 %, while the share of simple products was 10.4 %. It has already been mentioned that on average 36 % of manufacturing companies produced complex products and 52 % medium complex products. Fig. 1 shows that the share of complex products in companies that implemented analysed OI concepts was higher than usual (36 %) for the majority of OI concepts.

The highest share of complex products (52.8 %) was produced by companies, with OI concept TQM implemented within their operating systems. They are followed by companies with the implemented concept of training to enhance creativity (44.7 %). Surprisingly, in the penultimate place was the OI concept ISO 9000 and other standards (36.8 %) which were ranked as second in the share of use of the concept in companies. We can assume that the standardisation of systems does not affect the complexities of the products that companies produce. On the other hand, we can observe that the share of simple products was lower within companies that use selected OI concepts – the average share in general was 12 %. Share of simple products is especially low in companies that implemented TPM, TQM, integration of tasks, and programmes of staff development. The most interesting was the CIP concept – companies with this OI concept implemented do not produce simple products and where medium complex products were prevalent with almost 65 %. Therefore, it can be concluded that the more complex was the product, selected OI have greater impact.

In the period from 2009 until 2012, 61.8 % of Slovenian manufacturing companies had launched a new or significantly improved product on the market, while 22.5 % of companies had introduced radically new products – products that were also new for the market.

Fig. 2 shows the 10 more frequently used OI concepts and their effects on the introductions of new products on the market. On average companies that implemented OI concepts, achieved a higher share of new products launched on the market. The exceptions are two OI concepts namely, method 5S and training to enhance creativity, where it can be seen that implementation of these two concepts did not have a specific impact on the introduction of new products on the market.

The biggest difference in the launch of new products on the market (if concepts are introduced and used), can be observed in the use of TQM, task integration and ISO 9000 and other standards. 86 % of companies that implemented TQM in the period from 2009 until 2012 have launched new products on the market. According to the results presented in Fig. 1 it can be concluded that a significant number of new products were in fact complex product launches. By contrast, in the same period only 45 % of companies that did not use TQM launched new products on the market. If companies used task integration on average 81 % of them launched new products on the market. Only 49 % of companies that do not use task integration launched a new product. In the case of ISO 9000, 68 % of companies that used ISO 9000

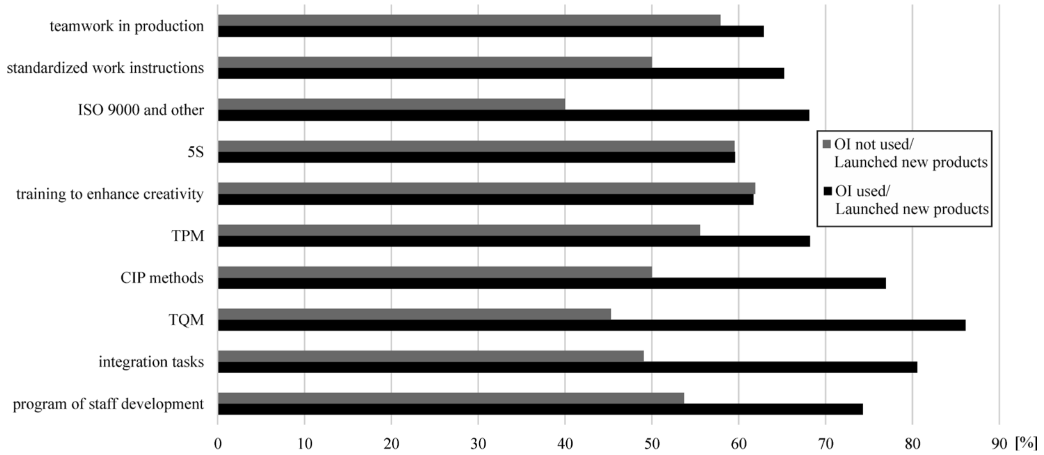

Fig. 2. *Share of launched products on the market in relation to the use of the OI*

launched a new product on the market but only 40 % of companies that do not use this concept.

Even though we can observe the difference regarding the launch of new products between companies that have implemented OI concepts and those that did not (Fig. 2), we tested whether there was a statistically significant difference. The test showed a statistically significant difference at P-value of 0.05. Next the correlation analysis between 10 OI concepts was performed to see how they affected each other (Table 2). The analysis showed that some concepts were complementary to each other. There was a high significant correlation between TQM, task integration, CIP and TPM. Investing in TQM, task integration, CIP will lead to higher usage of TPM. An increase in investment in task integration will have a positive impact on TPM, standardised and detailed work instruction teamwork in production, and ISO 9000. So if we invest into forming such a set of OI practices, we can expect enhancements in the mentioned areas. There was a very high correlation between TQM and task integration. This can be explained by the fact that TQM uses quality circles, where employees in the circles perform more tasks, motivating them to see the whole process of the work that can ultimately lead to more innovation. There is also a high correlation between OI concepts ISO 9000 and TPM. This is due to the fact that ISO standards require that all processes in the company are written and accurate. As ISO standards have to be renewed every three years that forces companies to comply with ISO prescriptions and one of them is regularly checking the equipment. Concept employee training for creativity and innovation has a positive impact on concept standardised and detailed work instructions. With newly acquired skills, workers introduce

Table 2. *Correlations between the 10 more widely used OI concepts in Slovenian manufacture companies*

	Team-work	ISO 9000	SDWI	5S	ETCI	TPM	CIP	TI	TQM	TDP
Teamwork in production	1									
ISO 9000 and other standards	0.017	1								
Standardised and detailed work instruction (SDWI)	**0.319	**0.277	1							
Method of 5S	0.189	0.129	**0.390	1						
Employee training for creativity and innovation (ETCI)	*0.278	*0.274	**0.303	*0.224	1					
Total Productive Maintenance (TPM)	*0.255	**0.405	**0.336	**0.361	*0.232	1				
Methods for continuous improvement process (CIP)	**0.342	*0.267	*0.246	0.185	0.112	**0.404	1			
Task integration (TI)	**0.312	**0.291	**0.390	*0.217	0.198	**0.466	**0.314	1		
Total Quality Management (TQM)	0.192	**0.324	*0.272	0.197	0.180	**0.624	**0.342	**0.493	1	
Talent development program (TDP)	0.120	*0.270	**0.317	*0.234	*0.270	**0.331	*0.230	**0.325	**0.303	1

* Correlation is significant at the 0.05 level (2-tailed); ** Correlation is significant at the 0.01 level (2 tailed).

Table 3. *Correlations between 10 OI concepts and new products launches*

Correlations	New products
Total Quality Management TQM	**0.380
Task integration	**0.374
ISO 9000 and others	**0.313
Methods for CIP	**0.289
Talent development program	*0.242
Standardised and detailed work instruction	0.206
Total Productive Maintenance TPM	0.156
Teamwork in production	0.119
Method of 5S	0.045
Employee training for creativity and innovation	–0.042

innovations to their work environment; consequently, the work instructions will be changed and thus indirectly improves business results.

Finally, we investigated the impacts of the 10 more frequently used OI when launching new products on the market (Table 3). The results show that there are four very dominant and significant OI concepts (significant value is 0.01 or less), which have a positive impact on launching new products on the market. These concepts are: TQM, task integration, ISO 9000 and CIP. Statistically speaking companies that implement OI concepts will also achieve better results when launching new products on the market. The aforementioned OI concepts directly contribute to improving the qualities of products and services. That means better/high quality products or service, which for customers is often more important than price.

There was also a positive correlation (significant at 0.05 or less) between the OI concept talent development programme and new products. This can be interpreted that companies which invest in staff education and training develop more new products. Other positive effects but insignificant are: standardised and detailed work instruction, TPM, teamwork in production and method of 5S. However, there was one OI concept that had negative effects on launching new products: employee training for creativity and innovation. Statistically speaking increased investment in the aforementioned OI concept resulted in a decrease in newly launched products. However this concept was introduced in companies usually as a prime concept to teach employees innovative thinking, and in order to generate more new ideas for new products. This might be explained by the fact that teaching employees takes time, and consequently there is a time lag between teaching and the actual creating of new products. That might be the reason that a particular concept has a negative effect on launching new products on the market.

Finally, a multi regression analysis was performed, with new products as the dependent variable and selected OI's as independent variables in order to test how each selected OIs influences new product launch (Table 4). Multiple regression analysis yields the standardised regression coefficients which showed the change in the dependent variable measured in standard deviations.

Beta coefficients are the estimates resulting from regression analysis and standardised so that the variances of the dependent and independent variables are equal to 1. Therefore, standardised coefficients

Table 4. *Results of the regression analysis*

R	R Square	Adjusted R Square	Std. Error of the Estimate	Sig.
0.573	0.328	0.227	0.419	0.002

Coefficients (a)	Unstandardized Coefficients		Standardized Coefficients	*t*	Sig.
	B	Std. Error	Beta	B	Std. Error
(Constant)	0.329	0.154		2.140	0.036
Teamwork in production	0.027	0.137	0.024	0.200	0.842
ISO 9000 and other standards	0.197	0.138	0.173	1.428	0.158
Standardized and detailed work instruction	0.069	0.138	0.060	0.499	0.619
Method of 5S	–0.044	0.110	–0.047	–0.402	0.689
Employee training for creativity and innovation	–0.197	0.109	–0.208	–1.808	0.075
Total Productive Maintenance TPM	–0.267	0.144	–0.282	–1.856	0.068
Methods for CIP	0.128	0.112	0.135	1.148	0.255
Task integration	0.205	0.122	0.214	1.678	0.098
Total Quality Management TQM	0.330	0.138	0.346	2.385	0.020
Talent development program	0.172	0.116	0.178	1.484	0.142

a. Dependent Variable: New products

refer to how many standard deviations a dependent variable will change, per standard deviation increase in the independent variable [24]. If we look at the results of the researched model (which is significant) it can be seen that only TQM has a strong significant positive impact on new product launches. TQM with continuous efforts to raise the quality of products or services directly contribute to launch more new products. That coincides with the Santos-Vijande and Álvarez-González study [11] in which they found that TQM and CIP, which are both OIs, have a strong positive impact on new product launches because TQM focuses (among other focuses) on the customer needs and wants, and CIP also gives rise to new modifications in products and processes. Maybe the best example of how CIP, TQM and quality circles improve products and processes can be found in Spear and Bowen [34]. ISO 9000 and others also positively influence new product launches, which might be explained by the fact that ISO manuals have a chapter on guidance for improvements. The method of 5S, employee training for creativity and innovation, and TPM have a negative impact on new product launches – but these concepts give results only in the long-run and that might be the reason why they negatively affect new product launches. On the other hand method of 5S and TPM are indirectly related to innovation rather taking care of the work environment as well as taking preventive care of machines. It must also be noted that these negative influences are small and insignificant. The model shows good correlation (r = 0.573) and changes in independent variable will influence change in dependent variable (new product launch) by 33 %.

4 CONCLUSION

The purpose of this paper was to examine which OI concepts in the Slovenian manufacturing companies have the more significant impact on launching new products on the market. Analysis of the impact of the implementation of OI has shown that companies that implemented OI concepts within their systems are achieving higher shares of launching new products on the market. Regression analysis showed that especially TQM significantly increases new product launches. At the same time correlation analysis for the 10 more widely used OI concepts in the Slovenian manufacturing industry was performed and showed strong significant relationships among OI concepts, showing that for example investing in TQM practices will enhance other OI concepts.

This research has also practical and managerial implications. Our results show that the use of specific OI concepts clearly positively affects the ability to manufacture complex products and the ability to develop, manufacture and launch new product on the market. This is a clear message to managers that technical innovation and the use of advanced technologies is not a sufficient requirement to manufacture and introduce new and complex products.

As is the case with all research, some issues have to be taken into account when considering the reliability, significance, and generalities of the results obtained. First, the data is from Slovenia containing 89 companies. Although the sample is not small further research should go towards the direction of a larger sample of more countries with different levels of development and also different strategies (for example low cost strategy).

5 REFERENCES

[1] Florida, R. (2005). *The Flight of the Creative Class: The New Global Competition for Talent*. Harper Collins, New York.

[2] Nagy, T., Ruzzier, M. (2013). *Vpliv uporabnikov na proces inoviranja: upravljanje uporabniškega potenciala s strani podjetij*. Meritum, Ljubljana.

[3] McGahan, A. (2004). How industries change. *Harvard Business Review*, vol. 82, no. 6, p. 79-86.

[4] Bikfalvi, A. (2007). *Innovation, Entrepreneurship and Outsourcing: Essays on the Use of Knowledge in Business Environments*, PhD thesis. University of Gerona, Gerona.

[5] Freeman, C., Soete, L. (1997). *The Economics of Industrial Innovation*. Pinter Publisher, London.

[6] Mol, M.J., Birkinshaw, J. (2009). The sources of management innovation: When firms introduce new management practices. *Journal of Business Research*, vol. 62, no. 12, p. 1269-1280, **DOI:10.1016/j.jbusres.2009.01.001**.

[7] Schumpeter, J.A. (1934). *The Theory of Economic Development. An Inquiry into Profits, Capital, Credit, Interest, and the Business Cycle*. Harvard University Press, Cambridge.

[8] OECD (2005). *The Measurement of Scientific and Technological Activities Oslo Manual. Guidelines for Collecting and Interpreting Innovation Data (3 ed.)*. OECD EUROSTAT, Paris , **DOI:10.1787/9789264013100-en**.

[9] Camisón, C., Villar-López, A. (2014). Organizational innovation as an enabler of technological innovation capabilities and firm performance. *Journal of Business Research*, vol. 67, no. 1, p. 2891-2902, **DOI:10.1016/j.jbusres.2012.06.004**.

[10] Read, A. (2000). Determinants of successful organizational innovation: Review of current research. *Journal of Management Practice*, vol. 3, no. 1, p. 95-119.

[11] Santos-Vijande, M.L., Álvarez-González, L.I. (2007). Innovativeness and organizational innovation in total quality oriented firms: The moderating role of market turbulence, *Technovation*, vol. 27, no. 9, p. 514-532, **DOI:10.1016/j.technovation.2007.05.014**.

[12] Hong, S., Oxley, L., McCann, P. (2012). A survey of the innovation surveys. *Journal of Economic Surveys*, vol. 26, no. 3, p. 420-444, **DOI:10.1111/j.1467-6419.2012.00724.x**.

[13] Gunday, G., Ulusoy, G., Kilic, K., Alpkan, L. (2011). Effects of innovation types on firm performance. *International Journal of Production Economics*, vol. 133, no. 2, p. 662-676, **DOI:10.1016/j.ijpe.2011.05.014**.

[14] Mumford, M.D. (2000). Managing creative people: Strategies and tactics for innovation. *Human Resource Management Review*, vol. 10, no. 3, p. 313-351, **DOI:10.1016/S1053-4822(99)00043-1**.

[15] Keupp, M.M., Palmie, M., Gassmann, O. (2011). The strategic management of innovation: A systematic review and paths for future research. *International Journal of Management Reviews*, vol. 14, no. 4, p. 367-390, **DOI:10.1111/j.1468-2370.2011.00321.x**.

[16] Camisón, C., Villar-López, A. (2011). Non-technical innovation: Organizational memory and learning capabilities as antecedent factors with effects on sustained competitive advantage. *Industrial Marketing Management*, vol. 40, no. 8, p. 1294-1304, **DOI:10.1016/j.indmarman.2011.10.001**.

[17] Armbruster H., Bikfalvi A., Kinkel S., Lay G. (2008). Organizational innovation: The challenge of measuring non-technical innovation in large-scale surveys. *Technovation*, vol. 28, no. 10, p. 644-657, **DOI:10.1016/j.technovation.2008.03.003**.

[18] Palčič, I., Buchmeister, B. Polajnar, A. (2010). Analysis of innovation concepts in slovenian manufacturing companies, *Strojniški vestnik - Journal of Mechanical Engineering*, vol. 56, no. 12, p. 803-810.

[19] Al-Hawari T., Ahmed A., Khrais S., Mumani A. (2013). Impact of assignment, inventory policies and demand patterns on supply chain performance. *International Journal of Simulation Modelling*, vol. 12, no. 3, p. 164-177, **DOI:10.2507/IJSIMM12(3)3.235**.

[20] Prester, J., Bozac, M.G. (2012). Are innovative organizational concepts enough for fostering innovation? *International Journal of Innovation Management*, vol. 16, no. 1, **DOI:10.1142/S1363919611003404**.

[21] Damanpour F., Aravind D. (2012). Managerial innovation: Conceptions, processes, and antecedents. *Management and Organization Review*, vol. 8, no. 2, p. 423-454, **DOI:10.1111/j.1740-8784.2011.00233.x**.

[22] Crossan, M.M., Apaydin, M. (2010). A multi-dimensional framework of organizational innovation: A systematic review of the literature. *Journal of Management Studies*, vol. 46, no. 6, p. 1154-1191, **DOI:10.1111/j.1467-6486.2009.00880.x**.

[23] Wright, C., Sturdy, A., Wylie, N. (2012). Management innovation through standardization: Consultants as standardizers of organizational practice. *Research Policy*, vol. 41, no. 3, p. 652-662, **DOI:10.1016/j.respol.2011.12.004**.

[24] Jin, Z., Hewitt-Dundas, N., Thompson, N.J. (2004). Innovativeness and performance: evidence from manufacturing sectors. *Journal of Strategic Marketing*, vol. 12, no. 4, p. 255-266, **DOI:10.1080/0965254042000308075**.

[25] Delarue, A., Van Hootegem, G., Procter, S., Burridge, M. (2007). Teamworking and organizational performance: A review of survey-based research. *International Journal of Management Reviews*, vol. 10, no. 2, p. 127-148, **DOI:10.1111/j.1468-2370.2007.00227.x**.

[26] Jiménez-Jiménez, D., Sanz-Valle, R. (2011). Innovation, organizational learning, and performance. *Journal of Business Research*, vol. 64, no. 4, p. 408-417, **DOI:10.1016/j.jbusres.2010.09.010**.

[27] Bolivar-Ramos, M.T., Garcia-Morales, V.J., Garcia-Sanchez, E. (2012). Technological distinctive competencies and organizational learning: Effects on organizational innovation to improve firm performance. *Journal of Engineering and Technology Management*, vol. 29, no. 3, p. 331-357, **DOI:10.1016/j.jengtecman.2012.03.006**.

[28] Evangelista, R., Vezzani, A. (2010). The economic impact of technological and organizational innovations. A firm-level analysis. *Research Policy*, vol. 39, no. 10, p. 1253-1263, **DOI:10.1016/j.respol.2010.08.004**.

[29] Laforet, S. (2013). Organizational innovation outcomes in SMEs: Effects of age, size, and sector. *Journal of World Business*, vol. 48, no. 4, p. 490-502, **DOI:10.1016/j.jwb.2012.09.005**.

[30] Hamel, G. (2009). Management Innovation: This is now a do-or-die management matter. *Leadership Excellence*, vol. 26, no. 5.

[31] Lai, X.D., Wu, G.-D., Shi, J.G., Wang, H.M., Kong, Q.S. (2015). Project value-adding optimization of project-based supply chain under dynamic reputation incentives. *International Journal of Simulation Modelling*, vol. 14, no. 1, p. 121-133, **DOI:10.2507/IJSIMM14(1)CO1**.

[32] Gong, D., Liu, S., Lu, X. (2015). Modelling the impacts of resource sharing on supply chain efficiency. *International Journal of Simulation Modelling*, vol. 14, no. 4, p. 744-755, **DOI:10.2507/IJSIMM14(4)CO20**.

[33] Koren, R., Palčič, I. (2015). The impact of technical and organisational innovation concepts on product characteristics. *Advances in Production Engineering & Management*, vol. 10, no. 1, p. 27-39, **DOI:10.14743/apem2015.1.190**.

[34] Spear, S.J., Bowen, H.K. (1999). Decoding the DNA of the Toyota Production System. *Harvard Business Review*, no. Sep-Oct, p. 96-106.

ERRATA

The Journal has been informed of errors in the recent article Petan, L., Ocaña, J., Grum, J. (2016). Effects of Laser Shock Peening on the Surface Integrity of 18 % Ni Maraging Steel. *Strojniški vestnik - Journal of Mechanical Engineering*, vol. 62, no. 5, p. 291-298, doi:10.5545/sv-jme.2015.3305. The typo occurs in the reference section at references [5], [12] and [13], where the author should be read correctly Ocaña.

The Journal regrets these errors, which occur at layout phase. The revised version of the article is available online.

Vsebina

Strojniški vestnik - Journal of Mechanical Engineering
letnik 62, (2016), številka 6
Ljubljana, junij 2016
ISSN 0039-2480

Izhaja mesečno

Razširjeni povzetki (extended abstracts)

Strojniški vestnik - Journal of Mechanical Engineering 62(2016)6, SI 59

Prejeto v recenzijo: 2015-12-08
Prejeto popravljeno: 2016-03-14
Odobreno za objavo: 2016-04-14

Postopek reševanja inverznega problema za določitev toplotne prestopnosti med ukapljenim dušikom in obdelovancem iz Inconela 718 pri kriogenem odrezavanju

Matija Hriberšek[1,*] – Viktor Šajn[1] – Franci Pušavec[1] – Joel Rech[2] – Janez Kopač[1]
[1] Univerza v Ljubljani, Fakulteta za strojništvo, Slovenija
[2] Univerza v Lyonu, Fakulteta za strojništvo Saint-Etienne, Francija

Cilj članka je prispevek k boljšem razumevanju vpliva ukapljenega dušika, ki se uporablja kot hladilo pri odrezavanju, na prestop toplote v Inconelu 718. V raziskavah je bila definirana toplotna prestopnost med ukapljenim dušikom in površino obdelovanca v odvisnosti od faze dušika. Uporabljeni material je bil Inconel 718, ki je visoko temperaturna zlitina niklja in kroma z izjemnimi mehanskimi in termičnimi lastnostmi in se uporablja v izdelkih z visoko dodano vrednostjo. Raziskava je bila izvedena na podlagi nepoznavanja natančnih vrednosti za toplotno prestopnost za omenjen kriogen fluid, saj so bile v dosedanjih raziskavah podane zgolj okvirne vrednosti.

Članek pojasnjuje razlike v vrednostih med toplotno prestopnostjo za kapljevito in plinasto fazo dušika v odvisnosti od razlike temperatur (ukapljen dušik-površina plošče iz Inconela 718). Cilj raziskave je bil dosežen z opravljenimi eksperimenti merjenja temperature s termoelementi v Inconelu 718, ob prehodu curka z ukapljenim dušikom čez ploščo. Nato je bila zasnovana numerična simulacija z uporabo končnih elementov, ki je popisala razmere pri eksperimentu. Glede na ujemanje padcev temperatur v materialu pri eksperimentu in numerični simulaciji, smo določili toplotno prestopnost v simulaciji med ukapljenim dušikom in površino Inconela 718, kar je bila procedura reševanja inverznega problema. Pristop k reševanju inverznega problema je bil eksperimentalno analitičen, saj se je uporabljalo eksperimentalno in analitično metodo (numerična simulacija) pri razreševanju problema prevoda toplote skozi ploščo iz Inconela 718.

Rezultati so potrdili, da toplotna prestopnost med ukapljenim dušikom in površino obdelovanca iz Inconela 718 ni konstantna vrednost, ampak pada z naraščajočo temperaturo kriogenega fluida. Dobljeni rezultati potrjujejo že določene intervale vrednosti za toplotno prestopnost, katera doseže maksimalno vrednost, pri razliki temperature med kriogenim fluidom in površino obdelovanca okoli 196 K (h = 75000 W/(m^{2}K)). Ta pojav se zgodi, ko je prisotna kapljevita faza dušika. Razpon v razliki temperatur med utekočinjenim dušikom in površino plošče (180 K in 120 K) glede na vrednosti za toplotno prestopnost nakazuje, da je bila prisotna mešana faza dušika. Medij izgubi hladilni vpliv, ko preide v plinasto fazo (ΔT = 100 K, h = 1500 W/(m^{2}K)), kar opredeljuje naravno konvekcijo zraka. Iz rezultatov raziskav se da tudi razbrati, da je vpliv toplotne prestopnosti očitno zmanjšan zaradi mehurčkastega vrenja, ki se pojavi pri plinasti fazi dušika, saj ima omenjena faza zelo nizko toplotno prevodnost (λ= 0.03 W/(mK)). V primeru, da se hladilni učinek medija vrednoti glede na obliko površine, na katero je bil ukapljen dušik usmerjen, je simulacija omejena le na ravno površino in ne na obdelovance ostalih oblik. Z uporabljenimi podobnimi hitrostmi pomika šobe in z upoštevanjem majhne površine, na katero je bil usmerjen tok fluida, se je želelo simulirati in približati stopnji podhladitve v materialu pri enem obratu struženja in jo nato posplošiti na kontinuiran odrezovalni postopek.

Glede na mnogo višje vrednosti pri toplotni prestopnosti za kapljevito fazo (h = 75000 W/(m^{2}K)), proti toplotni prestopnosti, ko se medij nahaja v plinasti fazi (h = 10000 W/(m^{2}K)), ima kapljevita faza mnogo večji hladilen učinek na material. To je glavni doprinos, saj je v preteklih objavah moč zaslediti le podane intervalne vrednosti za toplotno prestopnost za omenjen kriogen fluid.

Članek je aplikativne in znanstvene narave in bo odločilno prispeval k večjemu razumevanju vpliva ukapljenega dušika na obdelovalnost materiala, saj se le ta uporablja kot hladilo pri odrezavanju in prispeva k boljši integriteti površine po obdelavi (hrapavost površine, zaostale napetosti, ipd.).
Ključne besede: ukapljen dušik, kriogeno odrezavanje, inverzen problem, merjenje temperature, numerična simulacija, toplotna prestopnost

*Naslov avtorja za dopisovanje: Univerza v Ljubljani, Fakulteta za strojništvo, Aškerčeva 6, 1000 Ljubljana, Slovenija, matija.hribersek@fs.uni-lj.si

Strojniški vestnik - Journal of Mechanical Engineering 62(2016)6, SI 60

Prejeto v recenzijo: 2015-12-11
Prejeto popravljeno: 2016-03-23
Odobreno za objavo: 2016-04-18

Napovedovanje rezalnih sil pri frezanju več-slojnih kovinskih materialov s krogelnim oblikovnim frezalom

Uroš Župerl* – Franci Čuš – Tomaž Irgolič
Univerza v Mariboru, Fakulteta za strojništvo, Slovenija

Namen raziskave je uporabiti metodo umetnih nevronskih mrež (ANN) pri izdelavi učinkovitega modela za napovedovanje rezalnih sil med frezanjem več-slojnih kovinskih materialov, izdelanih z najbolj razširjenim dodajnim postopkom LENS.

Cilj članka je predstaviti postopek izdelave nevronskega napovednega modela in eksperimentalno raziskati odrezovalne razmere pri frezanju 16MNCr5/316L štiri-slojnega kovinskega materiala s krogelnim oblikovnim frezalom.

Predstavljena je prilagoditev topologije ANN k problemu napovedovanja rezalnih sil. Za izvedbo modeliranja treh komponent rezalne sile je uporabljena popularna tri nivojska arhitektura usmerjene nevronske mreže z učnim algoritmom vzvratnega širjenja napake. Izdelan nevronski model vsebuje sedem vhodnih nevronov, ki predstavljajo: podajalno hitrost, aksialno globino rezanja, radialno globino rezanja, kot zasuka orodja, premer orodja, trdota izdelanega sloja in debelina navarjenega sloja. Pri izdelavi napovednega modela sta upoštevana dva LENS procesna parametra ter trdota in debelina posameznega navarjenega sloja omenjenega naprednega materiala. Število skritih nivojev in optimalno število nevronov v posameznem nivoju je določeno s simulacijami. Optimalni nevronski model vsebuje 3 in 5 nevronov v skritem nivoju. Izhod iz modela so tri komponente rezalne sile, zato so potrebni trije izhodni nevroni.

Eksperimentalni podatki za izdelano napovednega modela so pridobljeni v petih korakih. V prvem koraku je izdelanih devet testnih obdelovancev iz 16MnCr5 osnovnega materiala. Nato so na osnovni material navarjeni 4 sloji nerjavnega jekla (316L) z različnimi debelinami in trdotami posameznega sloja. Testni obdelovanci so izdelani na Optomec LENS 850-R stroju. V drugem koraku sta izmerjeni trdota in debelina navarjenih slojev. Debelina izdelanih slojev je izmerjena na Nikon Epiphot 300 metalurškem mikroskopu.

V tretjem koraku so analizirani vplivi LENS procesnih parametrov na debelino in trdoto izdelanega sloja. Vplivi LENS procesnih parametrov na trdoto in debelino navarjenega sloja so prikazani na grafih. Ugotovljeno je, da ima moč laserja in hitrost navarjanja največji vpliv na trdoto in debelino posameznega sloja več-slojnega kovinskega materiala.

V četrtem koraku so izvedeni obdelovalni eksperimenti za vse tipične kombinacije rezalnih parametrov. Obdelovalni eksperimenti so izvedeni na CNC obdelovalnem stroju Heller BEA02. Rezalne sile so izmerjene s piezo-električnim dinamometrom (Kistler 9255) nameščenim med obdelovancem in mizo stroja. Izbrano je v orodjarni najpogosteje uporabljeno oblikovno frezalo iz sintranega materiala in trdoto 1770 HV.

V petem koraku so rezultati izmerjenih sil analizirani in pripravljeni za učenje napovednega modela. Vrednosti izmerjenih rezalnih sil so grafično predstavljene na diagramih v odvisnosti od kota zasuka rezalnega orodja. Vplivi LENS procesnih parametrov in rezalnih parametrov na potek rezalne sile so prikazani na grafih. Debelina izdelanega sloja ima signifikanten vpliv na rezalne sile. Rezalne sile so večje od pričakovanih pri aksialna globina frezanja, ki je enaka debelini navarjenega sloja. Vzrok bi lahko bil v nehomogeni strukturi mejnega področja med dvema izdelanima slojema.

Izvedena je validacija modela s primerjavo napovedi modela in eksperimentalnih podatkov. S primerjavo je ugotovljeno, da lahko metoda natančno napove rezalne sile z napako manjšo od 4,8 % Večina napovedanih vrednosti rezalnih sil je ekvivalentna s pripadajočimi eksperimentalnimi vrednostmi. Nadaljnje aktivnosti bodo usmerjene k implementaciji nevronskega modela v proizvodno okolje in k nadgrajevanju modela z novimi kombinacijami orodje/obdelovanec.

Ključne besede: oblikovno frezanje, rezalne sile, več-slojni material, LENS, napovedovanje, nevronska mreža

*Naslov avtorja za dopisovanje: Univerza v Mariboru, Fakulteta za strojništvo, Smetanova ulica 17, 2000 Maribor, Slovenija, uros.zuperl@um.si

Strojniški vestnik - Journal of Mechanical Engineering 62(2016)6, SI 61

Prejeto v recenzijo: 2016-01-24
Prejeto popravljeno: 2016-03-10
Odobreno za objavo: 2016-03-24

Nelinearne vibracije sistema rotor-kapljevina-temelji, podprtega s kotalnimi ležaji

Almatbek Kydyrbekuly[1] – Leyla Khajiyeva[1] – Alysher Ybraev Gulama-Garyp [1] – Julius Kaplunov[2]
[1] Kazahstanska nacionalna univerza Al-Farabi, Kazahstan
[2] Univerza Keele, Združeno kraljestvo

Članek preučuje dinamiko sistema rotor-tekočina-temelji ob upoštevanju linearne ekscentričnosti, dušenja in nelinearnosti kotalnih ležajev. Rotor, katerega cilindrična votlina je delno napolnjena z idealno nestisljivo kapljevino, je povezan s kotalnimi ležaji in elastično podprt s temelji. Visokohitrostni rotacijski stroji imajo pomembno vlogo v sodobni industriji, kjer opravljajo naloge prenosa navora in vrtilnega gibanja v mnogih energetskih, električnih in vrtalnih sistemih, vključno s plinskimi turbinami, kompresorji, separatorji, centrifugalnimi črpalkami in stroji za tekstil.

Članek obravnava razvoj splošnega matematičnega modela za vrednotenje sklopljenih nelinearnih nihanj in preučevanje stabilnosti gibanj. Eden glavnih poudarkov je vključitev deformabilnosti ležajev, ki postane pomembna pri visokih hitrostih vrtenja in močno vpliva na visoko natančnost delovanja. Nelinearne elastične deformacije, ki so povezane s tem, imajo radialno in obodno komponento. Naslednji izziv pri obravnavanih sistemih je močna sklopitev med gibanjem rotorja in tekočine, ki vpliva na frekvence vibracij in povzroča nestabilnosti.

Izpeljane so enačbe gibanja na podlagi klasičnih formulacij dinamike togih teles in mehanike fluidov. Vključena je Hertzova teorija za modeliranje vpliva nelinearnih deformacij ležajev in oblikovana je približna analitična rešitev za prej omenjene enačbe. Podrobno so analizirana lastna in vsiljena nihanja in predstavljene so omejitve s posebnostmi dinamičnega vedenja, vključno z možnostjo samocentriranja, povezanega z ničelnim pritiskom na podpore. Podane so preprosto razumljive eksplicitne formule za frekvence in amplitude vibracij. Izdelani so grafi, ki predstavljajo nestabilna področja lastnih nihanj za več različnih vrednosti mase tekočine v votlini, predstavljene pa so tudi krivulje odziva rotorja in temeljev. Iz fenomenološke analize predstavljenih numeričnih podatkov sledi več uporabnih zaključkov.

Predlagani pristop podaja takojšnji kakovostni vpogled v vrsto praktičnih problemov dinamike rotorjev in omogoča več posplošitev, vključno z implementacijo pristopa pri modeliranju centrifug, ki ločujejo kapljevito od trdne faze. Metodologijo, uporabljeno v članku, bi bilo mogoče dopolniti s fleksibilnostjo gredi in žiroskopskimi pojavi, dovolj robustna pa je tudi v prehodnih režimih. Rezultati omogočajo izbiro optimalnih parametrov rotorja, temeljev in tekočine za minimalno amplitudo vibracij in napetosti sistema, kakor tudi za zmanjšanje širine nestabilnih območij. Omogočajo tudi določanje pogojev za samocentriranje, končno pa odpirajo tudi priložnosti za omejevanje škodljivih nihanj s spreminjanjem lastnosti temeljev.

Ključne besede: rotor, temelji, kotalni ležaji, nelinearne vibracije, resonanca, kapljevina, votlina

*Naslov avtorja za dopisovanje: Univerza Keele, Fakulteta za računalništvo in matematiko, ST5 5BG, Združeno kraljestvo, j.kaplunov@keele.ac.uk

Strojniški vestnik - Journal of Mechanical Engineering 62(2016)6, SI 62

Prejeto v recenzijo: 2015-11-12
Prejeto popravljeno: 2016-03-17
Odobreno za objavo: 2016-03-30

Navarjanje kompozitnih prevlek iz Inconela 625/WC z direktnim diodnim laserjem

Damian Janicki* – Małgorzata Musztyfaga-Staszuk
Šlezijska tehniška univerza, Fakulteta za strojništvo, Poljska

Prevleke iz kompozita s kovinskim matriksom (MMC), sestavljene iz zlitine Inconel 625 in volframovega karbida (WC), so možna rešitev za potrebe zaščitnih prevlek v industriji, ki zahtevajo visoko stopnjo protikorozijske in protierozijske obstojnosti. Pri zgornjem sistemu kompozitne prevleke je treba upoštevati več pomembnih dejavnikov. Glavni problem je raztapljanje WC v zlitini matriksa, ki povzroči oblikovanje sekundarnih faz ter lahko privede do poslabšanja protiobrabnih in protikorozijskih lastnosti prevleke. Do danes je bilo opravljenih že veliko študij vpliva velikosti delcev WC in vnosa toplote pri laserskem navarjanju na stopnjo raztapljanja WC v talilni kopeli ter na povezane spremembe mikrostrukture pri nikljevih prevlekah MMC. Žal pa je bilo objavljenih le malo raziskav vpliva oblike delcev WC na lastnosti nikljevih prevlek MMC.

V predstavljeni študiji je bila izdelana kompozitna prevleka iz Inconela 625/WC po postopku navarjanja z direktnim diodnim laserjem velike moči, in sicer s pravokotno lasersko točko in s ploskim profilom žarka. Material za prevleko je bil pripravljen v obliki prašnate zmesi plinsko atomizirane zlitine Inconel 625 za matriks ter delcev WC, tako oglate kot sferične oblike. Za celovito analizo vpliva dodatka WC na geometrijo prevleke po enem prehodu in na mikrostrukturo matriksa je bil uporabljen tudi čist prah iz zlitine Inconel 625. Postopek laserskega navarjanja je bil opravljen z neposrednim vbrizgavanjem prahu v talilno kopel prek zunajosnega sistema. Glavni cilj preiskave je bil razumevanje vloge oblike delcev WC in stopnje vnosa toplote na kakovost uporabljenega sistema kompozitne prevleke, še posebej na njegove erozijske lastnosti. Mikrostruktura prevlek je bila analizirana po postopku vrstične elektronske mikroskopije (SEM) z energijsko disperzivno spektroskopijo (EDS) in rentgensko difrakcijo (XRD). Protierozijska obstojnost kompozitnih prevlek in kovinske prevleke Inconel 625 je bila preizkušena po standardu ASTM G76. Mehanizem erozijske obrabe kompozitnih prevlek je bil preučen z vrstičnim elektronskim mikroskopom.

Rezultati kažejo, da imajo kompozitne prevleke na osnovi Inconela 625 ter oglatih oz. okroglih delcev WC, navarjene z diodnim laserjem, enakomerno porazdelitev delcev WC po matriksu, ter da so prehodna območja med delci WC in matriksom brez napak. Stopnja raztapljanja WC je neposredno odvisna od vnosa toplote, kakor tudi od oblike delcev WC. Z večanjem vnosa toplote se povečuje tudi stopnja raztapljanja WC, zaradi česar se v matriksu in še posebej v območju prehoda oblikujejo sekundarne faze, bogate z volframom. Oglati delci WC so bolj nagnjeni k raztapljanju v talilni kopeli kot sferični delci. Pri prevlekah z oglatimi delci WC je bila ugotovljena tudi daljša srednja prosta pot (MFP) med delci WC. Razliko v vrednostih MFP pri teh prevlekah je mogoče pojasniti z različnimi stopnjami raztapljanja WC, pa tudi z dejstvom, da se okrogli delci bolje zlagajo. Kljub zgoraj omenjenim strukturnim lastnostim imajo prevleke z oglatimi delci WC boljšo protierozijsko obstojnost kot prevleke z okroglimi delci WC, tako pri normalnem kot pri poševnem kotu preizkušanja. Pri kotu 90° so bile tako erozijske vrednosti prevlek s sferičnim WC skoraj dvakrat večje kot pri prevlekah z oglatimi delci WC. To lahko neposredno pripišemo odličnemu mehanskemu prijemanju delcev WC nepravilnih oblik z matriksom in s sosednjimi delci WC. Pri sferičnih delcih WC je zaradi zelo gladkega stika z matriksom močno olajšano odstranjevanje matriksa pri preizkusih pod normalnim kotom. Sferični delci WC so tudi nagnjeni k medpovršinski dekoheziji RP/matriksa pri preizkusih pod poševnim kotom.

Ključne besede: lasersko navarjanje, kompozitna prevleka s kovinskim matriksom, direktni diodni laser, Inconel 625, erozijska obraba

*Naslov avtorja za dopisovanje: Šlezijska tehniška univerza, Fakulteta za strojništvo, Konarskiego 18A, Gliwice, Poljska, damian.janicki@polsl.pl

Strojniški vestnik - Journal of Mechanical Engineering 62(2016)6, SI 63

Prejeto v recenzijo: 2015-10-07
Prejeto popravljeno: 2016-02-15
Odobreno za objavo: 2016-03-15

Modeliranje kavitacijskega toka skozi odprtino v hidravličnih sistemih z zgoščenimi parametri

Junjie Zhou* – Jibin Hu – Chongbo Jing
Državni laboratorij za transmisije v vozilih, Institut za tehnologijo v Pekingu, Kitajska

Plinska kavitacija je pomemben problem, ki negativno vpliva na delovanje hidravličnih sistemov. Modeliranje z zgoščenimi parametri (LP) je uveljavljen pristop pri raziskavah hidravličnih sistemov zaradi možnosti hitre in prikladne uporabe na sistemski ravni. Članek predstavlja nov model kavitacijskega toka skozi odprtino z zgoščenimi parametri, ustvarjen po konceptu kontrolnih prostornin.

Podan je postopek za umerjanje neznanih koeficientov modela po metodi CFD, kakor tudi testni podatki. Postavljeno je bilo preizkuševališče za preučevanje kavitacije v zunanji zobniški črpalki z variabilno odprtino na vhodu. Najprej so bili opredeljeni štirje koeficienti CFD-modela kavitacije na podlagi izmerjenega masnega pretoka skozi preizkusno odprtino. Simulacija tokovnega polja po metodi CFD daje vse potrebne podatke, vključno s povprečnim dolvodnim masnim deležem zraka za določitev dveh koeficientov modela LP.

V postopku umerjanja modela se najprej uporabi izmerjeni masni pretok skozi odprtino pri treh dolvodnih tlakih za umerjanje štirih koeficientov modela CFD. Po izbiri primernih vrednosti se uporabi simulirano polje tekočine iz paketa Fluent za izračun parametrov modela kavitacije LP. Koeficienti, uporabljeni pri obeh pristopih, se nato uporabijo za primerjavo s preizkusi pri drugih delovnih pogojih.

Predlagani pristop in postopek umerjanja sta uporabna, saj zagotavljata dobro ujemanje z rezultati eksperimentov.

Raziskava je omejena v tem, da točnost merilnikov pretoka vpliva na vrednosti koeficientov in da model LP morda ni primeren za vse enote z zelo zapleteno zgradbo.

Članek predstavlja nov model za napovedovanje plinske kavitacije v hidravličnih odprtinah, kjer je odprtina po pristopu modeliranja z zgoščenimi parametri poenostavljena v tri povezane kontrolne prostornine. Ujemanje z eksperimentalnimi podatki dokazuje velik potencial predlaganega modela kavitacije z zgoščenimi parametri, ki je prikladnejši za preučevanje kavitacije v hidravličnih sistemih. Uspeh te raziskave je lahko podlaga za nadaljnje študije plinske kavitacije v hidravličnih regulacijskih ventilih ali visokohitrostnih črpalkah.
Ključne besede: plinska kavitacija, zgoščeni parametri, odprtina, hidravlični sistemi, CFD, umerjanje

*Naslov avtorja za dopisovanje: Državni laboratorij za transmisije v vozilih, Institut za tehnologijo v Pekingu, Kitajska, bit_zhou50082@163.com

Strojniški vestnik - Journal of Mechanical Engineering 62(2016)6, SI 64

Prejeto v recenzijo: 2015-11-15
Prejeto popravljeno: 2016-04-06
Odobreno za objavo: 2016-04-26

Merjenje izbranih parametrov prenosnikov toplote s polipropilenskimi vlakni

Mária Čarnogurská[1,*] – Miroslav Příhoda[2] – Marián Lázár[1] – Natália Jasminská[1] – Róbert Gallik[1] – Michal Kubik[1]
[1]Tehniška univerza v Košicah, Fakulteta za strojništvo, Slovaška
[2]Tehniška univerza v Ostravi, Fakulteta za metalurgijo in materiale, Češka republika

Namen tega članka je osvetlitev problemov, povezanih z izdelavo in delovanjem prenosnikov toplote s prenosno površino iz polipropilenskih vlaken. Najprej je bila opravljena raziskava spajanja vlaken po postopku zalivanja, ki mora biti izvedeno popolnoma tesno. Vsak snop vlaken je zalit na začetku in na koncu. Nato je bil preučen vpliv sprostitve napetosti snopa na prenos toplote in s tem na kapaciteto prenosnika toplote.

To je pomembno za nadzor funkcionalnosti prenosnika toplote v različnih režimih. Preučene so bile tri vrste snopov s 400, 900 in 1385 vlakni različnega premera (0,65 mm, 0,3 mm in 0,275 mm) v različnih režimih napetosti oz. sproščenosti vlaken. Konstrukcija eksperimentalnega prenosnika toplote omogoča sprostitev vlaken v območju od 0 % do 10 %.

Tesnost zalitja vlaken je bila eksperimentalno preizkušena. Voda pod tlakom je bila speljana skozi vodni filter, zapiralni ventil in merilnik tlaka na snop vlaken, skozi vlakna na drugo zalitje in nato ven iz prenosnika toplote. Tlak vode na vhodu v vodni filter je bil nastavljen na 0,3 MPa. Po obremenitvi vlaken z vodnim tlakom sta bila zaprta ventila pred in za zalitjem, nato pa je bil izmerjen padec tlaka po izteku določenega časa. Snop vlaken brez znakov popuščanja je bil potopljen v vodo pri temperaturi od 50 °C do 70 °C. Po ohladitvi vlaken na vstopno temperaturo vode je bil snop izpostavljen vodnemu tlaku 0,3 MPa. Zalitje je bilo preizkušeno v več opisanih ciklih.

Več avtorjev je preučevalo uporabnost prenosnikov toplote s polipropilenskimi vlakni, predvsem z vidika dovzetnosti polipropilenskih vlaken do biološkega onesnaženja v primerjavi z nerjavnim jeklom (bakterija Escherichia coli), uporabe prenosnikov toplote s polipropilenskimi vlakni za odvajanje odpadne toplote gospodinjske in industrijske vode, in uporabe tovrstnih prenosnikov (kot virom toplote) za toplotne črpalke. Preučevali so tudi interakcije med gibanjem vlaken in prenosom toplote, vpliv oblike in velikosti prenosne površine na kapaciteto prenosnika toplote itd.

Ugotovitve iz tega članka so uporabne v praksi in pri znanstvenih raziskavah. Članek razširja obstoječi obseg znanja z novimi spoznanji o temperaturnih mejah za brezhibno obratovanje izmenjevalnikov toplote.

Rezultati raziskav tesnjenja zalitij so pokazali praktično uporabnost snopov polipropilenskih vlaken le do temperature 50 °C. Pri višjih temperaturah pride do popuščanja zalitja, ki je izdelano iz treh različnih materialov (kovina, lepilo, polipropilen) z različnim odzivom na temperaturne spremembe (imajo različne koeficiente toplotne prevodnosti). Tesnjenje zalitij je bilo preizkušeno pri tlaku 0,3 MPa. Ta tlak daje zadostno rezervo za realno uporabo prenosnikov toplote pri odpadni vodi z majhno toplotno kapaciteto.

Meritve so tudi pokazale, da imajo lahko ti prenosnikov toplote z vlakni večjo toplotno moč kot konstrukcije s tesnimi vlakni. Pri večini pretočnih prerezov vlaken je bila dosežena večja vrednost toplotne prehodnosti, ko so bila vlakna v snopu popuščena za pribl. 1 %. Pri manjših pretočnih prerezih vlaken je sprejemljivo tudi večje popuščanje (nad 3 %). Rezultat je v določeni meri povezan z rahlim premikom vlaken v smeri prereza, ki po določeni sprostitvi vlaken povzroči intenzivnejši prenos toplote med primarnim in sekundarnim medijem. Ogrevalno zmogljivost prenosnika določa celotna toplotna prehodnost prek stene med medijema. Eksperimenti so pokazali, da dosega toplotna prehodnost prenosnika toplote vrednosti do pribl. 800 $W \cdot m^{-2} \cdot K^{-1}$, odvisno od sproščenosti snopa. V določenih razmerah je toplotna kapaciteta odvisna samo od velikosti površine za prenos toplote, torej od števila vlaken v snopu. Uporabnost polipropilenskih vlaken je omejena z njihovo obstojnostjo proti toploti in tlaku ter z njihovo trdnostjo.

Ključne besede: polipropilenska vlakna, prenosnik toplote, meritev, celotni koeficient prenosa toplote

*Naslov avtorja za dopisovanje: Tehniška univerza v Košicah, Fakulteta za strojništvo, Košice, Slovaška, maria.carnogurska@tuke.sk

Strojniški vestnik - Journal of Mechanical Engineering 62(2016)6, SI 66

Prejeto v recenzijo: 2016-02-01
Prejeto popravljeno: 2016-03-15
Odobreno za objavo: 2016-03-30

Ali organizacijske inovacije vplivajo na uvedbo novih izdelkov na tržišče?

Rolando Koren[1] – Jasna Prester[2] – Borut Buchmeister[1] – Iztok Palčič[1,*]
[1] Univerza v Mariboru, Fakulteta za strojništvo, Maribor, Slovenija
[2] Univerza v Zagrebu, Ekonomsko-poslovna fakulteta, Zagreb, Hrvaška

Poglavitni namen prispevka je raziskati razširjenost tipičnih organizacijskih konceptov za dvig inovativnosti (organizacijske inovacije) v slovenskih proizvodnih podjetjih ter preučiti njihov vpliv na sposobnost razvoja in uvajanja novih izdelkov na tržišče. Organizacijski koncepti so sicer precej poznani, vendar je njihov vpliv na inovativnost in poslovanje proizvodnih podjetij slabo raziskan. Z uporabo različnih statističnih metod (deskriptivna statistka, korelacije in regresijska analiza) smo analizirali rezultate anketne raziskave, ki smo jo izvedli v letih 2012 in 2013.

Naša raziskava temelji na podatkih iz največje evropske ankete o proizvodni dejavnosti in vključuje podatke iz slovenskih proizvodnih podjetij. V anketi sprašujemo podjetja o proizvodnih strategijah, rabi tehniških in organizacijskih inovacij, selitvi proizvodnje, tipih proizvodnje in izdelkov, konkurenčnih kriterijih, kvalifikacijah in izobrazbi zaposlenih, energetski učinkovitosti podjetij ter o na izdelek vezanih storitvah. Zbiramo tudi podatke o produktivnosti, fleksibilnosti, kakovosti, donosih ipd.

Predstavili smo 22 tipičnih organizacijskih inovacij in njihovo razširjenost v slovenskih proizvodnih podjetjih. Ugotovili smo, da pri rabi določenih konceptov obstajajo pomembne medsebojne korelacije, npr. med konceptom celovitega zagotavljanja kakovosti (TQM) in konceptom celovitega vzdrževanja proizvodnje (TPM); integracijo nalog in TPM; metodami za kontinuirano izboljševanje procesov (CIP) in TPM ipd. Ugotavljali smo prav tako, kakšen je vpliv organizacijskih inovacij na sposobnost proizvajanja kompleksnih izdelkov. Izsledki kažejo, da ima uvedba večine organizacijskih konceptov pozitiven vpliv na sposobnost proizvodnje kompleksnih izdelkov. Največji fokus raziskave je bil na ugotovitvi, če sploh in kateri organizacijski koncepti imajo največji vpliv na sposobnost razvoja in uvajanja novih izdelkov na tržišče. Ugotovili smo, da imajo pri tem največji vpliv koncepti TQM, integracija nalog, standardi kakovosti ISO 9000 in CIP.

Naša raziskava ima določene omejitve, vezane predvsem na geografsko omejitev (Slovenija) in velikost analiziranega vzorca. V nadalnjih razikavah bomo skušali v raziskavo vključiti izsledke partnerskih držav v projektu in analizirati raziskovalna vprašanja znotraj specifičnih industrij.

Smatramo, da je naš prispevek izviren, saj podobnih raziskav s področja organizacijskih inovacij in njihovega vpliva na sposobnost proizvodnje kompleksnih izdelkov ter uvedbo novih izdelkov na tržišče nismo našli. Nasploh je literatura na temo organizacijskih inovacij še precej redka in razpršena, zato menimo, da naš prispevek odpira nove perspektive pri preučevanju značilnosti in vpliva organizacijskih inovacij na poslovanje proizvodnih podjetij.

Članek ima praktični prispevek, saj menedžerjem proizvodnih podjetij jasno nakazuje, kako in katere organizacijske inovacije vplivajo na sposobnost razvoja in uvajanja različno kompleksnih novih izdelkov na tržišče. Jasno je razvidno, da tehniške inovacije in napredna tehnologija niso zadosten pogoj za inovativnost podjetij pri uvedbi novih izdelkov na tržišče.

Ključne besede: inovativnost, organizacijska inovacija, nov izdelek, tržišče, kompleksnost izdelka, anketna raziskava

*Naslov avtorja za dopisovanje: Univerza v Mariboru, Fakulteta za strojništvo, Smetanova ulica 17, 2000 Maribor, Slovenija, iztok.palcic@um.si

DOKTORSKE DISERTACIJE

DOKTORSKA DISERTACIJA

Na Fakulteti za strojništvo Univerze v Ljubljani sta obranila svojo doktorsko disertacijo:

● dne *25. maja 2016* **Sebastjan ŽAGAR** z naslovom: »Udarno utrjevanje aluminijeve zlitine v različnih stanjih« (mentor: prof. dr. Janez Grum);

V doktorskem delu so predstavljene raziskave in analize mehanskega udarnega utrjevanja s trdimi jeklenimi kroglicami na izbrano aluminijevo zlitino AlZn5.5MgCu, ki je bila pred tem dodatno toplotno obdelana.

V prvem sklopu raziskav smo analizirali površinski sloj po mehanskem udarnem utrjevanju, kar je podprto s porazdelitvijo in velikostjo izločkov, z mikrostrukturno analizo merjenja mikrotrdote, hrapavosti in zaostalih napetosti. Druga skupina raziskav je bila usmerjena na določevanje odpornosti materiala na utrujanje podprta s testi utrujanja in določevanje stanja materiala s pomočjo neporušnega merjenja električne prevodnosti. V tretji skupini raziskav pa smo obravnavali korozijsko odpornost mehansko udarno utrjenega materiala v različnih stanjih in ga primerjali z neobdelanimi vzorci v našem izhodiščnem gašenem stanju. Izvedli smo meritve korozijskega potenciala odprtega kroga, meritve ciklične polarizacije in mikrostrukturno analizo korozijskih zajed v materialu.

Cilj in namen doktorskega dela je bil določiti najugodnejšo temperaturo staranja izmed danih ter ugotoviti kako mehansko udarno utrjevanje in stopnja pokritja vplivata na lastnosti aluminijeve zlitine.

● dne *18. maja 2016* Uroš PLAZNIK z naslovom: »Parametrična analiza delovanja aktivnega elektrokaloričnega regeneratorja« (mentor: izr. prof. dr. Andrej Kitanovski, somentor: prof. dr. Alojz Poredoš);

V doktorskem delu so predstavljeni rezultati teoretične in eksperimentalne analize delovanja aktivnega elektrokaloričnega regeneratorja, ki je osnovna komponenta elektrokalorične hladilne naprave. Za teoretično preučevanje delovanja aktivnega elektrokaloričnega regeneratorja smo razvili dinamični 2D numerični model. Model omogoča analiziranje vpliva različnih parametrov na hladilne karakteristike (specifična hladilna moč in hladilno število) naprave z aktivnim elektrokaloričnim regeneratorjem. Izvedli smo teoretično analizo vpliva geometrijskih in obratovalnih lastnosti regeneratorja in analizo vpliva lastnosti večslojnih struktur in lastnosti delovne tekočine na hladilne karakteristike naprave. Preučili smo tudi vpliv histereze elektrokaloričnega materiala in vpliv regeneracije električne energije na energijsko učinkovitost naprave. Za eksperimentalno analizo smo postavili progo za testiranje aktivnih elektrokaloričnih regeneratorjev. Preučili smo delovanje dveh aktivnih elektrokaloričnih regeneratorjev sestavljenih iz ploščic $0{,}1Pb(Mg_{1/3}Nb_{2/3})O_3$-$0{,}9PbTiO_3$ volumske keramike in za nabor obratovalnih parametrov izmerili temperaturni razpon in specifično hladilno moč. Z eksperimentalno analizo smo potrdili koncept delovanja aktivnega elektrokaloričnega regeneratorja. Za primerjavo med teoretičnimi izračuni in eksperimentalnimi rezultati smo v numerični model vključili toplote tokove iz regeneratorja na okolico. Rezultate primerjave smo uporabili za validacijo numeričnega modela.

*

Na Fakulteti za strojništvo Univerze v Mariboru sta obranila svojo doktorsko disertacijo:

● dne *26. maja 2016* **Peter MAJERIČ** z naslovom: »Sinteza nanodelcev zlata z modificirano ultrazvočno razpršilno pirolizo« (mentor: doc. dr. Rebeka Rudolf);

Doktorsko delo predstavlja študije, eksperimentalno delo, tehnike karakterizacije, rezultate in analize, s katerimi je povezana sinteza čistih, okroglih, neaglomeriranih nanodelcev zlata (AuNPs) z velikostjo okoli 50 nm. V prvem delu raziskav smo sintetizirali AuNPs s konvencionalno ultrazvočno razpršilno pirolizo (USP). Za surovino smo uporabili tetrakloroavrično kislino $HAuCl_4$(s), ki smo jo raztopili v vodi. To raztopino smo v komori z ultrazvokom razpršili v kapljice, ki jih je nosilni plin N_2 prenesel v reakcijsko peč. V tej peči so potekale stopnje sinteze: izhlapevanje kapljic, toplotna dekompozicija, redukcija s plinom H_2 in zgoščevanje. Nastali so AuNPs različnih oblik z velikostmi do 300 nm, pri čemer smo identificirali visoko stopnjo aglomeracije. Ker s konvencionalnim USP nismo dosegli cilja, smo postavili hipotezo, da lahko izdelamo ciljne AuNPs z modificiranim USP, kjer je cona izhlapevanja kapljic ločena od reakcijske peči, reducirni plin pa je uveden neposredno v reakcijsko peč. Za potrditev hipoteze smo z eksperimenti preučevali vplivne parametre USP-sinteze: koncentracijo Au v začetni raztopini, temperature v coni izhlapevanja kapljic in v reakcijski peči ter pretok plinov N_2 in H_2. S pomočjo tehnik karakterizacij (TEM, DLS, ICP) na nastalih AuNPs smo ugotovili, da pri USP-sintezi hkrati potekata dva mehanizma nastanka nanodelcev (»kapljica-v-delec«, DTP in »plin-v-delec«, GTP). Z DTP nastajajo veliki nanodelci – do 300 nm, z GTP pa majhni – do 50 nm. Kadar potekata oba mehanizma hkrati, dobimo neugodno bimodalno velikostno porazdelitev AuNPs. Na tej osnovi smo postavili model nastanka AuNPs, ki pojasnjuje, kako lahko pri USP-sintezi s spreminjanjem koncentracije Au v začetni raztopini in pretokov plinov vplivamo na DTP in GTP mehanizma nastanka v korist GTP. S ciljno izbranimi parametri (0,5 g/l Au, 4,5 l/min N_2, 2,0 l/min H_2) smo ustvarili pogoje za nastanek AuNPs z GTP-mehanizmom. Pri tem so nastali okrogli AuNPs z ozko velikostno porazdelitvijo (37,0 ± 5,5 nm). Tako smo potrdili pravilnost postavljenega modela in hipotezo, da lahko z modificiranim USP izdelamo AuNPs ciljnih lastnosti.

- dne *30. maja 2016* **Danilo SLANA** z naslovom: »Vpliv plamenskega ravnanja na nosilnost teleskopskih ročic« (mentor: prof. dr. Nenad Gubeljak);

Teleskopske ročice so zvarjenci, izdelani iz modernih nizkolegiranih visokotrdnostnih finozrnatih jekel. Kot vsi zvarjenci so podvrženi deformacijam zaradi varjenja. Deformacije je treba zmanjšati in med najpomembnejše tehnično in ekonomsko sprejemljive postopke za ravnanje štejemo plamensko ravnanje. Pri plamenskem ravnanju s pomočjo mehanskih vpetij in lokalnega vnašanja toplote s plamenom povzročamo lokalno plastično deformacijo materiala in s tem spreminjamo obliko in velikost obdelovanca. Ker je material S700MC, iz katerega so izdelane teleskopske ročice, občutljiv na vnose toplote, je bil v nalogi raziskan vpliv plamenskega ravnanja na nosilnost tega elementa. Zbrani so bili podatki iz literature in izvedeni preskusi udarne žilavosti in natezne trdnosti. Z metodo končnih elementov so bile ponazorjene deformacije in obnašanje materiala v vroči točki in okolici. Naloga pokaže, da lahko plamensko ravnanje uspešno izvajamo brez vpliva na nosilnost, treba pa je uporabljati nižje temperature, kot smo jih vajeni iz ravnanja konstrukcijskih jekel nižje natezne trdnosti. Naloga tudi pokaže, da je potrebno pripraviti in slediti prilagojenim navodilom za izvedbo plamenskega ravnanja za različne vrste jekla.

Information for Authors

All manuscripts must be in English. Pages should be numbered sequentially. The manuscript should be composed in accordance with the Article Template given above. The maximum length of contributions is 10 pages. Longer contributions will only be accepted if authors provide juastification in a cover letter. For full instructions see the Information for Authors section on the journal's website: http://en.sv-jme.eu .

SUBMISSION:

Submission to SV-JME is made with the implicit understanding that neither the manuscript nor the essence of its content has been published previously either in whole or in part and that it is not being considered for publication elsewhere. All the listed authors should have agreed on the content and the corresponding (submitting) author is responsible for having ensured that this agreement has been reached. The acceptance of an article is based entirely on its scientific merit, as judged by peer review. Scientific articles comprising simulations only will not be accepted for publication; simulations must be accompanied by experimental results carried out to confirm or deny the accuracy of the simulation. Every manuscript submitted to the SV-JME undergoes a peer-review process.

The authors are kindly invited to submit the paper through our web site: http://ojs.sv-jme.eu. The Author is able to track the submission through the editorial process - as well as participate in the copyediting and proofreading of submissions accepted for publication - by logging in, and using the username and password provided.

SUBMISSION CONTENT:

The typical submission material consists of:

- A **manuscript** (A PDF file, with title, all authors with affiliations, abstract, keywords, highlights, inserted figures and tables and references),
- Supplementary files:
  - a **manuscript** in a WORD file format
  - a **cover letter** (please see instructions for composing the cover letter)
  - a ZIP file containing **figures** in high resolution in one of the graphical formats (please see instructions for preparing the figure files)
  - possible **appendicies** (optional), cover materials, video materials, etc.

Incomplete or improperly prepared submissions will be rejected with explanatory comments provided. In this case we will kindly ask the authors to carefully read the Information for Authors and to resubmit their manuscripts taking into consideration our comments.

COVER LETTER INSTRUCTIONS:

Please add a **cover letter** stating the following information about the submitted paper:

1. Paper **title**, list of **authors** and their **affiliations**.
2. **Type of paper**: original scientific paper (1.01), review scientific paper (1.02) or short scientific paper (1.03).
3. A **declaration** that neither the manuscript nor the essence of its content has been published in whole or in part previously and that it is not being considered for publication elsewhere.
4. State the **value of the paper** or its practical, theoretical and scientific implications. What is new in the paper with respect to the state-of-the-art in the published papers? Do not repeat the content of your abstract for this purpose.
5. We kindly ask you to suggest at least two **reviewers** for your paper and give us their names, their full affiliation and contact information, and their scientific research interest. The suggested reviewers should have at least two relevant references (with an impact factor) to the scientific field concerned; they should not be from the same country as the authors and should have no close connection with the authors.

FORMAT OF THE MANUSCRIPT:

The manuscript should be composed in accordance with the Article Template. The manuscript should be written in the following format:

- A **Title** that adequately describes the content of the manuscript.
- A list of **Authors** and their **affiliations**.
- An **Abstract** that should not exceed 250 words. The Abstract should state the principal objectives and the scope of the investigation, as well as the methodology employed. It should summarize the results and state the principal conclusions.
- 4 to 6 significant **key words** should follow the abstract to aid indexing.
- 4 to 6 **highlights;** a short collection of bullet points that convey the core findings and provide readers with a quick textual overview of the article. These four to six bullet points should describe the essence of the research (e.g. results or conclusions) and highlight what is distinctive about it.
- An **Introduction** that should provide a review of recent literature and sufficient background information to allow the results of the article to be understood and evaluated.
- A **Methods** section detailing the theoretical or experimental methods used.
- An **Experimental section** that should provide details of the experimental set-up and the methods used to obtain the results.
- A **Results** section that should clearly and concisely present the data, using figures and tables where appropriate.
- A **Discussion** section that should describe the relationships and generalizations shown by the results and discuss the significance of the results, making comparisons with previously published work. (It may be appropriate to combine the Results and Discussion sections into a single section to improve clarity.)
- A **Conclusions** section that should present one or more conclusions drawn from the results and subsequent discussion and should not duplicate the Abstract.
- **Acknowledgement** (optional) of collaboration or preparation assistance may be included. Please note the source of funding for the research.
- **Nomenclature** (optional). Papers with many symbols should have a nomenclature that defines all symbols with units, inserted above the references. If one is used, it must contain all the symbols used in the manuscript and the definitions should not be repeated in the text. In all cases, identify the symbols used if they are not widely recognized in the profession. Define acronyms in the text, not in the nomenclature.
- **References** must be cited consecutively in the text using square brackets [1] and collected together in a reference list at the end of the manuscript.
- **Appendix(-icies)** if any.

SPECIAL NOTES

Units: The SI system of units for nomenclature, symbols and abbreviations should be followed closely. Symbols for physical quantities in the text should be written in italics (e.g. v, T, n, etc.). Symbols for units that consist of letters should be in plain text (e.g. $\mathrm{ms^{-1}}$, K, min, mm, etc.). Please also see: http://physics.nist.gov/cuu/pdf/sp811.pdf .

Abbreviations should be spelt out in full on first appearance followed by the abbreviation in parentheses, e.g. variable time geometry (VTG). The meaning of symbols and units belonging to symbols should be explained in each case or cited in a **nomenclature** section at the end of the manuscript before the References.

Figures (figures, graphs, illustrations digital images, photographs) must be cited in consecutive numerical order in the text and referred to in both the text and the captions as Fig. 1, Fig. 2, etc. Figures should be prepared without borders and on white grounding and should be sent separately in their original formats. If a figure is composed of several parts, please mark each part with a), b), c), etc. and provide an explanation for each part in Figure caption. The caption should be self-explanatory. Letters and numbers should be readable (Arial or Times New Roman, min 6 pt with equal sizes and fonts in all figures). Graphics (submitted as supplementary files) may be exported in resolution good enough for printing (min. 300 dpi) in any common format, e.g. TIFF, BMP or JPG, PDF and should be named Fig1.jpg, Fig2.tif, etc. However, graphs and line drawings should be prepared as vector images, e.g. CDR, AI. Multi-curve graphs should have individual curves marked with a symbol or otherwise provide distinguishing differences using, for example, different thicknesses or dashing.

Tables should carry separate titles and must be numbered in consecutive numerical order in the text and referred to in both the text and the captions as Table 1, Table 2, etc. In addition to the physical quantities, such as t (in italics), the units [s] (normal text) should be added in square brackets. Tables should not duplicate data found elsewhere in the manuscript. Tables should be prepared using a table editor and not inserted as a graphic.

REFERENCES:

A reference list must be included using the following information as a guide. Only cited text references are to be included. Each reference is to be referred to in the text by a number enclosed in a square bracket (i.e. [3] or [2] to [4] for more references; do not combine more than 3 references, explain each). No reference to the author is necessary.

References must be numbered and ordered according to where they are first mentioned in the paper, not alphabetically. All references must be complete and accurate. Please add DOI code when available. Examples follow.

Journal Papers:

Surname 1, Initials, Surname 2, Initials (year). Title. Journal, volume, number, pages, DOI code.

[1] Hackenschmidt, R., Alber-Laukant, B., Rieg, F. (2010). Simulating nonlinear materials under centrifugal forces by using intelligent cross-linked simulations. *Strojniški vestnik - Journal of Mechanical Engineering,* vol. 57, no. 7-8, p. 531-538, DOI:10.5545/sv-jme.2011.013.

Journal titles should not be abbreviated. Note that journal title is set in italics.

Books:

Surname 1, Initials, Surname 2, Initials (year). Title. Publisher, place of publication.

[2] Groover, M.P. (2007). *Fundamentals of Modern Manufacturing*. John Wiley & Sons, Hoboken.

Note that the title of the book is italicized.

Chapters in Books:

Surname 1, Initials, Surname 2, Initials (year). Chapter title. Editor(s) of book, book title. Publisher, place of publication, pages.

[3] Carbone, G., Ceccarelli, M. (2005). Legged robotic systems. Kordić, V., Lazinica, A., Merdan, M. (Eds.), Cutting Edge Robotics. Pro literatur Verlag, Mammendorf, p. 553-576.

Proceedings Papers:

Surname 1, Initials, Surname 2, Initials (year). Paper title. Proceedings title, pages.

[4] Štefanić, N., Martinčević-Mikić, S., Tošanović, N. (2009). Applied lean system in process industry. *MOTSP Conference Proceedings*, p. 422-427.

Standards:

Standard-Code (year). Title. Organisation. Place.

[5] ISO/DIS 16000-6.2:2002. *Indoor Air – Part 6: Determination of Volatile Organic Compounds in Indoor and Chamber Air by Active Sampling on TENAX TA Sorbent, Thermal Desorption and Gas Chromatography using MSD/FID.* International Organization for Standardization. Geneva.

WWW pages:

Surname, Initials or Company name. Title, from http://address, date of access.

[6] Rockwell Automation. Arena, from *http://www.arenasimulation.com,* accessed on 2009-09-07.

EXTENDED ABSTRACT:

When the paper is accepted for publishing, the authors will be requested to send an **extended abstract** (approx. one A4 page or 3500 to 4000 characters). The instruction for composing the extended abstract are published on-line: http://www.sv-jme.eu/information-for-authors/ .

COPYRIGHT:

Authors submitting a manuscript do so on the understanding that the work has not been published before, is not being considered for publication elsewhere and has been read and approved by all authors. The submission of the manuscript by the authors means that the authors automatically agree to transfer copyright to SV-JME when the manuscript is accepted for publication. All accepted manuscripts must be accompanied by a Copyright Transfer Agreement, which should be sent to the editor. The work should be original work by the authors and not be published elsewhere in any language without the written consent of the publisher. The proof will be sent to the author showing the final layout of the article. Proof correction must be minimal and executed quickly. Thus it is essential that manuscripts are accurate when submitted. Authors can track the status of their accepted articles on http://en.sv-jme.eu/.

PUBLICATION FEE:

Authors will be asked to pay a publication fee for each article prior to the article appearing in the journal. However, this fee only needs to be paid after the article has been accepted for publishing. The fee is 240.00 EUR (for articles with maximum of 6 pages), 300.00 EUR (for articles with maximum of 10 pages), plus 30.00 EUR for each additional page. The additional cost for a color page is 90.00 EUR. These fees do not include tax.

Strojniški vestnik -Journal of Mechanical Engineering
Aškerčeva 6, 1000 Ljubljana, Slovenia,
e-mail: info@sv-jme.eu

9 770039 248001
ISSN 0039-2480

http://www.sv-jme.eu

Contents

Papers